Design and Optimisation Framework of a Multi-MW Airborne Wind Energy Reference System

Master of Science Thesis

Dylan Eijkelhof

Delft University of Technology - Technical University of Denmark

Design and Optimisation Framework of a Multi-MW Airborne Wind Energy Reference System

by

Dylan Eijkelhof

to obtain the degree of Master of Science in Aerospace Engineering at the Delft University of Technology
and Master of Science in Engineering (European Wind Energy) at Technical University of Denmark,
to be defended publicly on 30 September, 2019 at 10:00 AM.

Faculty of Aerospace Engineering, Delft University of Technology

Student number:	4281446 (TU Delft), s173313 (DTU)	
Project duration:	November 1, 2018 – July 31, 2019	
Thesis committee:	Dr.-Ing. R. Schmehl,	TU Delft, supervisor
	Dr. Ir. M. Gaunaa,	DTU, supervisor
	Prof. Dr. Ir. D.A. von Terzi,	TU Delft, reader
	U. Fasel,	ETH Zurich, PhD student

Delft University of Technology
Department of
Aerospace Engineering

Technical University of Denmark
Department of
Wind Energy

The undersigned hereby certify that they have read and recommend to the Faculty of Aerospace Engineering and Department of Wind Energy for acceptance a thesis entitled

"Design and Optimisation Framework of a Multi-MW Airborne Wind Energy Reference System."

by

Dylan Eijkelhof

in partial fulfilment of the requirements for the degree of

Master of Science in Aerospace Engineering at TU Delft
Master of Science in Engineering at DTU

Dated: 30 September 2019

Thesis committee:

Dr.-Ing. R. Schmehl (TU Delft)

Dr. Ir. M. Gaunaa (DTU)

Prof. Dr. Ir. D.A. von Terzi (TU Delft)

U. Fasel PhD (ETHZ)

Preface

This Master thesis has been an amazing learning experience on all sorts of fields like structural modelling, aerodynamic modelling but also doing research in general. It will finish the hard work and long hours I have put into the European Wind Energy Master. I am grateful I could end this period with a project I worked on every day with a lot of pleasure.

The basis for this research originally stemmed from my passion of combining two major research fields, namely Aerospace Engineering and Wind Energy into a project about Airborne Wind Energy. For this, I would like to thank my daily supervisor Urban Fasel (ETH Zurich) and two supervisors Dr. Ir. Roland Schmehl (TU Delft) and Dr. Ir. Mac Gaunaa (DTU) for providing me with the opportunity to do research on this fascinating subject and the support they have given me throughout the project. Urban laid the basis of this thesis way before I even started thinking about what to write my thesis on and without his prior and on-going research I would not have been able to achieve such a big step in the development of an open source Airborne Wind Energy Reference System.

I like to believe this thesis is a first important step for faster development in the AWE sector but hopefully it will not be the last and that many may follow and contribute to a AWE benchmarking network.

The design developed in this thesis is published together with this thesis as a separate MSC.Nastran .bdf file. In case the file is not present and required by the reader an email can be sent to dylan_eijkelhof@hotmail.com requesting the Finite Element Model.

Dylan Eijkelhof
Zurich, September 24, 2019

Abstract

In the present world of conventional wind energy, the National Renewable Energy Laboratory (NREL) 5MW reference wind turbine for offshore system development has become an important piece of the puzzle towards a renewable future based on wind energy. DTU showed the benefit of such a reference model with their 10 MW reference wind turbine and continued the evolution in multi-megawatt wind power systems. Even though these two systems exist in the conventional wind turbine industry, a publicly available reference system does not exist in airborne wind energy.

Currently, Airborne Wind Energy Systems (AWES) are still in the prototype testing phase as no commercial utility-scale product has been released to the market yet. A reference model like the NREL 5MW turbine can therefore significantly increase the speed of AWES development and open a door towards more publicly available research.

This thesis solves the following main research question: "How does a multi-megawatt utility scale airborne wind energy reference system look like, focusing on the main wing parameters?". This is done by setting up a relatively computationally efficient optimisation framework based on a Fluid Structure Interaction (FSI) model combined with a flight dynamics simulation model which can be used in early design optimisations, for example.

The FSI model consists of a 3D linear structural Finite Element model coupled with a potential-flow based 3D panel method. The aircraft structure is parametrised and parameters are found for an aircraft with a wing area of approximately 150 m². The wing mesh and other structural components are created in Matlab while MSC.Nastran is exploited to obtain the stiffness, mass and inertia matrices. A model order reduction technique is applied to the structural model, relying on the mode superposition method to decrease the computation effort by several orders. The wing's aerodynamic behaviour is calculated by the 3D panel method. A model order reduction technique is also applied here, based on a Taylor expansion of the aerodynamic influence coefficient matrices. A modified fixed wing aircraft flight controller is used to fly a circular flight path where the ground station periodically allows the tether to be reeled out and in. The navigation of the aircraft is split up in two components, namely the lateral controller (based on a modification to the L_1-control logic) and radial dynamics controller (depending on the elevator and tether reel-out behaviour).

A Covariance Matrix Adaptation Evolution Strategy (CMAES) optimisation method is applied with a specific objective function to find the system design parameters. This work then presents a detailed representation of the aircraft design, consisting of the planform parameters, material choices and composite layup. It demonstrates the ability of the framework to obtain a wing that can sustain high wing loadings. Also the system performance in a full power cycle illustrates the full potential of a 150 m² wing which is able to generate multiple megawatts of power. This thesis serves as a foundation of reference systems in airborne wind energy, which other researchers can use and adapt to contribute further to a benchmark network in Airborne Wind Energy.

Contents

List of Figures

List of Tables

Nomenclature

Abbreviations

AWE(R)S	Airborne Wind Energy (Reference) System
AWES	Airborne Wind Energy (System)
CMAES	Covariance Matrix Adaptation Evolution Strategy
CMAS	Composite Materials and Adaptive Structures (lab)
DS	Dynamic System
DU	Delft University
FE	Finite Element
FGS	Fixed-Ground-Station
FSI	Fluid Structure Interaction
GG	Ground-Generated
HAWT	Horizontal Axis Wind Turbine
HC	Higher Camber
HPPE	High Performance PolyEthylene
LEI	Leading Edge Inflatable
LE	Leading Edge
MRevE	Reversed Engineered from Makani
NREL	National Renewable Energy Laboratory
ODE	Ordinary Differential Equation
PDE	Partial Differential Equation
PECE	Predict Evaluate Correct Evaluate
TE	Trailing Edge
UD	Uni-directional (composite layup)

Greek symbols

α	Angle of attack	[°]
$\vec{\alpha}_A$	Aircraft Euler angles	[rad]
$\dot{\vec{\alpha}}_A$	Aircraft Euler rates	[rad s^{-1}]
η	Desired roll angle to achieve $a_{s,cmd}$	[rad]
η_g	Generator efficiency	[–]
$\dot{\theta}_A$	Aircraft pitch angle (Euler)	[rad s^{-1}]
θ_A	Aircraft pitch angle (Euler)	[rad]
θ_c	Circumferential angle	[rad]
λ	Eigenvalue	
$\vec{\mu}$	Doublet strength	[m^2 s^{-1}]
ν	Poisson's ratio	[–]
ρ	Air density	[kg m^{-3}]
ρ	Material mass density	[kg m^{-3}]
$\vec{\sigma}$	Source strength	[m^2 s^{-1}]
τ_g	Generator torque	[N m]
τ_{tot}	Total torque acting on drum	[N m]
$\dot{\phi}_A$	Aircraft roll rate (Euler)	[rad s^{-1}]
ϕ_A	Aircraft roll angle (Euler)	[rad]
$\vec{\phi}_{a,i}$	Aileron mode i	
$\vec{\phi}_{v,i}$	Vibration mode i	
φ	Desired roll angle	[rad]
φ	Scalar speed potential function	
$\boldsymbol{\Psi}$	Total expansion basis	
$\boldsymbol{\Psi}_a$	Aileron modes	
$\boldsymbol{\Psi}_v$	Vibration modes	
$\dot{\psi}_A$	Aircraft yaw rate (Euler)	[rad s^{-1}]
ψ_A	Aircraft yaw angle (Euler)	[rad]
$\vec{\omega}_A$	Aircraft angular velocities	[rad s^{-1}]
$\dot{\vec{\omega}}_A$	Aircraft angular accelerations	[rad s^{-2}]

ω_g	Generator angular velocity	[rad s^{-1}]
ω_i	Eigenfrequency of mode i	

Latin symbols

$\boldsymbol{A}$	Aerodynamic influence coefficient matrix (doublet)	
$\boldsymbol{A}_0$	Initial aerodynamic influence coefficient matrix, statically undeformed wing (doublet)	
$\boldsymbol{A}_i$	Aerodynamic influence coefficient matrix, reduction base i (doublet)	
A	Thermal expansion coefficient	[K^{-1}]
A	Wing area	[m^2]
$a_{s,cmd}$	Centripetal acceleration to reach control reference point at L_1	[m s^{-2}]
A_T	Tether area	[m^2]
$\boldsymbol{B}$	Aerodynamic influence coefficient matrix (source)	
$\boldsymbol{B}_0$	Initial aerodynamic influence coefficient matrix, statically undeformed wing (source)	
$\boldsymbol{B}_i$	Aerodynamic influence coefficient matrix, reduction base i (source)	
$\widetilde{\boldsymbol{C}}$	Modal damping matrix (reduced order)	
$\boldsymbol{C}$	Damping matrix	
c_0	Unit damping coefficient	[N s m^{-1}]
C_D	3D drag coefficient	[–]
C_d	2D drag coefficient	[–]
$C_{D,c}$	Cylinder drag coefficient	[–]
$C_{D,i}$	Induced drag coefficient	[–]
$C_{D,v}$	Viscous drag coefficient	[–]
C_L	3D lift coefficient	[–]
C_l	2D lift coefficient	[–]
$\boldsymbol{C}_p$	Pressure coefficient	[–]
$d_{x,sweep}$	Rib translation over the X_B-axis	[m]
E	Young's modulus	[Pa]
$\vec{F}$	Aerodynamic force	[N]
$\vec{F}_A$	Total forces acting on the aircraft	[N]
$\vec{f}_a$	Aerodynamic forces in modal coordinates	
$\vec{F}_{A,a}$	Aerodynamic force	[N]
$\vec{F}_{A,g}$	Gravity force	[N]
$\vec{F}_{A,t}$	Tether force	[N]
$\vec{F}_{a,i}$	Aerodynamic force	[N]
$\vec{F}_{d,i}$	Aerodynamic drag force on tether particle i	[N]
$\vec{F}_{dp,i}$	Damping force on tether particle i	[N]
$\vec{F}_{DS}$	Generalised force vector	
$F_{G(1,2)}$	Gravity force component	[N]
$\vec{F}_{G,i}$	Gravity force on tether particle i	[N]
$\vec{F}_{s,i}$	Spring force on tether particle i	[N]
F_t	Tether force magnitude	[N]
$\vec{F}_{T,i}$	Total force on tether particle i	[N]
G	Shear modulus	[Pa]
h	Altitude from ground	[m]
h_{ref}	Wind measurement reference altitude	[m]
I	Integral controller gain	[–]
I_{GS}	Combined generator, gearbox and drum inertia	[kg m^2]
$\boldsymbol{J}$	Aircraft intertia matrix	
$\widetilde{\boldsymbol{K}}$	Modal stiffness matrix (reduced order)	
$\boldsymbol{K}$	Stiffness matrix	
k_0	Unit stiffness coefficient	[N m^{-1}]
K_p	Proportional controller gain	[–]
$\dot{L}$	Rate of change in angular momentum	[N m]
l_0	Flight path tether length parameter	[m]
L_1	Reference point distance	[m]
l_{init}	Initial tether length	[m]

$\widetilde{\boldsymbol{M}}$	Modal mass matrix (reduced order)	
$\boldsymbol{M}$	Mass matrix	
M	Mach number	[–]
$\vec{M}_A$	Moments acting on the aircraft	[N m]
M_a	Total number of aerodynamic nodes	[–]
m_A	Total aircraft mass	[kg]
$\vec{M}_{A,a}$	Aerodynamic moments	[N m]
$\boldsymbol{M}_{DS}$	Generalised mass matrix	
M_s	Total number of structural nodes	[–]
$m_{T,i}$	Tether particle mass	[kg]
$\boldsymbol{n}$	Panel normal	
N	Number of composite layers	
N	Number of considered structural modes	
n_g	Gearbox ratio	[–]
$n_{s,s}$	Number of wing skin nodes	
n_T	Number of tether particles	
P	Proportional controller gain	[–]
p	Pressure	[Pa]
$\dot{p}_A$	Aircraft angular acceleration in x direction	[rad s^{-2}]
p_A	Aircraft angular velocity in x direction	[rad s^{-1}]
P_{el}	Electric power	[W]
$\boldsymbol{Q}$	Total panel velocities	
$\vec{q}$	Total modal amplitudes	
q	Dynamic pressure	[Pa]
$\dot{q}_A$	Aircraft angular acceleration in y direction	[rad s^{-2}]
$\vec{q}_a$	Aileron modal amplitudes	
q_A	Aircraft angular velocity in y direction	[rad s^{-1}]
$\vec{q}_v$	Vibration modal amplitudes	
$\boldsymbol{r}$	Panel coordinates	[m]
$\dot{r}_A$	Aircraft angular acceleration in z direction	[rad s^{-2}]
r_A	Aircraft angular velocity in z direction	[rad s^{-1}]
r_c	Flight path radius	[m]
r_d	Drum radius	[m]
Re	Reynolds number	[–]
Rot_z	Rib rotation around the Z_B-axis	[rad]
S	Allowable stress for in-plane shear.	[Pa]
S_c	Allowable stress in compression	[Pa]
S_s	Allowable stress in shear	[Pa]
S_t	Allowable stress in tension	[Pa]
t	Time	[s]
T_{ref}	Material reference temperature	[K]
$\widetilde{\boldsymbol{T}}_T$	Modal thin plate spline interpolation matrix	
$\vec{u}$	Displacement	[m]
$\dot{u}_A$	Aircraft acceleration in x direction	[m s^{-1}]
$\dot{\vec{u}}$	Velocity	[m s^{-1}]
u_A	Aircraft velocity in x direction	[m s^{-1}]
$\ddot{\vec{u}}$	acceleration	[m s^{-2}]
$\boldsymbol{V}$	Velocity	
$\dot{v}_A$	Aircraft acceleration in y direction	[m s^{-1}]
$\vec{v}_A$	Aircraft flight velocity	[m s^{-1}]
v_A	Aircraft velocity in y direction	[m s^{-1}]
$\dot{\vec{v}}_A$	Aircraft flight acceleration	[m s^{-1}]
$\boldsymbol{V}_{el}$	Structural displacement induced velocities	[m s^{-1}]
$\boldsymbol{V}_p$	Perturbation velocities on panel	[m s^{-1}]
V_{reel}	Tether reel out speed	[m s^{-1}]
$\dot{\vec{v}}_{T,i}$	Tether particle acceleration	[m s^{-2}]
$\vec{v}_{T,i}$	Tether particle velocity	[m s^{-1}]
$\vec{V}_w$	Wind velocity	[m s^{-1}]
$\dot{w}_A$	Aircraft acceleration in z direction	[m s^{-1}]

w_A	Aircraft velocity in z direction	[m s^{-1}]
$\vec{X}$	Flight state vector	
$\vec{x}_a$	Aerodynamic node location	[m]
X_c	Allowable stress in compression in the longitudinal direction	[Pa]
$\vec{x}_s$	Structural node location	[m]
X_t	Allowable stress in tension in the longitudinal direction	[Pa]
$\vec{y}$	Dynamic state vector	
Y_c	Allowable stress in compression in the lateral direction	[Pa]
Y_t	Allowable stress in tension in the lateral direction	[Pa]
z	Spanwise distance from root	[m]
z_0	Roughness length (terrain type)	[m]
Z_p	Z-axis of tilted plane at centre of flightpath	

1 Introduction

A substantial amount of energy is demanded by a growing world population and the technologically improving societies, which comes with growth and possibility to do technical research. This is complementary to the human satisfaction, for nourishment and the ability to perform their jobs [1]. Jobs are becoming progressively dependent on computers and other technological devices, which both require power.

In the present world of conventional wind energy, the National Renewable Energy Laboratory (NREL) 5 MW reference wind turbine for offshore system development [2] has become an important piece of the puzzle towards a renewable future based on wind energy. Several companies and universities utilise the data and results provided for this turbine as a reference to compare their own design and analysis. Later, DTU designed a 10 MW reference wind turbine [3] for research purposes and continued the evolution in multi-megawatt power systems. This turbine is an up-scaled version of the NREL 5 MW turbine design except for the rotor blades, which are re-designed for optimal 10 MW power generation.

One issue with renewable energy harvested by wind turbines, is that a growth of wind farms can cause saturation of windy areas which are satisfactory for installations. This is the reason why current research is done in optimising the power capacity per unit area. This is discernible in the global development of large-scale wind turbines [4].

The main focus of this report is on a relatively new research area, namely Airborne Wind Energy Systems (AWES). The current stage of this research is still in the prototype testing phase. No commercial utility-scale product has been released to the market yet. Universities and companies are presently both involved. This area is promising as larger and more persistent wind speeds are found at these high altitudes (e.g. 200m - 10km). Loyd presented the basic principle in 1980 with a theoretical maximum energy that can be extracted from the wind by an AWES [5]. Different AWES are tested at the moment. There are trade-offs made between fixed ground stations and moving ground stations; ground-generated and flight-generated power; and between rigid wing aircraft and soft kites.

Up to the knowledge of this thesis' author, a publicly available reference system like the 5MW or 10MW reference turbines does not exist in airborne wind energy, definitely not in the megawatt-scale. This research aims to achieve such a representative multi-megawatt utility-scale system where the initial system planform is known and initiate a benchmark network for AWE researchers.

Designing large-scale AWES, requires a closer look into the many physical challenges of upscaling, as aeroelasticity, for example, starts playing a major role. Increasing flexibility of the wing induces large deformations, significantly changing the aerodynamic behaviour of the wing. Dealing with these challenges, requires a more complex approach.

To create the system, a parametric model is set-up for the aircraft. Some of the required information is reverse-engineered from published documents of airborne wind energy system design companies, such as Ampyx Power or Makani Power, or is designed with the help of other publicly available aircraft/system design sources. Considering the envisioned design is based on the Ampyx Power AP4 aircraft (in other words an upscaled version of the AP3), wing surface and aspect ratio parameters are collected from Ampyx Power. This data is then combined with their AP3 published progress reports [6]. The Ampyx Power AP4 system will initially be designed in order to re-power decommissioning offshore wind farm installations [7].

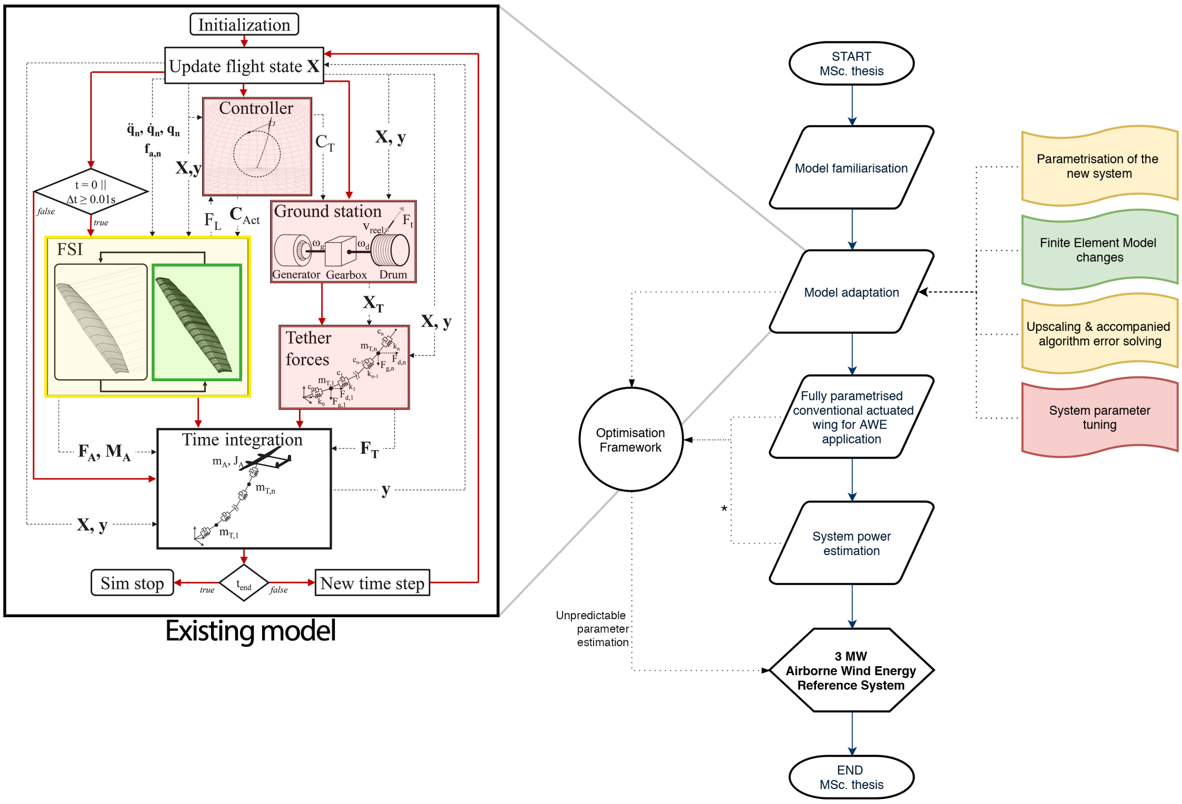

Figure 1.1: Thesis flowchart, including the existing aero-servo-elastic model [8] and the applied modifications/additions by the author in colour.

2
State of the art

The state of the art is split-up into three parts, namely the background of airborne wind energy system research; aero-servo-elastic and dynamic system modelling including the models provided by the Laboratory of Composite Materials and Adaptive Structures(CMAS) at ETH Zurich; and reference models within wind energy combined with scalability of AWE systems. A more detailed presentation of state of the art research in Airborne Wind Energy in general can be found in [9].

2.1. Background

Different system configurations exist in Airborne Wind Energy. These system are either based on an on-board generator or a generator on the ground. On-board generator systems all rely on rotors. Whether this is in the form of turbines in front of a wing, rotors in autorotation or a turbine inside a lifting aerostat depends on the choice of the company. Within ground generators there are mainly two types of ground stations. Fixed ground stations, where stationary generators generate electricity by a pumping motion or moving ground stations where the generator can move around. With motion enabled generators, power can be produced by the motion of wheels or by a rotating platform, for example [10]. Fixed-ground-station ground-generated Airborne Wind Energy Systems (FGS-GG-AWES) are amidst the most elaborately studied airborne wind energy systems by academic research facilities and individual companies. This is also visible in the diagram in figure 2.1 with data presented in [10].

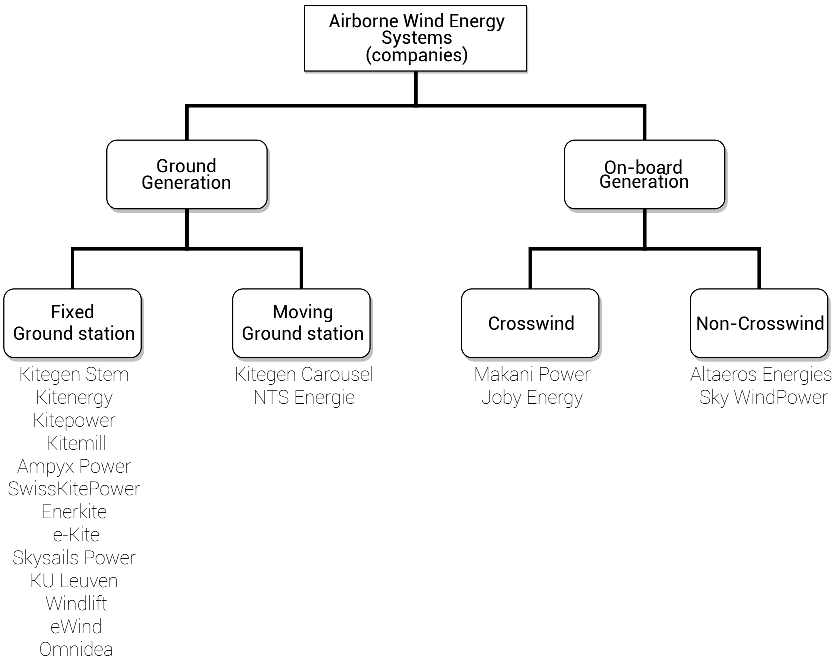

Figure 2.1: Companies working on different types of AWESs.

In this research a reference model will be created based mostly on the FGS-GG-AWES, the Ampyx Power AP4 aircraft project. This aircraft designed by Ampyx Power has a generator based on the ground rather than on-board, mainly because it comes with higher risk to put such a valuable part of the system up in the sky (in case of a crash). Also, the tether can be less complex as no electrical current has to flow through [11]. However, the tether will have a lower life span due to the continuous switch between production and recovery cycles (e.g. traction and retraction). For on-board generator systems the production efficiency can be higher as there is no recovery phase necessary [12].

Energy transformation is done by a two-phase process, the production and the recovery phase. In the production phase, electrical energy is generated by a tensile interaction between the aircraft and the ground station. In the recovery phase a smaller amount of energy is consumed. The system consists of ropes wounded around winches, which in turn are connected to a generator axis [10]. During the production phase, the aircraft is configured to produce a maximum traction force on the rope and consequently maximise the energy production. The recovery phase consist of the opposite, motors rewind the rope around the winch and the aircraft is controlled in a way to minimise the power consumed in the process [13, 14]. Another method that can be used by a ground station in the recovery phase is high-speed winching. Without changing the angle of attack the aircraft/kite is reeled-in directly against the wind [15].

The flight mode which is used the most in airborne wind energy is the crosswind flight. As initially demonstrated by Loyd and later also proven by many others, the crosswind flight mode achieves one or two orders of magnitude higher power than non-crosswind flight mode [5]. This does depend on the way power is produced. For example with a turbine in the middle of a lifting aerostat, developed by Altaeros Energies, crosswind might not be optimal. Another way to obtain a significant increase in power would be having better aerodynamic efficiency of the tether [16].

Different aircraft can be used in Fixed-ground-station ground-generated Airborne Wind Energy Systems (FGS-GG-AWES). Leading Edge Inflatable(LEI) kites, foil kites, delta kites, gliders, swept rigid wings and semi-rigid wings. More and more companies are changing to rigid wing aircraft (e.g. gliders) [10, 17] as the fabric wings have durability issues, influencing the lifetime and performance [18]. Hence, this is one of the reasons why a glider will be used in this reference model. Additionally, the control system of a rigid wing aircraft is less complex as the system dynamics are much better understood and the system has less degrees of freedom due to less wing flexing. In case of a disjointed tether, the aircraft can still be reliably controlled [11]. Kites typically survive only for a couple of hundred hours while with composite structures the lifetime of a rigid wing can go up to 20 years [11, 18]. Reducing the number of replacements of the aircraft can significantly reduce the maintenance costs and downtime.

A few different companies are researching the different possibilities within this branch of Airborne Wind Energy Systems. KiteGen Research has been one of the early companies to be testing out a prototype of a FGS-GG-AWES [9]. After some years of testing their prototype, they changed their research focus to a new generator type, namely KiteGen Stem. This system consists of special winches that are driven by a pulley system on a flexible rod (Stem) which then in turn connects to the aircraft by a rope. This Stem is chosen mainly for two reasons: to support and hold the aircraft, and to reduce spikes in the tether loading caused by wind gusts. The entire ground station can rotate in azimuthal angles which allows the Stem to have two degrees of freedom respective to the ground. Even though the concept was first patented by KiteGen in 2008 [19], several other companies and academic research facilities develop a similar concept nowadays. In order to boost the endurance of their systems, KiteGen also develops aerodynamic ropes [20]. EnerKite invented a 30kW rated power pumping kite portable generator. It is portable as it can be mounted on the back of a truck. Their aircraft can only be controlled from the ground by three ropes attached to both wings and the fuselage. EnerKite currently changed their focus to semi-rigid wings [21]. Ampyx Power was the first company that successfully developed a pumping glider generator [22]. The aircraft is connected to the ground-station by one single tether. [6]

2.2. Modelling

Aero-servo-elastic modelling of an aircraft developed over time. A few developments are summarised and presented below. Early studies done in [23, 24] use the Langrange equations and model the structure as a number of point masses which only endure small deformations. A mean-axis reference frame is utilised. Aerodynamic forces are given in the form of stability derivatives. In the following period a program called ASTROS is designed. ASTROS is an Automated STRuctural Optimisation System [25], which couples a finite element structure with both steady and unsteady aerodynamics. Drela developed the software called ASWING, a tool capable of analysing the aerodynamic, structual and control behaviour of an aircraft [26, 27]. It couples a lifting line aerodynamic model with structure composed of non-linear beams. Aerodynamic lag is also accounted for in the form of corrections. The research done by Waszak and Schmidt and Buttrill et al. lead to the development of a framework where an aero-servo-elastic model is developed and coupled with flight dynamics [28–35]. Instead of a mean-axis reference frame, a body reference frame is used. Lagrange equations are used as well, but for the aerodynamics, a strip model is used. The strip model has low fidelity but is capable of estimating aerodynamic forces at low computational cost. Later, a model including a geometrical exact representation of the structure and a non-linear based aerodynamic model is developed [36].

This shows that modelling of Airborne Wind Energy System dynamics has been done by several research sources. Studies in this century have been done mostly on point masses and rigid body dynamics of soft kites [37–39]. A tool called UM/NAST developed at the University of Michigan, solves the system for highly flexible aircraft. This is done by means of coupling a non-linear beam structural model an unsteady aerodynamic model and a non-linear control dynamics model. Reduced order models are applied to the non-linear beam representation [40–43]. Several more contemporary studies are done applying theories on multibody- and particle system dynamics [38, 44], and FE modelling of flexible kites [45]. Fasel et al. and Wijnja et al. show an approach to model the aeroelastic characteristics of rigid wing AWES in crosswind conditions [46, 47]. Fasel et al. couple a linear 3D FE model with a nonlinear extended lifting line method into a two-way FSI simulation. Wijnja et al. extends the earlier mentioned simulation code ASWING to simulate the aeroelastic characteristics of an Airborne Wind Turbine. A tensile support system is introduced, modelled by multiple forces acting on the tether-wing attachment points.

Even though these approaches were chosen over time, different structural and aerodynamic models should be chosen for different purposes and available computational resources. Different structural and aerodynamic models are shown in figure 2.2. It is sorted by computational cost from low computational effort necessary (left) to high computational cost (right). Most methods are collected by Dussart et al. [48] where the rationale for the qualitative positions is explained.

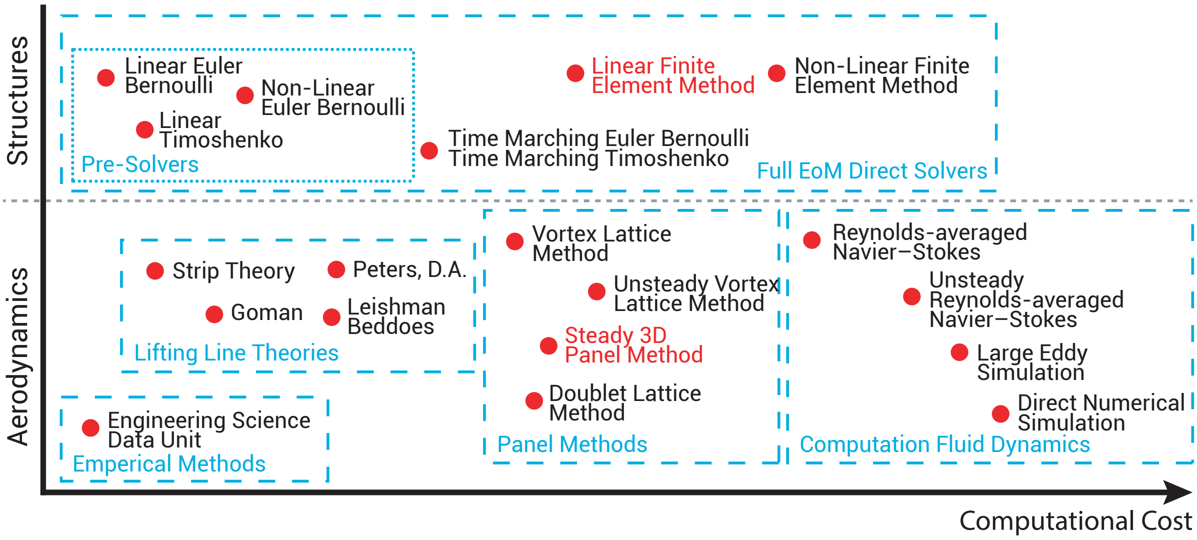

Figure 2.2: Structures and aerodynamics modelling methods sorted by computational cost with the models used in this thesis in red.

For the aero-servo-elastic model used in this thesis, a higher fidelity model described in [8, 49] is chosen. A fluid structure interaction simulation is set up by coupling of a linear three dimensional finite element structural model with a three dimensional panel aerodynamic model, in contradiction to the method described in [46] where an extended lifting line aerodynamic model is utilised. This panel method is especially applicable in optimisation frameworks and conceptional design phase where subsonic attached flows are considered, friction drag is ignored and the calculation time is one of the dominant factors [50]. This FSI model is then in turn coupled with a flight dynamics model including both the aircraft, ground station and tether. Model order reduction techniques are applied to the finite element and the three dimensional panel method, in order to increase the computational efficiency of the simulation and enabling the user to efficiently run a multidisciplinary optimisation [49].

The model designed in [8, 49] is designed to fly a circular trajectory. Several numerical optimisations are performed by Horn et al. [51]. Flying several loops before retracting the tether increases the average power production. Flying figure of eight shaped flight paths could also potentially be more advantageous, but currently it is unknown what is the optimal trajectory shape.

2.3. Wind energy benchmarking and scalability

In the present world of wind energy, the NREL 5MW reference wind turbine has become an important piece of the puzzle towards a renewable future based on wind energy. Just like the 5MW turbine, also the DTU 10MW turbine has been a key contribution. These turbines can be used for initial system performance estimation when scaling the rotor, for example.

For the 5MW reference turbine designed by NREL a set of different parameters and results was published to be useful for the research society. First of all, the legal liability and responsibility are mentioned. It is necessary to provide the main reason why the model is required and to whom it is useful.

Realistic and standardized input data is required to make conceptual studies useful. A description of the whole system with its aerodynamic, structural and control-system properties are provided. Different sources of data were required to be utilised and it is shown how the data is composed to the final system properties [2].

The DTU 10MW reference turbine designed at the Technical University of Denmark(DTU) uses the NREL 5MW turbine as a basis with a new blade design for improving aerodynamic properties and shows the upscaling process. Validation is done as an important step in order to make the results valuable. Also uncertainty estimates are made for the used models [52].

Scaling up of an Airborne Wind Energy System requires different modelling approaches but may provide several benefits. For example, regarding the tether drag, by reaching critical Reynolds numbers on the tether itself. Most dimensional parameters are found to be linearly scalable in first approximations [53]. Linearly increasing the dimensions quadratically increases the wing area while the mass scales cubically, which is also known as the square-cube law [54]. Increasing the surface area increases the wing drag and lowers the relative importance of the drag produced by the tether [53].

An important concept in scaling of AWESs, is the flying mass. Increasing the mass of the aircraft reduces the tension on the tether, which in turn reduces the power generated by the aircraft. This is due to the fact that power production highly depends on tension on the tether (upscaling can therefore only be done by taking the mass closely into consideration) [55].

2.4. Research objective and approach

This literature study leads to the following main research question:

> *How does a multi-megawatt utility scale airborne wind energy reference system look like, focusing on the main wing internal structure parameters?*

The main objective is as follows:

> *"Provide detailed specifications of the first scalable utility-scale multi-megawatt ground generated airborne wind energy reference system and initiate a benchmark network to encourage the further development of airborne wind energy applications."*

In order to find the answer to the research question, this thesis is set-up in four major parts. In the previous sections of this chapter, the relevant state-of-the-art research in airborne wind energy systems is summarised. In chapter 3 the methods, the aero-servo-elastic tool, used to analyse the Airborne Wind Energy System is described combined with the objectives of the initial optimisations within this framework. An existing model developed at ETH Zurich [8] is adapted to work with conventional actuated wings at large scale. An adapted finite element model is then implemented back into the existing framework where the main parameters of the wing can be determined including the composite layup. The aerodynamic behaviour of the wing is then solved by a modified three dimensional panel method [50]. Control parameters are found, which are necessary to produce power at different wind speeds. The final results of this analysis are presented in section 4.2 with all system parameters. Section 4.3 shows an extensive illustration of the reference system's performance and design outcomes of different optimisations. The thesis set-up is structured into a flowchart seen in figure 1.1, which shows the work done in this thesis and the applied modifications to the existing system simulation can be observed.

3
Methods

In this chapter, the developed aero-servo-elastic model is elaborated on, based on the work of Fasel et al. [8]. The way of numerically solving the AWE aircraft's dynamics, combined with the wing's tether dynamics and aero-elastics, banks on an alternating solution of a conventionally actuated wing FSI model and a model made up of the aircraft-, ground station- and tether dynamics. The two models are written in Matlab (Simulink) and figure 3.1 shows the schematic of the total system. The FSI model contains a three dimensional structural FE model and a three dimensional panel method. The FSI is first introduced by Molinari et al. [56], where the full model description can be read. Fasel et al. [8] also describes the complete model, therefore, only a summary of the used parts out of the original model is given in this thesis. This is complemented with an elaborate description of the added/changed parts. After the model description, the optimisation strategy is explained, including the objective functions which are used to steer the optimiser in finding the wanted results.

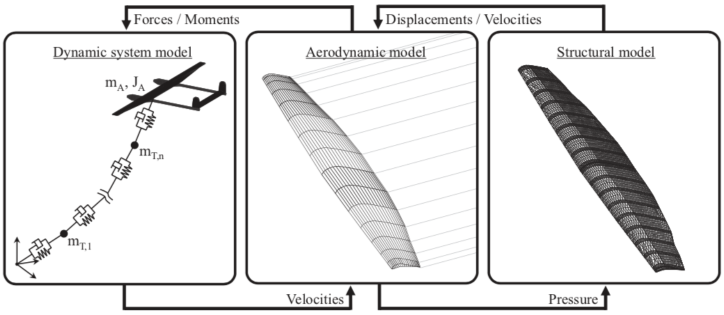

Figure 3.1: Coupling method of the aircraft, ground station and tether dynamics with the FSI model [8].

First, the parametrization of the system is described in section 3.1. Second, the structural model, built from the first eight parameters, is described in section 3.2. Third, the aerodynamic model is presented in section 3.3. In this section the panel method is introduced together with the flutter analysis. Fourth, the used control and flight dynamics model is displayed in section 3.4. Fifth, the coupling strategies, between the prior methods, are described in section 3.5. Last, the convergence study strategy and objective functions of the optimiser are elaborated on in section 3.6.

3.1. System parametrisation

Running the algorithm starts with initialising the planform parameters of the system. In order to decide which values are used, the AWES is parametrised. This parametrisation is done to the following parts:

1. Wing planform (e.g. span, chord and sweep etc.).
2. 2-dimensional airfoils at root and tip.
3. Airfoil twist at root and tip.
4. Number of spanwise sections (e.g. ribs).
5. Number of chordwise sections (e.g. spars and stringers).
6. Fuselages and tail.
7. Composite layup of the wing skin at the root and tip.
8. Aileron mechanism.
9. Tether.
10. Ground station.
11. Flight conditions.
12. Wind model.
13. Flight controller.

As this thesis is primarily focusing on the internal structure of the main wing, the most detailed parametrisation is required for this lift generating device. Other parts are more simplified, examples are the fuselage and tail modelled like simple beam structures requiring less defining parameters.

In chapter 2 it is mentioned that the envisioned overall design is based on the AP4 system of Ampyx Power (taking the published parameters of the AP3 system into account when upscaling the wing). The wing area is therefore taken to be approximately 150 m^2. This is the surface area contemplated by Ampyx Power for the AP4 aircraft (M. Kruijff, personal interview, January 31, 2019). In order to obtain this surface area, the span and chord lengths of the AP3 are upscaled keeping a similar aspect ratio.

The reasoning for choosing specific parameters for the parametrisation is given in sections 3.2 to 3.4. Section 4.2 elaborates on the reference system parameter values. Here a detailed description is given on how the algorithm represents the system. When all parameters are initialised, the input file (.bdf) for MSC.Nastran is created. Section 3.2 describes the Finite Element mesh which is written to this file. The parameters specified at the root and tip are linearly interpolated to the rib locations in between. This is done in order to keep the number of parameters being optimised small, consequently keeping the computational effort limited. Acknowledging that this system is meant to serve as a reference/benchmark model and finding the right scale to produce power in the MW scale, a more extensive system parametrisation is out of the scope of this thesis.

3.2. Structural model

The structural model consists of a 3D finite element model. The wing mesh and other structural components are created in Matlab while MSC.Nastran[57] is exploited to obtain the stiffness, mass and inertia matrices. The Finite Element Method is a computational model to solve complex partial differential equations (PDE's). It relies on discretising a surface in a number of finite elements. Depending on the shape choice of the element, there are 3, 4 or more nodes per element. The method solves the PDE's at these nodes to determine the displacements. The accuracy of this method strongly depends on two factors, namely the element size (e.g. number of elements) and the type of element (e.g. shape). Each element type relies on different assumptions. The type of elements chosen and their characteristics are elaborated on in subsection 3.2.1.

Before running MSC.Nastran, the root's wingbox section is fixed by single point constraints to enforce zero displacement. After the mesh is created, the linear static analysis(SOL101) solver of MSC.Nastran is used to obtain the mass- and stiffness-matrices as well as the aircraft inertia's. The aeroelastic behaviour is then evaluated in Matlab, calculating the steady state of forces acting on the aircraft. MSC.Nastran, a commercial program, is used because it is desired to have a fast calculation time and this software is optimised to generate the stiffness- and mass- matrices as quickly as possible. This speeds up the process and saves time on programming it during this thesis. Combining the two software, a good combination of design flexibility and high speed analysis is achieved.

In this chapter, first, the set-up of the finite element model is shown in subsection 3.2.1. Second, the obtained system of equations is shown in subsection 3.2.2.

3.2.1. Finite Element model

The three dimensional finite element model is modelled with plate (CTRIA3), beam (CBEAM) and rod (CROD) elements to formulate the structural mesh. This is done in multiple steps:

1. Generate the aircraft planform.
2. Generate skin property ID's.
3. Interpolate airfoil shapes to rib positions.
4. Create rib nodes.
   (a) Choose maximum node spacing.
   (b) Interpolate nodes to the right airfoil shape.
5. Create skin and spars plate elements (CTRIA3).
6. Find the nodes on the stringerpath and create beams representing the stringers.
7. Create servo-actuation rods and aileron hinge mechanisms.
8. Add the fuselage and tail beams.
9. Add rib plate elements (CTRIA3).

First, the wing, fuselage and tail parameters are combined to create the planform of the aircraft (see figure 4.4). The ribs are spaced over the semi-span of the wing. The sweep angle, taper and twist distribution are applied along the semi-span determining the leading edge and trailing edge positions of each spanwise station. Between the fuselages, the chord and twist are kept constant. As can be seen in figure 3.2 and with measurements in figure 4.4, the taper is applied from the trailing edge and the ribs are kept orthogonal to the trailing edge.

Second, the property identification numbers are generated for the skin elements in order to provide the right properties to the skin elements and to define different composite layups later in the algorithm.

Third, two airfoils are being interpolated from the root to the tip in order to determine the wing cross-sections along the span. When similar airfoils are chosen at the root and tip, the airfoil shape is only scaled by the chord length and rotated by its preferred structural twist angle.

Fourth, at each rib station the rib nodes are generated. This is done by choosing the maximum node spacing (determined by a convergence study shown in subsection 4.1.1) and interpolating the nodes of the airfoil shape determined in the previous step to their chosen chordwise positions.

Fifth, the skin panels and spar sections are added to the model. A spanwise maximum element size is used to create the elements of the skin and spars. First a quadrilateral mesh is obtained by dividing the spanwise sections into multiple elements by interpolation between the ribs. Including these nodes, Delaunay triangulation is applied to each cell (provided by the intersections of ribs and stringers) to create the indices in between the ribs which produce triangles forming a CTRIA3 element in MSC.Nastran. These triangular elements rely on the assumption that in this particular element a constant strain is present. This results in a constant stress tensor for that specific element. One can conclude then that the key importance in obtaining accurate results is to make sure the stress gradient within the element is comparatively small. The final mesh of the top skin can be seen on figure 3.2.

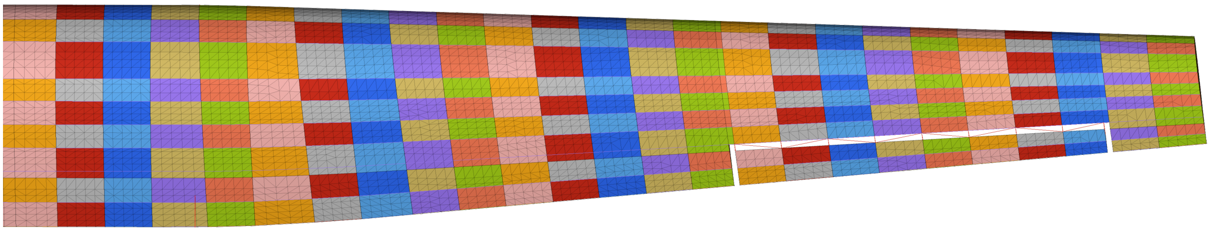

Figure 3.2: Upper surface mesh of the main wing (top view), the colours represent different material property identification numbers.

Sixth, stringers are represented by CBEAM elements. These elements have a solid rectangular cross-section represented by a width and certain composite layup. It is ensured the stringers are kept straight towards the tip.

Seventh, the aileron mechanism is added to the system (see figure 3.3). Many researchers have used the RBE2, RBE3, CBUSH, CBEAM(+pinflags) elements or a combination of them to simulate the hinge axis and add dependencies to the nodes which make the aileron rotate [58–60]. However, in the current FSI model a much simpler method was chosen. For the FSI model, the equations of motion are solved in the Matlabenvironment and not only in MSC.Nastran. When using RBE2 or RBE3 elements, modifications to these equations of motion are necessary. Using a web of very stiff, but not infinitely stiff, CROD elements, the aileron can be constraint to only rotate around the specified axis without modifying the equations already set-up by [8]. At each spanwise bottom end of the aileron an actuator is implemented. In the structural model this is done by adding two CROD elements per aileron with a high enough stiffness to withstand the aerodynamic forces but also low enough to be deformed by an applied external actuator force. Without these actuator elements, the aileron can rotate infinitely around its rotational axis which results in a singular stiffness matrix

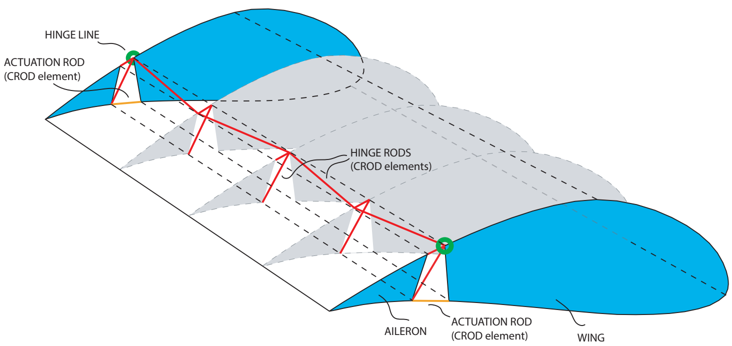

Figure 3.3: Aileron hinge FEM representation (arbitrary number of ribs for illustrative purposes only).

Eighth, the structure is expanded with the fuselages and tail. Even though this thesis focuses on the main wing, the fuselages and tail are added to the model in order to represent the added stiffness and inertia in the system. Simple CBEAM elements are used just like for the stingers. For the Fuselages a tube cross-section is chosen, as this is the closest depiction of the hollow structure. For the tail a hollow bar cross-section is used. This resembles the wing box of the tail airfoil.

Last, the rib elements are created. For each rib station, CTRIA3 elements are generated within the airfoil shape. Because of the non-straight geometry and already available function in Matlab performing the Delaunay triangulation, the ribs are modelled with CTRIA3 elements. Each rib is divided in three sections, the wing, the gap and the rear (aileron) panel. The process of creating one of these panels can be seen in figure 3.4. The reasoning for choosing three panels is rather simple, to include the gap between the wing and the aileron, the gap panel can just be left out. In step 1, a rectangular grid of nodes is introduced within the back panel boundaries. Step 2 eliminates the nodes outside the airfoil boundaries and moves the inner nodes to a more equidistant position to the profile shape and makes sure there is sufficient distance between nodes. Step 3 then generates the triangular elements and returns the three node indices required to form each element.

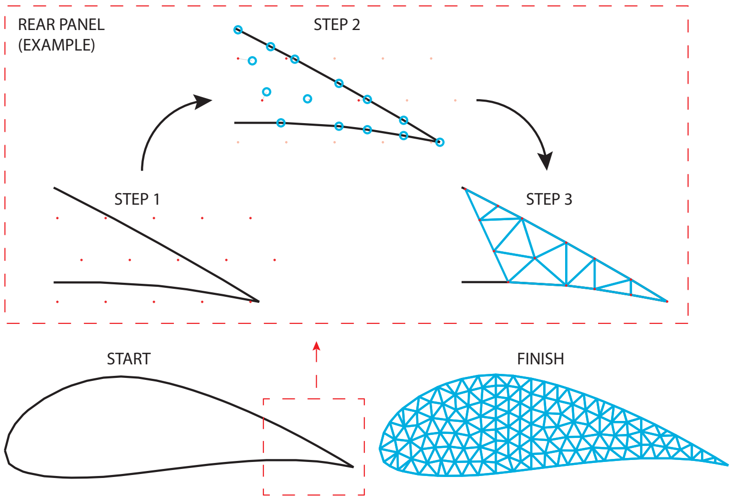

Figure 3.4: Rib triangular mesh generation,

3.2.2. System of equations

In order to make the FSI-interface faster, and thus the dynamic simulation, a model order reduction technique is applied to the structure.

The linear equations of motion of the dynamic structural system is given in eq. (3.1).

$$\boldsymbol{M}\ddot{\vec{u}} + \boldsymbol{C}\dot{\vec{u}} + \boldsymbol{K}\vec{u} = \vec{F}, \tag{3.1}$$

where $\boldsymbol{M}$,$\boldsymbol{C}$,$\boldsymbol{K}$ $\in \mathbb{R}^{M_s \times M_s}$ are the mass, the damping and the stiffness matrices, $\vec{u}$,$\dot{\vec{u}}$,$\ddot{\vec{u}}$ $\in \mathbb{R}^{M_s}$ the displacements, the velocities, and the accelerations, respectively and $\vec{F} \in \mathbb{R}^{M_s}$ the external loads. The displacements are given by eq. (3.2) with the model order reduction technique applied based on the mode superposition method [61].

$$\vec{u} \approx \begin{bmatrix} \boldsymbol{\Psi}_v & \boldsymbol{\Psi}_a \end{bmatrix} \begin{bmatrix} \vec{q}_v \\ \vec{q}_a \end{bmatrix} = \boldsymbol{\Psi}\vec{q}, \tag{3.2}$$

where $\boldsymbol{\Psi}_v$ contains the vibration modes $\left[\vec{\phi}_{v,1}, \dots, \vec{\phi}_{v,i}, \dots, \vec{\phi}_{v,N,v}\right]$ and $\boldsymbol{\Psi}_a$ contains the aileron modes $\left[\vec{\phi}_{a,1}, \vec{\phi}_{a,2}\right]$, $\vec{q}_v$ and $\vec{q}_a$ are the modal amplitudes, and $\boldsymbol{\Psi}$ and $\vec{q}$ are the total expansion basis and the total modal amplitude vector, respectively. The first vibration mode and both the aileron modes are visualised in figure 3.5.

The vibration modes are determined by solving the free vibration generalised eigenvalue problem given in eq. (3.3).

$$\left(\boldsymbol{K} - \omega_i^2 \boldsymbol{M}\right) \vec{\phi}_{v,i} = \vec{0}, \tag{3.3}$$

where ω_i is the corresponding eigenfrequency. The aileron modes are determined with the static equation of motion, given the actuation forces $\vec{F}_{a,i}$, by eq. (3.4).

$$\vec{\phi}_{a,i} = \boldsymbol{K}^{-1}\vec{F}_{a,i} \tag{3.4}$$

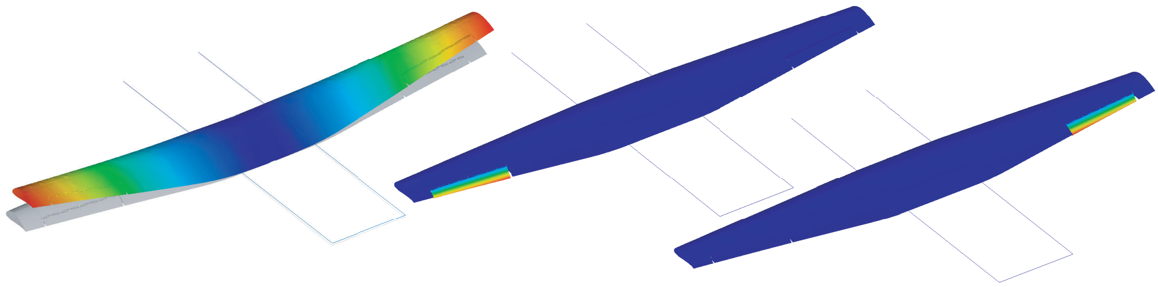

Figure 3.5: First vibration mode (left), the first aileron mode (centre) and the second aileron mode (right).

Inserting eq. (3.2) into eq. (3.1) and applying the Galerkin projection, several modal matrices are obtained. Namely, $\widetilde{\boldsymbol{M}} = \boldsymbol{\Psi}^T\boldsymbol{M}\boldsymbol{\Psi}$, $\widetilde{\boldsymbol{C}} = \boldsymbol{\Psi}^T\boldsymbol{C}\boldsymbol{\Psi}$ and $\widetilde{\boldsymbol{K}} = \boldsymbol{\Psi}^T\boldsymbol{K}\boldsymbol{\Psi}$, which are calculated only once. Resulting in the new equation of motion given by eq. (3.5). The reduced EOM is then numerically integrated using the method developed by Newmark et al. [62].

$$\widetilde{\boldsymbol{M}}\ddot{\vec{u}} + \widetilde{\boldsymbol{C}}\dot{\vec{u}} + \widetilde{\boldsymbol{K}}\vec{u} = \boldsymbol{\Psi}^T\vec{F}, \tag{3.5}$$

Currently, it is chosen to use 10 vibration modes and 2 actuator modes. This is chosen, based on an earlier research performed on the FTERO aircraft at ETH Zurich. However, their aircraft is much smaller. Due to time constraint it is decided for this initial reference system to keep the number of modes the same as they used. In further development is necessary to do a parameter study on the number of modes necessary to accurately capture the wing deformations and increase the fidelity of the FSI solver.

3.3. Aerodynamic model

The aerodynamic model consists of a potential-flow based three dimensional panel method following the proposed algorithm by Katz and Plotkin [63] and implemented in Matlab by Filkovic [50]. Subsection 3.3.1 gives a brief description of the method applied and what conditions are being satisfied. The flutter analysis method is explained in subsection 3.3.2.

3.3.1. 3D panel method

Modelling the aerodynamics of an aircraft can be done in different ways. The one that is most accurate is to perform experimental testing. However, a prototype is necessary which can be very expensive at large scales and unacceptable during the early design stage of an AWE system. Numerical modelling of the aerodynamic behaviour by use of the panel method, is already used for years. Other methods as the finite volume method are more accurate than the panel method but are significantly slower in solving the problem.

The model is based on the recognised and well-known incompressible flow Navier-Stokes equations [64]. Equation (3.6) shows the conservation of mass and eq. (3.7) the conservation of momentum. Combining these equations with the law of newton viscosity, this results in eqs. (3.8) and (3.9), the Navier-Stokes equations for incompressible fluids. In the 3D panel method the viscosity contribution is omitted.

$$\frac{\partial \rho}{\partial t} + \frac{\partial(\rho u_i)}{\partial x_i} = 0 \tag{3.6}$$

$$\frac{\partial(\rho u_i)}{\partial t} + \frac{\partial(\rho u_i u_j)}{\partial x_j} = -\frac{\partial p}{\partial x_i} + \frac{\partial \tau_{ij}}{\partial x_j} + \rho f_i \tag{3.7}$$

$$\vec{\nabla}\vec{u} = 0 \tag{3.8}$$

$$\rho(\frac{\partial \vec{u}}{\partial t} + \vec{\nabla}\rho\vec{u} \otimes \vec{u}) = -\vec{\nabla}p + \mu\vec{\nabla}^2\vec{u} + \rho\vec{f} \tag{3.9}$$

In the case of potential flow, eq. (3.6) can be rewritten to the Laplace equation eq. (3.10) with the scalar speed potential φ.

$$\vec{\nabla}^2\varphi = 0 \tag{3.10}$$

For the 3D panel method a key property of the Laplace equation is used. The sum of any two solutions forms a solution on its own. In other words, the present flow can be arranged in such a way that it presents the sum of singularities whose values are obtained by satisfying specific boundary conditions. The particular implementation used in this thesis is based on quadrilateral panel source-dipole discretization that solves the Laplace equation. The potential within the body's surface is zero as the Dirichlet boundary condition (no penetration of the boundary layer more specifically) is imposed. The Kutta condition is applied at the trailing edge, making the trailing edge wake source strength equal to the difference between the trailing edge upper- and lower panel. A more specific explanation on this panel method can be found in [8, 50].

The chosen panel method is beneficial in this framework as it has the ability to determine the volumetric body surface pressures at a relatively low computational cost. As the complete algorithm is designed to optimise a system and requiring a large amount of computation cycles, a rather fast aerodynamic computation is necessary. High fidelity results require solving the wing displacement at each time step, and thus keeping the simulation time low is necessary.

A drawback, however, is that it is based on inviscid flow. This means that stall behaviour of the wing is not modelled. In order to counteract this effect, and prevent the overestimating of the lift and consequently power performance, a boundary is set on the lift. Limiting the maximum lift coefficient will limit the maximum angle of attack attainable during the simulation. The method used by [8] and described in [65] is also used for the wing developed during this research. The Critical Section Method(CSM) is demonstrated to have the best resemblance with wind tunnel experiments for unswept wings. The current wing design only has a very small sweep angle and CSM is therefore chosen to be the best option just like for the morphing wing in [8]. At an arbitrary spanwise locations the local two dimensional angle of attack at maximum lift coefficient is determined. The minimum section angle of attack determines the angle of attack where the 3D maximum lift coefficient is acquired. The two dimensional lift coefficients are determined via RFOIL [66]. The 3D stall angle of attack is pre-computed and kept constant throughout the simulations. In order to prevent the need for any post-stall behaviour estimations the analysis is stopped when the maximum lift coefficient is surpassed.

Currently, a steady flat wake is shed behind the wing instead of a helical wake. As a quasi steady flow is assumed during the proposed flight trajectory, more explained in detail in section 3.4, this assumption stays within reasonable error limits.

First the potential flow needs to be solved. This is done by solving the linear system of equations in eq. (3.11).

$$\boldsymbol{A}\vec{\mu} + \boldsymbol{B}\vec{\sigma} = \vec{0}, \tag{3.11}$$

where $\boldsymbol{A}$, $\boldsymbol{B} \in \mathbb{R}^{M_a \times M_a}$ are the doublet and source aerodynamic influence coefficient matrices, respectively and different for each wing configuration. $\vec{\mu}$, $\vec{\sigma} \in \mathbb{R}^{M_a}$ are the doublet and source strength vectors, respectively. The coefficient matrices $\boldsymbol{A}$ and $\boldsymbol{B}$ are dependent on the geometry and thus have to be recalculated at each time step to account for bending and/or twist of the wing and aileron deflection. In [63], the detailed derivation of the doublet and source aerodynamic influence coefficient matrices can be found. As mentioned earlier the Dirichlet boundary condition is enforced on each panel, together with the panel normal $\boldsymbol{n} \in \mathbb{R}^{M_a \times 3}$ and the flow velocity seen by each panel, the source strength can be determined directly by eq. (3.12).

$$\vec{\sigma} = -\boldsymbol{n} \cdot \boldsymbol{V}, \tag{3.12}$$

$$\boldsymbol{V} = \vec{v}_A + \vec{V}_w + \vec{\omega}_A \times \boldsymbol{r} + \boldsymbol{V}_{el}, \tag{3.13}$$

where $\vec{v}_A \in \mathbb{R}^3$ represents the aircraft's velocity, $\vec{V}_w \in \mathbb{R}^3$ the wind velocities, $\vec{\omega}_A \in \mathbb{R}^3$ the aircraft's angular velocity, $\boldsymbol{r} \in \mathbb{R}^{M_A \times 3}$ the coordinates of all panels and $\boldsymbol{V}_{el} \in \mathbb{R}^{M_A \times 3}$ the structural displacement induced velocities. Section 3.5 describes how $\boldsymbol{V}_{el}$ is obtained from structural to aerodynamic mesh interpolation.

Combining eqs. (3.11) and (3.12) the system can be solved for the doublet strength according to eq. (3.14). The total panel velocities can then be calculated by eq. (3.15) and the perturbation velocities on panel i by eq. (3.16).

$$\vec{\mu} = \boldsymbol{A}^{-1}\boldsymbol{B}\left(\boldsymbol{n} \cdot \boldsymbol{V}\right) \tag{3.14}$$

$$\boldsymbol{Q} = \boldsymbol{V} + \boldsymbol{V}_p \tag{3.15}$$

$$V_{p,i,t1} = -\frac{\partial \mu_i}{\partial t_1}, \quad V_{p,i,t2} = -\frac{\partial \mu_i}{\partial t_2}, \quad V_{p,i,n} = \sigma_i \tag{3.16}$$

The three aforementioned perturbation velocities are in the two tangential directions (t_1 and t_2) and the normal direction. For the tangential derivates a central differencing scheme is applied.

With the total panel velocities, $\boldsymbol{Q}$, known, the pressure coefficients can be calculated with eq. (3.17).

$$\boldsymbol{C_p} = 1 - \frac{\boldsymbol{Q}^2}{\boldsymbol{V}^2}. \tag{3.17}$$

Integrating the pressure over the upper- and lower surface of the wing, the lift can be computed. Taking the local lift coefficient of each panel, the induced drag coefficient is estimated by an extended lifting line approach described in [63]. As mentioned before, the main drawback of the 3D panel method is that it is based on inviscous flow. This means the viscous drag needs to be implemented separately. This is done in pre-processing step, where the viscous drag is computed for the undeformed wing. A non-linear extended lifting line approach is combined with RFOIL. RFOIL is used to determine the two dimensional airfoil characteristics. As there are only small variations in de viscous drag caused by deformations of the wing and there are very high lift conditions ($C_{D,i} >> C_{D,v}$) during a power cycle, the viscous drag does not have to be recalculated for deforming geometry [63, 66, 67].

Just like for the structural model the system of equations can be rewritten when applying model order reduction methods. With this application, again the computational efficiency is increased. Earlier it was mentioned the influence coefficient matrices $\boldsymbol{A}$ and $\boldsymbol{B}$ are dependent on the geometry and thus have to be recalculated at each time step. Nonetheless, applying a Taylor expansion of the matrices on the structural vibration mode allows for the matrices not having to be recalculated at each time step as shown in eq. (3.18).

$$\boldsymbol{A} \approx \boldsymbol{A}_0 + \sum \boldsymbol{A}_i q_i, \quad \boldsymbol{B} \approx \boldsymbol{B}_0 + \sum \boldsymbol{B}_i q_i, \tag{3.18}$$

where $\boldsymbol{A}_0$, $\boldsymbol{B}_0$ are the initial influence coefficient matrices calculated for the original statically deformed wing and $\boldsymbol{A}_i$, $\boldsymbol{B}_i$ are the influence matrices of the different reduction base shapes. $\boldsymbol{A}_i$, $\boldsymbol{B}_i$ are obtained using a forward differencing scheme. As shown in eq. (3.14), matrix $\boldsymbol{A}$ needs to be inverted. This means eq. (3.18) still needs to be factorised at each time step, counteracting the benefit of the model order reduction technique. Miller supplies a theorem which gives the exact expression for the inverse of a sum of two arbitrary square matrices which are non-singular [68]. This allows the inverse of $\boldsymbol{A}$ to be calculated by eq. (3.19).

$$\boldsymbol{A}^{-1} = \boldsymbol{A}_0^{-1} - \frac{1}{1 - tr\left(\sum \boldsymbol{A}_i q_i \boldsymbol{A}_0^{-1}\right)} \boldsymbol{A}_0^{-1} \sum \boldsymbol{A}_i q_i \boldsymbol{A}_0^{-1}. \tag{3.19}$$

3.3.2. Flutter analysis

Flutter analysis is performed using a simple modal eigenvalue analysis. The stability system in modal coordinates is written in eq. (3.20).

$$\left[\lambda^2 \widetilde{\boldsymbol{M}} + \widetilde{\boldsymbol{K}} - \frac{q_i}{q_0} \widetilde{\Delta \vec{F}}\right] \vec{q} = \vec{0}, \tag{3.20}$$

where $\lambda \in \mathbb{R}^N$ are the system's eigenvalues, $q_i \in \mathbb{R}^1$ the dynamic pressure at a given flight speed, q_0 the dynamic pressure at reference velocity, $\vec{q}$ the modal displacements, $\widetilde{\Delta \vec{F}} = \boldsymbol{\Psi}^T(\vec{F} - \vec{F}_0) \in \mathbb{R}^N$ and $\vec{F}_0 \in \mathbb{R}^N$ the forces at reference velocity. The force vectors are calculated by running the reduce order FSI. This does assume steady aerodynamics which can have a negative effect on the calculation accuracy [69].

Flutter occurs when the real part of the complex λ crosses through zero. The velocity at which this occurs is evaluated for each mode and the lowest velocity from the modes is taken as the critical flutter speed. A safety factor of 1.5 is then applied to the flutter speed and this is then compared to the flight velocity in each simulation to make sure no flutter occurs throughout an entire power cycle.

Wijnja et al. uses a similar approach to compare the flutter speeds of different flutter modes. Also the sensitivity of the center of gravity position on the flutter speed is shown. This thesis only considers flutter speed as an extra requirement to better represent reality. Therefore, the influences considered in [47] are not evaluated. However, in more detailed analysis of the system, sensitivity is something that should be taken into account.

3.4. Control and flight dynamics model

In this section, the models used for each of the different disciplines within the flight dynamics model are presented. First, the aircraft model in subsection 3.4.1. Second, the tether in subsection 3.4.2. Third the ground station with gearbox and generator in subsection 3.4.3. Fourth, the wind model for calculating the wind speed at each height in subsection 3.4.4. Last, the flight controller and desired trajectory in subsection 3.4.5

3.4.1. Aircraft

In order to model the aircraft in the simulation outside of the FSI interface, the aircraft is represented by a fixed mass. The equations of motion for such an aircraft in the body fixed reference frame are given by eqs. (3.21) to (3.23).

$$\dot{\vec{v}}_A = \begin{bmatrix} \dot{u}_A \\ \dot{v}_A \\ \dot{w}_A \end{bmatrix} = \frac{\vec{F}_A}{m_A} - \vec{\omega}_A \times \vec{v}_A = \frac{\vec{F}_{A,a} + \vec{F}_{A,g} + \vec{F}_{A,t}}{m_A} - \vec{\omega}_A \times \vec{v}_A, \tag{3.21}$$

$$\dot{\vec{\omega}}_A = \begin{bmatrix} \dot{p}_A \\ \dot{q}_A \\ \dot{r}_A \end{bmatrix} = \boldsymbol{J}_A^{-1}(\vec{M}_A - \vec{\omega}_A \times (\boldsymbol{J}_A \vec{\omega})) = \boldsymbol{J}_A^{-1}(\vec{M}_{A,a} - \vec{\omega}_A \times (\boldsymbol{J}_A \vec{\omega}_A)), \tag{3.22}$$

$$\dot{\vec{\alpha}}_A = \begin{bmatrix} \dot{\phi}_A \\ \dot{\theta}_A \\ \dot{\psi}_A \end{bmatrix} = \begin{bmatrix} 1 & \sin\phi_A \tan\theta_A & \cos\phi_A \tan\theta_A \\ 0 & \cos\phi_A & -\sin\phi_A \\ 0 & \frac{\sin\phi_A}{\cos\theta_A} & \frac{\cos\phi_A}{\cos\theta_A} \end{bmatrix} \begin{bmatrix} p_A \\ q_A \\ r_A \end{bmatrix}, \tag{3.23}$$

where the aircraft's velocity and acceleration terms are given by $\vec{v}_A = (u_A, v_A, w_A)^T$ and $\dot{\vec{v}}_A \in \mathbb{R}^3$, respectively. m_A is the aircraft mass and $\vec{F}_A \in \mathbb{R}^3$ the forces acting on the aircraft, consisting of the aerodynamic, gravity, and tether loads. The moments acting on the aircraft are denoted by $\vec{M}_A \in \mathbb{R}^3$, consisting of the aerodynamic moments $\vec{M}_{A,a} \in \mathbb{R}^3$. The moment induced by the tether is not taken into account as in the current configuration the tether is attached in the centre of gravity. $\boldsymbol{J}_A \in \mathbb{R}^{3\times3}$ contains the aircraft's moment of inertias calculated by Nastran and corrected by including an engine weight. $\vec{\omega}_A = (p_A, q_A, r_A)^T$, $\dot{\vec{\omega}}_A \in \mathbb{R}^3$ are the angular velocities and accelerations, respectively. Equation (3.23) calculates the angular velocities in the body-fixed reference frame by multiplying a transformation matrix with the angular velocities in the inertial reference frame, with $\vec{\alpha}_A = (\phi_A\ (roll), \theta_A\ (pitch), \psi_A\ (yaw))^T$, $\dot{\vec{\alpha}}_A \in \mathbb{R}^3$ are the Euler angles and corresponding rates. Figure 3.6 shows the location and directions of the inertial reference frame (X_I, Y_I, Z_I) and the body-fixed reference frame (X_B, Y_B, Z_B).

3.4.2. Tether

Several models exist in order to model the dynamics of the tether. When creating a multi-megawatt system, not only the aircraft size but also the length and thickness of the tether increases. This raises the importance of modelling the tether dynamics in an appropriate way due to phenomena like the sag and an increasing tether drag. As the tether modelling itself is not in the scope of this thesis, only a brief summary is supplied. Three options are described here, a rigid body approximation; linear spring-damper element; and a multiple particle system.

The first option is by far the easiest way to model the tether but accuracy is low and therefore it can only be applied to simple simulations and not in the desired higher fidelity model used in this thesis.

The second option models the tether by a linear spring-damper element which is performing quite well for a tether shorter than 100m [70]. A big scale AWE system, as designed in this thesis, requires a tether length much longer than 100m.

The third option describes a method using a number of point masses. Spring-damper elements are used to connect these point masses to one another. From the three, this method describes the dynamics most accurately [70, 71]. However, the main disadvantage of this approach is that a small time-step is required to model the behaviour owing to the high stiffness of the springs.

The existing framework presented in [8] already has a tether model, based on method three and presented in [71], ready with satisfying behaviour and therefore this one is chosen for the analysis of this reference system. The unit stiffness and damping properties are acquired by using Hook's law and combining this with the specific material properties. Equations (3.24) and (3.25) are used to calculate the unit stiffness- and the unit damping coefficient.

$$k_0 = \frac{EA_T}{l_{T,0}} \tag{3.24}$$

$$c_0 = 0.005k_0 \tag{3.25}$$

$$\tag{3.26}$$

The model provides a quite reasonable performance as long as the space between particles is relatively small [71]. Throughout the simulation, the number of masses is kept constant and thus the weight of each point mass must change during the traction and retraction phase. The equations of motion of the tether particles are represented by eq. (3.27).

$$\dot{\vec{v}}_{T,i} = \frac{1}{m_{T,i}(t)}(\vec{F}_{T,i} - \dot{m}_{T,i}(t)\vec{v}_{T,i}) \approx \frac{\vec{F}_{T,i}}{m_{T,i}(t)} = \frac{\vec{F}_{d,i} + \vec{F}_{G,i} + \vec{F}_{s,i} + \vec{F}_{dp,i}}{m_{T,i}(t)}, \tag{3.27}$$

where $\vec{F}_{T,i} \in \mathbb{R}^3$ are the loads acting on each tether element, consisting of the gravity, aerodynamic drag, spring and damping forces.$\vec{v}_{T,i}$, $\dot{\vec{v}}_{T,i} \in \mathbb{R}^3$ are the particle's velocity and acceleration, respectively.

For the simulations the number of tether particles in this thesis is taken as $\mathrm{n}_T = 5$ particles. For a higher accuracy the number of tether particles should be determined by a convergence study on the power production, but time constraint did not allow for the verification of this parameter during the current research period.

3.4.3. Ground station

The ground station model consists of three components, namely the generator, drum and gearbox. The implementation relies on the conservation of angular momentum principle. To simplify the model, it is assumed that the gearbox and shafts stiffness are infinite. This assumption allows for the combination of the generator-, gearbox- and drum inertias into one value of total inertia, I_{GS}. The change in angular momentum can then be calculated by eq. (3.28). This change in angular momentum is equal to the drum's total endured torque, τ_{tot}.

$$\dot{L} = I_{GS}\dot{\omega}_g = \frac{I_{GS}}{r_d}\dot{v}_{reel} = \tau_{tot}, \tag{3.28}$$

where $\dot{L}$ is the change in angular momentum, I_{GS} the total inertia, $\dot{\omega}_g$ the angular acceleration at the drum, r_d the drum radius and $\dot{v}_{reel}$ the reel-out acceleration.

The total torque can be calculated using eq. (3.29).

$$\vec{\tau}_{tot} = r_d F_t + n_g \tau_g + \tau_{fric}. \tag{3.29}$$

where F_t is the magnitude of the force the tether exerts on the drum, n_g gearbox ratio, τ_g the generator torque and τ_{fric} the friction.

Combining and rearranging eqs. (3.28) and (3.29) the generator torque can be determined by eq. (3.30).

$$\tau_g = n_g^{-1}\left(\frac{I_{GS}}{r_d}\dot{v}_{reel} - r_d F_t - \tau_{fric}\right) \tag{3.30}$$

Knowing the generator torque, the electrical power output of the generator can be calculated using eq. (3.31).

$$P_{el} = \eta_g \tau_g \omega_g, \tag{3.31}$$

where η_g is the generator efficiency and ω_g the angular velocity at the drum location.

3.4.4. Wind

Wind changes velocity with altitude which is one of the reasons why airborne wind energy systems are promising. In order to calculate the different wind speeds, a relation between reference wind speed and altitude is used. Equation (3.32) shows a logarithmic profile of the wind. The relation is commonly used in calculating the wind speeds in wind energy [72].

$$v_w(h) = v_{w,ref} \frac{\log\left(h/z_0\right)}{\log\left(h_{ref}/z_0\right)}, \tag{3.32}$$

where $v_{w,ref}$ is the measured wind speed at reference height h_{ref}. Typically, the wind speed is measured at an altitude of 6 m. z_0 is dependent on the terrain type and taken to be 0.03 which represents farmland with only a very small amount of buildings and trees.

3.4.5. Controller and flight path

In order to make the aircraft produce power and show the potential of the reference system, a rather simple approach is chosen to control the aircraft and fly a prescribed trajectory. The already availability of this model and the main focus of this thesis on the system specification are the dominating factors of this choice. This means a lot of improvement can still be made on flying a different trajectory for instance but for an initial performance estimation this controller satisfies.

The flight controller controls the aircraft and ground station during the simulation. This allows the aircraft to fly the trajectory and the tether to be reeled in and out. The strategy is first introduced in airborne wind energy by Galliard et al. [73] where a state-of-the-art fixed wing aircraft flight controller is modified. A circular flight path is flown where ground station periodically lets the tether being reeled out and in. The navigation is split up in two components, namely the lateral and radial dynamics. Fagiano et al. and Rapp et al. present a similar approach to control a rigid wing AWE system [74, 75]. Lateral dynamics are controlled by changing the aileron angle and its accompanied roll, whereas the pitch angle and the tether state control the radial dynamics. No active yaw controller is implemented as the aircraft is assumed stable in this rotation.

3.4.5.1. Flight path

As mentioned earlier, a circular flight path is flown. This flight path is prescribed by three parameters. An initial tether length, path radius and the elevation angle relative to the ground. From these parameters the flight path is prescribed as seen in figure 3.6

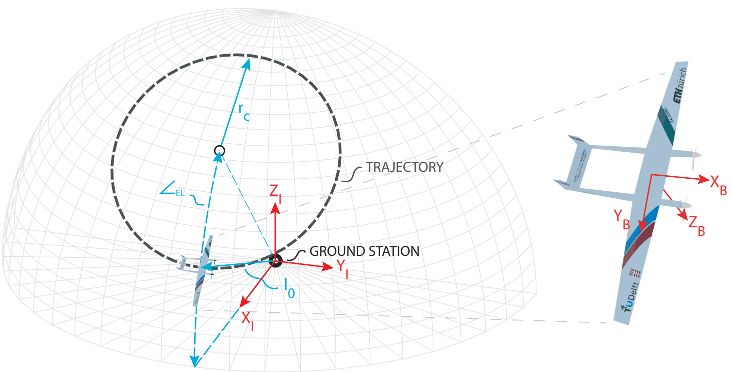

Figure 3.6: Definition of the prescribed trajectory.

3.4.5.2. Lateral (roll) controller

The lateral or roll controller works similar to the method described in [76], based on a modification to the L_1-control logic. The aircraft follows the circular trajectory described in sub-subsection 3.4.5.1 on a plane which is tilted around the inertial y-axis, Y_I.

The L_1-control logic controls the aircraft by calculating a required centripetal acceleration to reach a reference point on the trajectory defined by a distance L_1. The obtained circular path to fly to the reference point is tangential to the velocity vector of the aircraft and can be described by a radius r and angle η. The acceleration is defined in eq. (3.33).

$$a_{s,cmd} = \frac{V^2}{r} = 2\frac{V^2}{L_1}\sin\eta, \tag{3.33}$$

where η is the desired roll angle to achieve the determined $a_{s,cmd}$. It is derived using the circle radius r_c, the distance L_1, aircraft position and velocity V. The lateral acceleration of the aircraft is calculated by eq. (3.34).

$$a_{s,cmd} = 2\frac{V^2}{L_1}\sin\eta = \frac{1}{m_A}\left(F_{G,1}\tan\delta - F_{G,2} + F_L\left(\tan\delta\cos\varphi - sin\varphi\right)\right), \tag{3.34}$$

where δ is the angle between the tether and the Z_p-axis (tilted flight path Z-axis, pointed towards the ground station) and the forces $F_{G,1}$ and $F_{G,2}$ are components of the gravity vector. The gravity force components are dependent on the actual roll angle of the aircraft. Rearranging equation eq. (3.34) allows for the calculation of the desired roll angle, φ.

3.4.5.3. Radial (pitch, ground station) controller

The radial controller is a combination of the pitch controller and the ground station controller. The pitch controller adapts the elevator angle to achieve a desired angle of attack. The ground station or winch controller allows for a periodical motion of the tether reel out. When the aircraft velocity aligns with the gravity vector, the aircraft accelerates the most. Therefore, in downwards flight the aircraft's velocity increases. Consequently higher lift forces can be achieved, and thus higher power. The ground station reels out in this stage and slows down until the retraction phase starts when flying towards higher altitudes. In upward flight the gravity force slows down the aircraft and smaller lift forces can be obtained. The controller tries to adapt the angle of attack to increase the lift during reel-out and decrease the lift during reel-in, in order to attain more power optimal flight configurations and limiting the power consumption during retraction. The angle of attack is limited to the maximum pre-computed angle of attack, discussed in subsection 3.3.1. Another limit is the buckling force of the wing. The force of the tether on the aircraft cannot exceed the buckling force (a safety factor of 1.5 is included). As this is not implemented in the dynamic simulation, the optimiser gets punished when exceeding this load limiting the angle of attack and reel-out system characteristics. The periodical behaviour of the desired angle of attack and reel out are described by Fourier-series for the desired trajectory, given the aircraft's circumferential angle, θ_c, as input. The desired angle of attack is then processed by the attitude controller. The desired tether length, however, is converted into a reel out speed by the ground station controller.

3.4.5.4. Actuator inputs for attitude control

The desired roll angle and angle of attack is transformed into aileron and elevator actuator input, using the combination of two PI-controllers and two P-controllers. This controller is based on a standard controller for attitude tracking of fixed-wing aircraft [77]. Two loops are used to change the actuator states. Two PI-controllers (one for roll and one for pitch) are used to convert the roll and pitch angles into roll and pitch rates. This is done in the outer loop of the controller. Two proportional controllers with variable gains determined by eq. (3.35) are used in the inner loop to convert the roll and pitch rates into aileron and elevator inputs.

$$K_P = \frac{K_{P,pre}}{V_T^2}, \tag{3.35}$$

where K_P is the used gain of the P-controller, $K_{P,pre}$ the predefined constant controller gain and V_T^2 the magnitude of the aircraft's velocity squared.

The desired tether length is converted into a desired generator torque in two steps. The first step is done by applying a proportional controller which outputs the reel out speed. A PI-controller is then used in the second step to obtain the desired generator torque.

3.5. Coupling strategies

This section describes the strategy used to couple the structural- with the aerodynamic model, creating a fluid-structure interaction simulation in subsection 3.5.1. Subsection 3.5.2 describes the coupling of the FSI model with the flight dynamics simulation, and elaborates on the ordinary differential equation solver used by Matlab Simulink to solve the system of equations and proceed from one time step to another.

3.5.1. Fluid - structure interface

The structural mesh designed in section 3.2 and the aerodynamic mesh section 3.3 do not align at their common interface. Therefore, an interpolation between meshes must be performed at this interface. The coupling of the structural model with the aerodynamic model is done by two different interpolation methods. One of which is the thin plate spline method, which outperforms other methods in both efficiency and accuracy [78–80]. The thin plate spline method is used in order to transfer the structural displacements from one mesh to another. The forces on the aerodynamic mesh are transferred back to the structural mesh by another method called inverse distance weighting [81]. This other method is chosen because the thin plate spline method would result in large oscillations of the forces on the structure and therefore, assumed an inappropriate method [82].

The thin plate splines method assumes that a sum of spline functions can approximate the displacements of an arbitrary point on the structural and aerodynamic mesh at location $\vec{x} \in \mathbb{R}^3$.

$$u_m(\vec{x}) = \sum_{i=1}^{n_{s,s}} \gamma_i \|\vec{x} - \vec{x}_{s,i}\|^2 \log_{10}\left(\|\vec{x} - \vec{x}_{s_i}\|^2\right) + p(\vec{x}), \; m = \{a, s\}, \tag{3.36}$$

where $n_{s,s}$ are the number of skin nodes given by the structural mesh, $\vec{x}_{s,i} \in \mathbb{R}^3$ is the location of one structural node i, and γ_i and $p(\vec{x})$ are an interpolation coefficient and a linear polynomial with coefficients $\beta \in \mathbb{R}^4$, respectively. Using this assumption, the known displacements of structural nodes and the unknown displacements of the aerodynamic nodes can be presented like in eq. (3.37) where eq. (3.36) is rewritten into matrix form.

$$\vec{u}_a = [\boldsymbol{M}_{a,s} \; \boldsymbol{P}] \begin{bmatrix} \vec{\gamma} \\ \vec{\beta} \end{bmatrix}, \tag{3.37}$$

$$\begin{bmatrix} \vec{u}_s \\ \vec{0} \end{bmatrix} = \begin{bmatrix} \boldsymbol{M}_{s,s} & \boldsymbol{P}_s \\ \boldsymbol{P}_s^T & 0 \end{bmatrix} \begin{bmatrix} \vec{\gamma} \\ \vec{\beta} \end{bmatrix}, \tag{3.38}$$

where $M_{a,s} \in \mathbb{R}^{M_a \times n_{s,s}}$ is $\|\vec{x} - \vec{x}_{s,i}\|^2 \log_{10}\left(\|\vec{x} - \vec{x}_{s_i}\|^2\right)$ evaluated for $\vec{x}$ being the nodes on the aerodynamic mesh and $M_{s,s} \in \mathbb{R}^{n_{s,s} \times n_{s,s}}$ is the same equation evaluated on the structural nodes.

Combining and rearranging eq. (3.37) an interpolation matrix $\boldsymbol{T}_T \in \mathbb{R}^{M_a \times n_{s,s}}$ can be found in the form of eq. (3.39) and the displacements on the aerodynamic mesh can be determined by eq. (3.40).

$$\boldsymbol{T}_T = \begin{bmatrix} \boldsymbol{M}_{a,s} & \boldsymbol{P}_a \end{bmatrix} \begin{bmatrix} \boldsymbol{M}_{s,s} & \boldsymbol{P}_s \\ \boldsymbol{P}_s^T & 0 \end{bmatrix}^{-1}, \tag{3.39}$$

$$\vec{u}_a = \boldsymbol{T}_T \vec{u}_s. \tag{3.40}$$

As the wing is a three dimensional object it undergoes deformations in three dimensions as well. A block diagonal matrix $\boldsymbol{T}_{T,3D} = blkdiag(\boldsymbol{T}_T, \boldsymbol{T}_T, \boldsymbol{T}_T)$ is obtained by rearranging the interpolation matrix. Applying the same model order reduction as in subsection 3.2.2 the interpolation matrix reduces into a modal interpolation matrix $\widetilde{\boldsymbol{T}}_T \in \mathbb{R}^{3M_a \times N}$ and eq. (3.40) turns into eq. (3.41) where the outer surface of the wing is split up into an upper and lower surface ($k = \{u, l\}$).

$$\vec{u}_{a,k} = \widetilde{\boldsymbol{T}}_{T,k} \vec{q}, \; k = \{u, l\}. \tag{3.41}$$

For the calculation of the structural induced velocities on the aerodynamic mesh a similar approach can be used as depicted in eq. (3.42) and the modal interpolation matrix remains unchanged.

$$\vec{V}_{el,k} = \widetilde{\boldsymbol{T}}_{T,k} \vec{\dot{q}}, \; k = \{u, l\}. \tag{3.42}$$

To interpolate the forces the other way around, from the aerodynamic panels to the structural nodes, the inverse distance weighting method is applied. This implies that the load will be proportional to the inverse of the distance to each aerodynamic node like in eq. (3.43).

$$F_{s,i} = \frac{\|\vec{x}_a - \vec{x}_{s_i}\|}{\sum_{k=1}^{n_{s,s}} \|\vec{x}_a - \vec{x}_{s,k}\|} \cdot \boldsymbol{F}_a \tag{3.43}$$

This equation can then be rewritten in a similar manner as done for the thin spline method. The fraction is taken for each node and rewritten in matrix form to the matrix $T_I \in \mathbb{R}^{n_{s,s} \times M_a}$. Applying then the model order reduction technique again and splitting the equation for lower and upper surface result in eq. (3.44).

$$\vec{f}_{a,k} = \widetilde{\boldsymbol{T}}_{I,k} \vec{F}_a, k, \; k = \{u, l\}, \tag{3.44}$$

where $\vec{f}_{a,k}$ are the aerodynamic forces in structural (modal) coordinates for upper and lower surface, $\tilde{\boldsymbol{T}}_{I,k}$ the modal interpolation matrices and $\vec{F}_a, k$ the aerodynamic forces.

Knowing $\vec{f}_a$, the new locations of the structural coordinates can be obtained solving the equations of motion given in eq. (3.5) for static deformation. Such a loop is one iteration of the FSI and this is performed several times until two convergence criteria are met. One of which is the displacement and the other the lift forces. Typically the FSI converges after two iterations for reasonable change in angle of attack and aircraft velocity. Larger changes usually require less than 6 iterations which makes the FSI framework a quick and powerfull method of calculating the aircraft forces during the power cycle simulations. An abstract of the iteration cycle can be seen in figure 3.7.

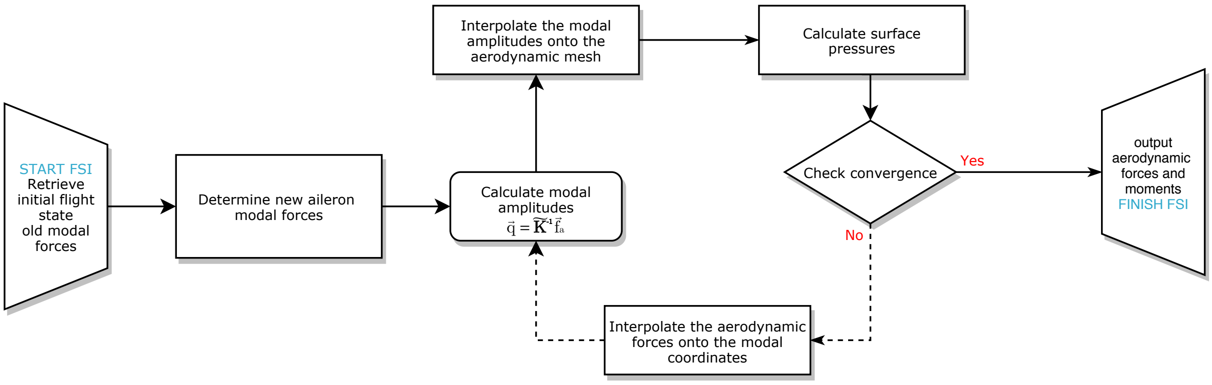

Figure 3.7: Flowchart of the FSI iteration cycle.

3.5.2. FSI - flight dynamics interface

The FSI solver and the flight dynamics model are coupled to solve the actual forces and moments produced by the main wing at each sampled time step. As the simulation ordinary differential equation solver uses a variable time step, some iterations are having a very short period of time between them, increasing the simulation time significantly when using the FSI iterative solver. For this it is chosen to sample the FSI every 0.01 s, making the simulation a lot less computationally expensive while the dynamics of the wing are still captured accurately. This is combined with the maximum time step of the ordinary differential equation solver, which is set to 0.01 s. Choosing a larger sampling time for the FSI is observed to introduce unphysical wing behaviour inducing sudden actuator inputs.

The variable step solver used is the Adams-Bashforth-Moulton PECE solver ODE 113 solver, an explanation on the characteristics of the solver can be found in [83] with a comparison to other solvers. The solver is chosen in this context as it outperformed the simulation time of other tried solvers available in the Matlab (simulink) environment. The numerical integration of the coupled model is illustrated in figure 3.8. Here the flight state $\vec{X}$ is composed of the aircraft and tether positions, the Euler angles and the wind velocity.

The total dynamic system shown in figure 3.8 contains 22 degrees of freedom, d_{DS}. These are six degrees of freedom for the aircraft, three degrees of freedom per tether particle and 1 degree of freedom of the ground station. The system can be described by a time derivative of the dynamic state vector and a generalised force vector as shown in eq. (3.45).

$$\boldsymbol{M}_{DS}\dot{\vec{y}} = \vec{F}_{DS}, \tag{3.45}$$

where $\boldsymbol{M}_{DS} \in \mathbb{R}^{d_{DS} \times d_{DS}}$ is the generalised mass matrix, $\vec{y} = (\vec{v}_A, \vec{\omega}_A, \vec{v}_T, \omega_g)^T \in \mathbb{R}^{d_{DS}}$ the dynamic state vector and $\vec{F}_{DS} \in \mathbb{R}^{d_{DS}}$ the generalised force vector. The numerical integration of this system over time is performed using an explicit calculation scheme. This means the state variables at a certain time step is directly calculated from the prior time step.

Each time step, all parameters of the dynamic system are updated except for the aircraft forces and moments which is updated each 0.01 s. It could mean the time step is exactly the same as this sampling time, which means all variables are updated at the same time.

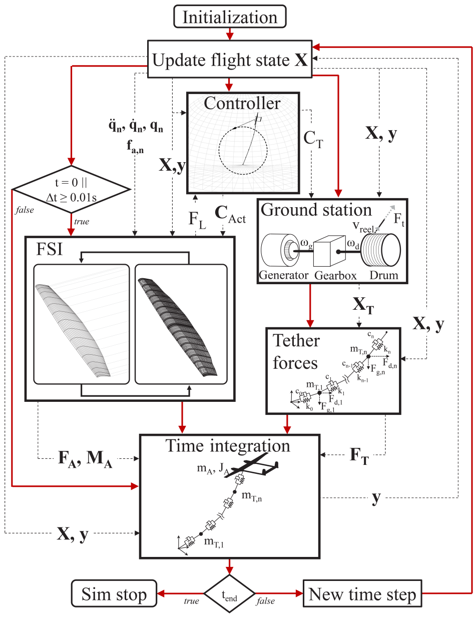

Figure 3.8: Numerical integration of the coupled existing Aero-servo-elastic model [8].

3.6. Convergence studies and initial optimisation objectives

During this thesis, two optimising frameworks were set up. One with only the fluid-structure interaction model and one combining the FSI solver with the flight dynamics model. First, a simple convergence study was performed on the mesh sizes of the structural- and aerodynamics model. Second, the first optimisation is ran to determine the structural parameters. Third, the second optimisation framework is used to determine the controller inputs for the flight dynamics model. These two optimisations were fully decoupled to be able to achieve results within the time frame of this thesis. However, the discussed framework can just as well optimise the structure and controller parameters simultaneously. Unfortunately, the amount of computational power available during this thesis was limited to the use of eight parallel workers.

A "covariance matrix adaptation evolution strategy" (CMAES)[84] optimisation method is applied with a specific objective function dependent on each of the two frameworks discussed above. The objective functions are elaborated on in subsection 3.6.2.

3.6.1. Convergence studies

A convergence study of the structural mesh was performed on the buckling coefficient. There are three parameters mainly determining the element sizes; the chordwise node spacing of the leading edge section; the chordwise nodespacing of the rest of the airfoil; and the spanwise element separation. The spanwise element separation has the biggest influence on the buckling coefficient, because the elements need to be sufficiently small to transfer the stresses accurately as constant stress elements. To simplify the convergence study to one single parameter, the leading edge node spacing is taken one third of the spanwise spacing in order to still accurately catch the leading edge geometry and the rest of the chordwise spacing is taken to be two third of the spanwise spacing.

A convergence study of the aerodynamic mesh was performed on the lift coefficient. Just like for the structural method, one parameter is related to the other. However, the aerodynamic mesh is composed of only two parameters. The ratio between the spanwise and chordwise panels is kept constant, allowing for a simple convergence evaluation. In order to capture the aileron and tip aerodynamic behaviour more accurately, the panels are using cosine spacing to divide the panels in spanwise direction and have a more fine mesh towards the tip.

3.6.2. Generation evolution and objective functions

For the structural optimisation a few parameters were kept constant to limit the computational expense and limit the size of the aircraft. The wing span, the root and tip chord and the airfoil is chosen to remain constant forcing the optimiser to reduce the weight and consequently, to increase the load factor calculated by dividing the lift over weight. Keeping these parameters constant is chosen based on the available computational power. It is noted that changing these parameters have a significant influence on the design, but an initial direction had to be chosen within the available time frame. Varying the internal structure and demonstrating the capability of increasing the critical load factor of the wing is therefore picked as the preferred objective. The shape and size of the wing are by far the biggest contributor to the amount of lift the wing can produce. When the lift stays approximately constant, the load factor can only be increased by lowering the weight. This is then done by changing the number of ribs and changing all the layup parameters, making sure the wing has a buckling factor of at least 1.5. The buckling is assumed to be the critical failure mode. However, this might not always be the case and needs to be verified. Buckling is the phenomena where a member of the structure becomes unstable showing unwanted deformations before the failure load of the material. This lowers the load carrying capabilities of this member and consequently result in structural failure.

The objective function of the structural model is defined as following. First the FE model of the wing is set-up and fed in to MSC.Nastran to obtain the stiffness and mass matrices. The FSI is then run to determine the loads in an aeroelastic static solution. These loads are then fed back in MSC.Nastran for a buckling analyses with the loads calculated by the FSI module. The buckling analyses will supply the buckling coefficient. The load factor is determined by dividing the lift by the weight. However, it has to be noted this is not the actual load factor, as the buckling load is the lift multiplied by the buckling coefficient. After these parameters are determined, a flutter speed calculation is done checking whether the flight speed is exceeding the flutter speed. If either the buckling coefficient is below 1.5 or the flutter speed is lower than the envisioned flight speed, the load factor is penalised to trick the algorithm that the result is not desired. Choosing very high parameters as the initial guess and making sure the wing satisfies the non-penalty criteria, the optimiser can find a lighter wing. The Matlab code which calculates the objective function value from the simulation output is given in appendix B.1.

The objective function for the power optimisation is relying on running the full flight dynamics model for 200 s. After 60 seconds, the average power and distance to the flight path are estimated over a full cycle. A few criteria have to be met before the average power is accepted as valid and to make sure the aircraft would not have crashed during its flight. The first, criteria is the power cycle time, this is set to a minimal of 2 seconds. The second, is the percentage difference between average produced power of two cycles, which is set to a maximum of 2%. This determines if a steady state power production is reached. The third, criteria is to check whether the aircraft had crashed into the ground. The fourth, is the tether force exerted on the aircraft. The tether force may not exceed the buckling load. The fifth criteria, is the flutter speed, however observing the results it is found this criteria was always met. The final criteria, is the flight path error. The average distance between the aircraft and the desired flight path is measured over a power cycle and checked if this is below 5% of the radius of the desired circular trajectory. The flight path is mainly penalised because for this reference system an initial system capable of flying a desired trajectory is of more value. Whenever any of these criteria are not met, a penalty is given to the power. This forces the optimiser to find a solution meeting all criteria, and maximises this value in the process. The Matlab code which calculates the objective function value from the simulation output is given in appendix B.2.

For the final power curve of this system a different objective is used to find parameter sets that work at lower wind speeds. Two additional corrections are applied to the power. When power is produced, the power is divided by the value calculated in eq. (3.46). When power is needed by the system, in other words, using the system cost the user electricity, the power is multiplied by the value calculated in eq. (3.47). The functions given were found to be effective by trial and error on a test power curve. Any other function which makes the lower power at lower wind speeds more optimal would be possible to use. The Matlab code which calculates the objective function value from the simulation output is given in appendix B.3.

$$F_{prod} = \exp\left(V_w \cdot 0.9\right) \tag{3.46}$$

$$F_{loss} = \frac{\exp\left(V_w^{0.0001}\right)}{2000} \tag{3.47}$$

4 Results: system design and performance

The performance of the presented reference airborne wind energy system is shown throughout this chapter. First, the initial two system optimisations are shown in section 4.1. Here the mesh sizes, structural optimisation and flight dynamics controller input results are depicted. Second, the reference system design parameters are elaborated on in section 4.2. Last, the reference system performance throughout a full simulation power cycle is demonstrated in section 4.3.

4.1. Initial optimisations

During this thesis, the two optimising frameworks are run to determine the reference system design parameters. One with only the fluid-structure interaction model and one combining the FSI solver with the flight dynamics model. First, the result of the mesh convergence study are shown in subsection 4.1.1. Second, the results of the structural and flight dynamics optimisation are presented in subsection 4.1.2. The objective functions used, are elaborated on in subsection 3.6.2.

4.1.1. Mesh cell sizes

Subsection 3.6.1 describes the choices for the convergence studies and the determined values are presented in this subsection. Table 4.1 shows the wing planform parameters used for the mesh generation. For the FEM mesh a spanwise spacing of 0.2 m is found to sufficiently determine the buckling coefficient. This implies a leading edge spacing of 0.07 m and a 0.13 m spacing over the rest of the chord. Figure 4.1 shows 10 spanwise panels per half-span should be sufficient to determine the lift accurately enough on the aerodynamic mesh, the result is within 1% of the last examined value. This results in 18 chordwise panels and adding up to a total of 720 panels.

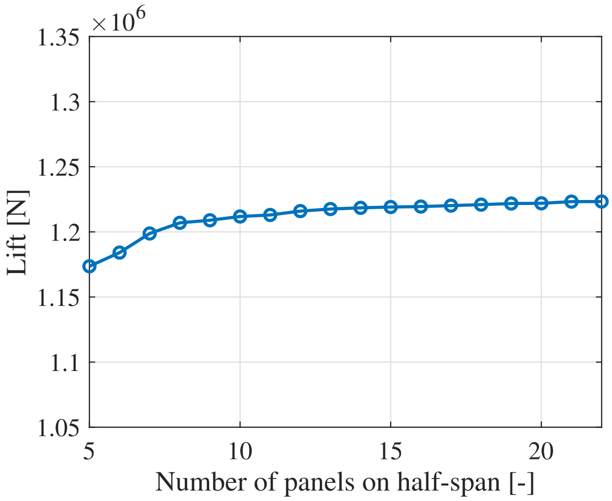

Figure 4.1: Convergence on the lift force for a different number of aerodynamic panels.

4.1.2. Generation evolution and objective functions

The load factor evolution of the structural optimisation over many iterations is like depicted in figure 4.2.

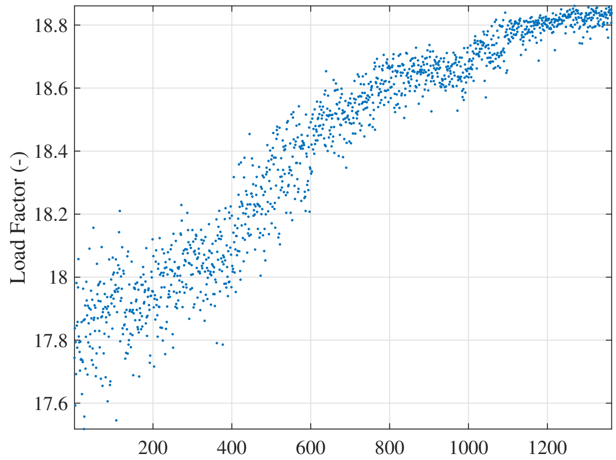

Figure 4.2: Non-penalised load factors during the structural optimisation process.

Here, the load factor represents the lift force over the aircraft weight. As the minimum buckling factor required for no penalty is 1.5, the actual buckling factor at the highest point in figure 4.2 is 1.557. At this point, the lift is 1.2036×10^6 N which makes the maximum load factor the aircraft can endure before buckling equal to 29.47. However, it should be noted a better way to optimise the load factor would be to take the buckling factor into account in the calculation of the objective function outcome, and not only to use it for a penalty criteria. This way the actual load factor is optimised and not just the reference case load factor which is calculated for one specific angle of attack and flight speed. It must be noted that the buckling load might not be the failure load in a later stage. Currently, the loads are not allowed to exceed the buckling load at which the maximum composite direct stress failure index is 0.97. This is calculated by MSC.Nastran and extracted by the software HyperView (part of HyperWorks). This indicates that the internal stresses do not exceed the material failure load when buckling occurs. However, in future studies a closer look to material properties and the critical failure mode must be performed to obtain accurate results.

The evolution of the actual power production (not objective function) is shown in figure 4.3, this is the power coming out of the flight dynamics simulation and no penalties are applied yet. Here, the power and non-penalised power are compared. Non-penalised power data points are the power where no penalties are applied, thus a valid power production of the corresponding simulations. The tendency of lowering the power towards more optimiser iterations is mainly caused by the distance to the flight path. Even though no flight path penalty is applied, it was chosen for this initial optimiser to multiply the objective function value with a factor corresponding to its diversion of the desired trajectory. This causes the optimiser to follow the trajectory in a more accurate way at the expense of the power output.

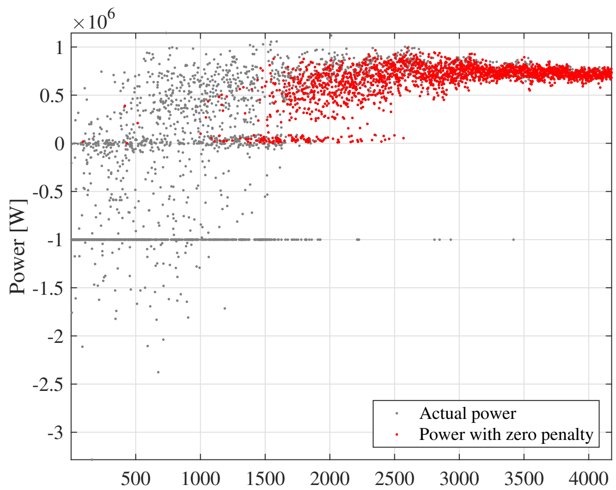

Figure 4.3: Actual power during the optimisation process compared to the non-penalised actual power.

4.2. System design parameters

This chapter describes the system design parameters of the Airborne Wind Energy Reference System described throughout this thesis. First, the planform of the main wing is explained in subsection 4.2.1. Second, the details on material choices and composite layup are elaborated on in subsection 4.2.2. Third, subsection 4.2.3 presents the airfoil chosen and gives the reasoning. Last, the important parameters used in the flight dynamics simulation are given in subsection 4.2.4.

4.2.1. Wing planform

As mentioned before, the AP4 [7] was taken as a reference aircraft for the design of this reference system. As not much is published yet for the AP4 aircraft, the published planform type for the AP3 aircraft is taken instead [6] assuming the AP4 is more or less an upscaled version of the AP3 aircraft. A twin-fuselage configuration is chosen, which contributes to the benefit of having appropriate tether clearance during take-off and landing. This configuration also allows the necessary propulsion power to be divided over two propellers, one at the front of each fuselage. The tether is connected under the main wing as close to the centre of gravity as possible. It is chosen to use only one tether. However, multiple tethers can provide a beneficial amount of redundancy and safety. The Ampyx Power AP3 aircraft uses only one tether in the centre of gravity. Multiple tethers significantly increases aerodynamic drag and thus decreases the power output. Combining this with the additional material and maintenance costs, the price of energy will increase which is a big disadvantage on the economic market [11].

In the flight simulations, shown in chapter 4, it is attached at the centre of gravity calculated by MSC.Nastran which is shifted by including two single point masses of 200 kg each as the propellers in the front end of each fuselage. The centre of gravity is measured from the leading edge (the x=0 node of the airfoil). The AP4 wing span is adapted slightly, combining it varying a root and tip chord that result in both a 150 m^2 surface area and an aspect ratio of 12. The airfoil selection is explained in subsection 4.2.3. The front and back spar position and total number of ribs were determined by the optimiser to maximise the wing load factor. The ailerons are sized following the design approach of [85]. The ailerons are then extended from 60 to 90% of the halfspan. The 10% left at the wing tip is not used for the aileron as the vortex flows present here provide little control effectiveness. Historical guidelines show that for 30% of the chord, typically the aileron chord takes up about 25% of the wing section chord. The sweep is taken rather small. Sweep is mostly introduced for aerodynamic reasons, increasing the flight speed at which shockwaves are created on the wing. However, a swept back wing tends to have a higher divergence speed than an unswept wing [86]. No large sweep is necessary for shockwave prevention, mainly because the flight speed regime is at the lower Mach number scale and shockwaves will not occur. Also, keeping the sweep low increases the general efficiency of the wing by attaining a high aspect ratio at similar span.

As the focus of this thesis is mainly on the internal structure of the main wing and setting up a framework that could potentially optimise a full system to increase its power production performance, the design of the two tail sections are solely dependent on scaling. The horizontal and vertical stabiliser are sized by determining the ratios, Ampyx Power used for the tail sections compared to the wing span. These ratios are determined by comparing several published articles and pictures of the AP3. This resulted in the dimensions presented in table 4.1. However, the stability of the aircraft is monitored closely throughout the simulations to make sure the aircraft can perform its power cycle.

A visual representation of the wing is shown in figure 4.4. Here, a few of the main dimensions are shown on the envisioned design. Table 4.1 gives brief summary of planform parameters of the main wing, fuselages and tail. For each parameter it is specified whether it is a constant chosen value/airfoil or it is a result from the optimisation runs. However, a constant value does not mean it cannot be varied by the optimiser, it is just chosen to be one persistent parameter during the optimisation process to reduce the computational effort.

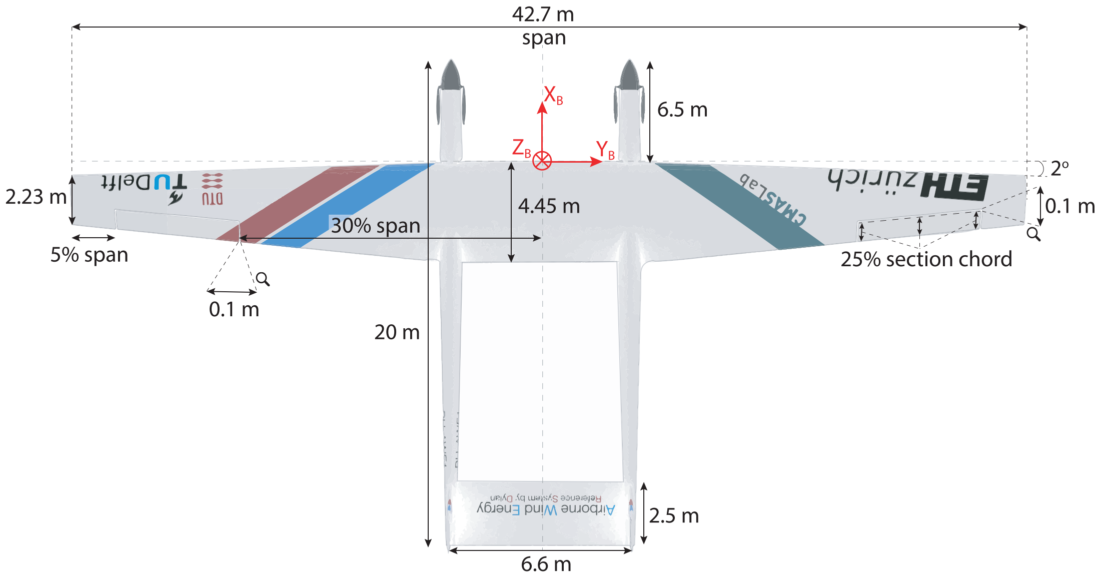

Figure 4.4: Wing planform (top view).

Table 4.1: General planform parameters of the wing, tail and fuselage. Contant (=C) or Optimiser outcome (=O).

Parameter		**Value**	**C/O**
Center of Gravity	[m,m,m]	-1.67, 0, 0.229	O
Total aircraft mass	[kg]	6885.2	O
Wing:			
Span	[m]	42.7	C
$\text{Chord}_{\text{root}}$	[m]	4.45	C
$\text{Chord}_{\text{tip}}$	[m]	2.23	C
LE Sweep	[°]	2	C
Aspect Ratio	[-]	12.1	C
Surface Area	[m²]	150.3	C
$\text{Airfoil}_{\text{root}}$	[-]	RevE_{HC}	C
$\text{Airfoil}_{\text{tip}}$	[-]	RevE_{HC}	C
Front spar	[% c_{local}]	33.3	O
Back spar	[% c_{local}]	43.4	O
$\text{Aileron}_{\text{root-inner rib}}$	[% $b_{1/2}$]	60	C
$\text{Aileron}_{\text{root-outer rib}}$	[% $b_{1/2}$]	90	C
$\text{Aileron}_{\text{LE-spar}}$	[% c_{local}]	75	C
Total number of ribs	[-]	50	O
Horizontal Tail/Elevator:			
Span	[m]	6.7	C
Chord	[m]	2.5	C
Airfoil	[-]	NACA 0012	C
Vertical Tail:			
Span	[m]	3	C
Chord	[m]	2.8	C
Airfoil	[-]	NACA 0012	C
Fuselages:			
Length	[m]	20	C
Radius	[m]	0.6	C
$X_{\text{Nose-LE}_{\text{wing}}}$	[m]	6.5	C
$Y_{\text{Root-Fuselage}}$	[m]	3.8	C

Table 4.2 shows a detailed description of the wing planform necessary in combination with table 4.1 to reconstruct the wing. Each Z position is measured from the root in spanwise direction. The chord is

the actual chord length of the rib. The twist is the structural rotation of the airfoil sections in order to achieve higher angles of attack at the root and lower at the tip to reduce the lift induced drag. Another benefit from this is to make sure the root stalls before the tip. This makes sure the ailerons can still function properly when the first signs of stall are present [87]. The twist is kept constant throughout the optimisation process. $d_{x,sweep}$ is the chord wise distance each airfoil is moved backwards to account for sweep and is measured from the unswept leading edge position. The Rot_z is the angle the rib is rotated to become perpendicular to the trailing edge. The trailing edge is swept forward to increase the aspect ratio of the wing.

Table 4.2: Semi-wing detailed planform description.

Z [m]	**Chord** [m]	**Twist** [°]	$\mathbf{d_{x,sweep}}$ [m]	$\mathbf{Rot_z}$ [°]
0	4.45	5	0	0
0.155	4.45	5	0	0
0.88833	4.45	5	0	0
1.7217	4.45	5	0	0
2.555	4.45	5	0	0
3.3881	4.4498	5	-0.00087445	1.8359
4.2224	4.4085	5	-0.015449	1.8359
5.0523	4.3265	4.7511	-0.043557	4.7806
5.891	4.2274	4.4995	-0.072845	4.7806
6.7179	4.114	4.2515	-0.10172	5.8894
7.5587	3.9985	3.9993	-0.13108	5.8894
8.3846	3.8851	3.7516	-0.15992	5.8894
9.2254	3.7696	3.4994	-0.18928	5.8894
10.0513	3.6562	3.2516	-0.21812	5.8894
10.8921	3.5407	2.9995	-0.24749	5.8894
11.7179	3.4273	2.7517	-0.27633	5.8894
12.5587	3.3118	2.4995	-0.30569	5.8894
13.3846	3.1984	2.2518	-0.33453	5.8894
14.2254	3.0829	1.9996	-0.36389	5.8894
15.0513	2.9695	1.7519	-0.39273	5.8894
15.8921	2.854	1.4997	-0.42209	5.8894
16.7179	2.7406	1.252	-0.45093	5.8894
17.5587	2.6251	0.99982	-0.48029	5.8894
18.3846	2.5116	0.7521	-0.50913	5.8894
19.2254	2.3962	0.49991	-0.53849	5.8894
20.0513	2.2827	0.25219	-0.56733	5.8894
20.8921	2.1673	0	-0.59669	5.8894

4.2.2. Material choices and detailed composite layup

The two materials used for the composite layers in this section are defined in table 4.3. In MSC.Nastran these materials are defined as MAT8 materials. MAT8 materials are orthotropic, in other words, materials containing properties which differ along the three mutually-orthogonal planes of property symmetry.

Table 4.3: Material properties of the 45°and the 0°UD plies.

Parameter		±45°fabric	UD 0°tape
Material type	[-]	MAT8	MAT8
Layer thickness	[m]	0.0002	0.00017
$E_{1,longitudinal}$	[Pa]	3.83×10^{10}	1.12×10^{11}
$E_{2,lateral}$	[Pa]	3.83×10^{10}	6.9×10^{9}
ν_{12}	[-]	0.3	0.3
G_{12}	[Pa]	4.70×10^{9}	9.9×10^{9}
G_{1Z}	[Pa]	4.70×10^{9}	9.9×10^{9}
G_{2Z}	[Pa]	2.35×10^{9}	4.9×10^{9}
ρ	[kg/m³]	1600	1600
$A_{1,thermal}$	[K⁻¹]	0	0
$A_{2,thermal}$	[K⁻¹]	0	0
T_{ref}	[K]	0	0
X_t	[Pa]	8.88×10^{8}	2.10×10^{9}
X_c	[Pa]	8.88×10^{8}	1.73×10^{9}
Y_t	[Pa]	8.03×10^{8}	56.5×10^{6}
Y_c	[Pa]	8.18×10^{8}	56.5×10^{6}
S	[Pa]	1.07×10^{8}	1.02×10^{8}

4.2.2.1. Wing skin

The composite layup of the wing skin panels are designed for the root and tip, while interpolating linearly between to create eight sections. This is done by assigning a number of spanwise skin panels, one determined between two consecutive ribs, to each of the eight sections. Whenever the number of panels cannot be divided by eight, the number of panels is sorted in descending order from root to tip, allowing for more panels with higher thickness at the root. For each skin panel the layup is done with a [45°_N -45°_N 45°_N 0°_N] ply orientation. The thicknesses given to MSC.Nastran are defined as [$.25t_{45}$ $.5t_{45}$ $.25t_{45}$ t_{UD}]. Figure 4.5 shows the distribution of the layup thickness over the wingspan.

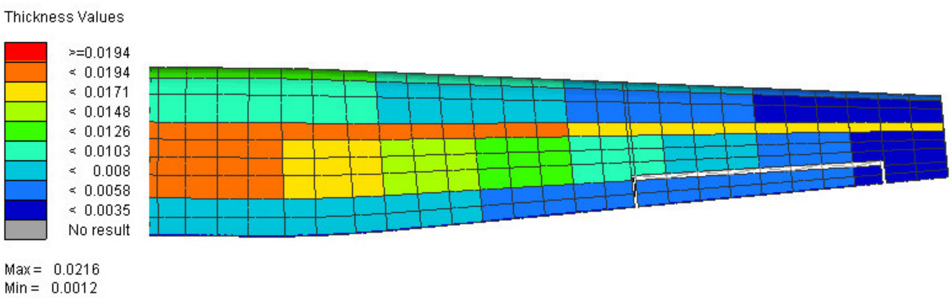

Figure 4.5: Top skin layup thickness distribution.

On both surfaces, top and bottom, it can be noted that one expected feature is happening. The thicknesses increases when moving from the tip to the root visible in figures 4.5 and 4.6. This comes from the bending moment that increases significantly towards the root. In other words, the composite plies have to withstand a higher loading and thus must be stronger. Because of the interpolation method between the root and the tip, no local buckling phenomena can be noted. On the bottom surface is can be clearly seen that the wingbox takes up most of the loads acting on the wing. Also on the top it can be seen that the wingbox has the highest thicknesses. The increased thicknesses present on the rear part of the wing are most likely occurring due to twist in the wing.

From tables 4.4 to 4.7 a couple of other things become clear. The UD layers have a lower stiffness in compression than in tension. This is visible in the wingbox section area where approximately double the amount of UD layers are required by the top layer. However, the UD layer ply used in this thesis is thinner than the ±45°plies, which overall still result in thicker bottom surface wingbox panels. The optimiser chosen to let the bottom wingbox pales take up all the loads where at the top surface it is more spread out over the whole wing section.

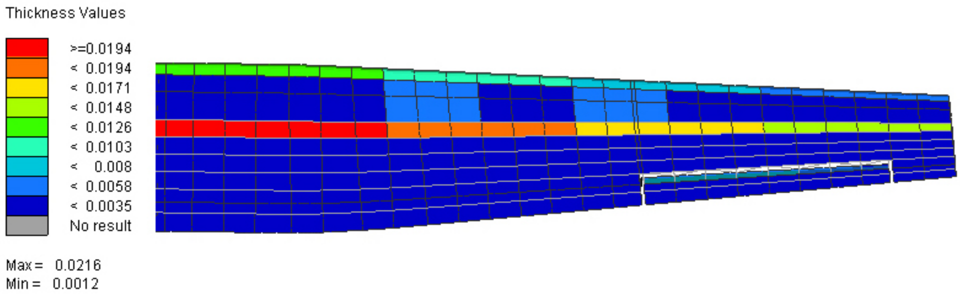

Figure 4.6: Bottom skin layup thickness distribution.

Table 4.4: Number of ±45°layers for each top skin panel.

	Root																								**Tip**
LE	47	47	47	47	44	44	44	39	39	39	35	35	35	31	31	31	27	27	27	23	23	23	19	19	19
	38	38	38	38	33	33	33	28	28	28	23	23	23	18	18	18	13	13	13	8	8	8	2	2	2
	38	38	38	38	33	33	33	28	28	28	23	23	23	18	18	18	13	13	13	8	8	8	2	2	2
Wingbox	14	14	14	14	16	16	16	17	17	17	18	18	18	19	19	19	20	20	20	21	21	21	22	22	22
	82	82	82	82	71	71	71	60	60	60	49	49	49	38	38	38	27	27	27	17	17	17	5	5	5
	82	82	82	82	71	71	71	60	60	60	49	49	49	38	38	38	27	27	27	17	17	17	5	5	5
	82	82	82	82	71	71	71	60	60	60	49	49	49	38	38	38	27	27	27	17	17	17	5	5	5
	28	28	28	28	25	25	25	22	22	22	19	19	19	16	16	16	13	13	13	11	11	11	7	7	7
	28	28	28	28	25	25	25	22	22	22	19	19	19	16	16	16	13	13	13	11	11	11	7	7	7
TE	28	28	28	28	25	25	25	22	22	22	19	19	19	16	16	16	13	13	13	11	11	11	7	7	7

Table 4.5: Number of 0°layers for each top skin panel.

	Root																								**Tip**
LE	10	10	10	10	10	10	10	9	9	9	8	8	8	8	8	8	7	7	7	6	6	6	5	5	5
	10	10	10	10	10	10	10	9	9	9	8	8	8	8	8	8	7	7	7	6	6	6	5	5	5
	10	10	10	10	10	10	10	9	9	9	8	8	8	8	8	8	7	7	7	6	6	6	5	5	5
Wingbox	95	95	95	95	91	91	91	86	86	86	81	81	81	77	77	77	72	72	72	67	67	67	62	62	62
	10	10	10	10	11	11	11	11	11	11	11	11	11	11	11	11	11	11	11	11	11	11	11	11	11
	10	10	10	10	11	11	11	11	11	11	11	11	11	11	11	11	11	11	11	11	11	11	11	11	11
	10	10	10	10	11	11	11	11	11	11	11	11	11	11	11	11	11	11	11	11	11	11	11	11	11
	10	10	10	10	11	11	11	11	11	11	11	11	11	11	11	11	11	11	11	11	11	11	11	11	11
	10	10	10	10	11	11	11	11	11	11	11	11	11	11	11	11	11	11	11	11	11	11	11	11	11
TE	10	10	10	10	11	11	11	11	11	11	11	11	11	11	11	11	11	11	11	11	11	11	11	11	11

Table 4.6: Number of ±45°layers for each bottom skin panel.

	Root																								**Tip**
LE	47	47	47	47	44	44	44	39	39	39	35	35	35	31	31	31	27	27	27	23	23	23	19	19	19
	8	8	8	8	9	9	9	10	10	10	10	10	10	11	11	11	11	11	11	12	12	12	12	12	12
	8	8	8	8	9	9	9	10	10	10	10	10	10	11	11	11	11	11	11	12	12	12	12	12	12
Wingbox	69	69	69	69	63	63	63	57	57	57	51	51	51	45	45	45	39	39	39	33	33	33	27	27	27
	8	8	8	8	8	8	8	8	8	8	8	8	8	8	8	8	8	8	8	8	8	8	7	7	7
	8	8	8	8	8	8	8	8	8	8	8	8	8	8	8	8	8	8	8	8	8	8	7	7	7
	8	8	8	8	8	8	8	8	8	8	8	8	8	8	8	8	8	8	8	8	8	8	7	7	7
	8	8	8	8	8	8	8	8	8	8	8	8	8	8	8	8	8	8	8	8	8	8	7	7	7
	8	8	8	8	8	8	8	8	8	8	8	8	8	8	8	8	8	8	8	8	8	8	7	7	7
TE	8	8	8	8	8	8	8	8	8	8	8	8	8	8	8	8	8	8	8	8	8	8	7	7	7

Table 4.7: Number of 0°layers for each bottom skin panel.

	Root																								**Tip**
LE	10	10	10	10	10	10	10	9	9	9	8	8	8	8	8	8	7	7	7	6	6	6	5	5	5
	10	10	10	10	10	10	10	9	9	9	8	8	8	8	8	8	7	7	7	6	6	6	5	5	5
	10	10	10	10	10	10	10	9	9	9	8	8	8	8	8	8	7	7	7	6	6	6	5	5	5
Wingbox	46	46	46	46	46	46	46	46	46	46	46	46	46	46	46	46	46	46	46	46	46	46	45	45	45
	10	10	10	10	10	10	10	10	10	10	9	9	9	9	9	9	8	8	8	8	8	8	7	7	7
	10	10	10	10	10	10	10	10	10	10	9	9	9	9	9	9	8	8	8	8	8	8	7	7	7
	10	10	10	10	10	10	10	10	10	10	9	9	9	9	9	9	8	8	8	8	8	8	7	7	7
	10	10	10	10	10	10	10	10	10	10	9	9	9	9	9	9	8	8	8	8	8	8	7	7	7
	10	10	10	10	10	10	10	10	10	10	9	9	9	9	9	9	8	8	8	8	8	8	7	7	7
TE	10	10	10	10	10	10	10	10	10	10	9	9	9	9	9	9	8	8	8	8	8	8	7	7	7

4.2.2.2. Spars and ribs

The composite layup of the spar and rib panels are done in an identical procedure. However, a slightly different layup orientation is applied because the biggest loads on the spars and ribs are shear loads. For the spar and rib, the number of layers are interpolated from the root to the tip with a ply orientation given by [45°_N -45°_N 45°_N]. The thicknesses given to MSC.Nastran are defined as [$.25t_{45}$ $.5t_{45}$ $.25t_{45}$].

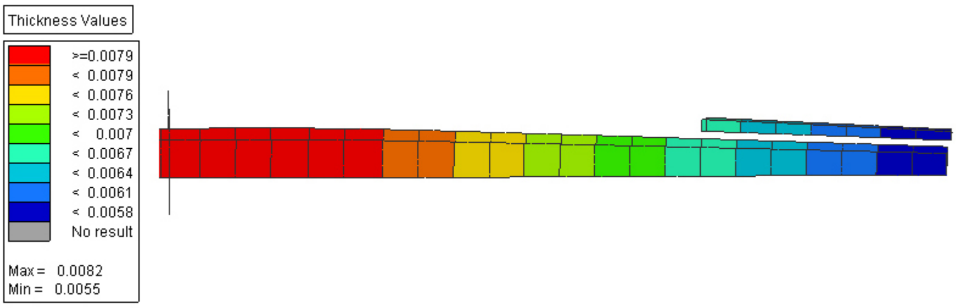

Figure 4.7: Spar layup thickness distribution.

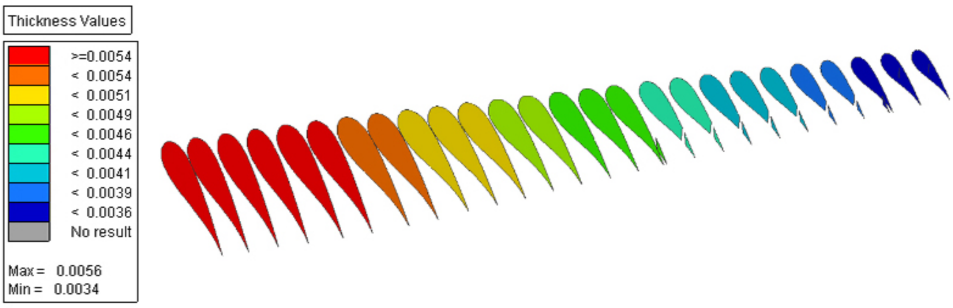

Figure 4.8: Rib layup thickness distribution.

With the current approach, only one thing can be noted in the layup results. Both the spar panels and the rib panels are interpolated only spanwise to adapt to the changes in bending moment which can be seen as expected in figures 4.7 and 4.8. As twist does occur as well, the rib layup could be depicted by more parameters which also changes the layup from leading- to trailing edge. This can potentially decrease the weight of the ribs as a collective. Tables 4.8 and 4.9 provide the number of layers that are in each panel over the wing span.

Table 4.8: Number of $\pm 45^\circ$layers for each spar panel.

Root																								**Tip**
41	41	41	41	41	40	39	39	38	37	36	35	35	34	33	32	31	31	30	29	28	27	27	26	25

Table 4.9: Number of $\pm 45^\circ$layers for each rib.

Root																									**Tip**
28	28	28	28	28	27	27	26	26	25	25	24	23	23	23	22	22	21	21	20	19	19	19	18	18	17

4.2.2.3. Stringers

The composite layup of the stringers is done in a similar matter. However, a less detailed application is used. The layup of the upper and lower stringers are kept constant over the wing span. With the number of layers a certain thickness is determined by multiplying the number of layers with the UD tape layer thickness given in table 4.10. Together with an arbitrary width, a beam model is created using a bar cross-section representation. The geometry and material of the stringers can be found in table 4.10. MAT1 elements are used, MSC.Nastran does not allow other material than MAT1 to be used for beam representations. These materials are isotropic linear and temperature independent materials. The orientation of the plies are lay in $[0°]_N$.

Table 4.10: Geometry and material properties of the upper and lower stringers.

Parameter		Upper	Lower
# Layers	[m]	84	43
Width	[m]	0.05	0.05
Beam cross-section	[-]	BAR	
Material type	[-]	MAT1	
Layer thickness	[m]	0.00017	
E	[Pa]	1.35×10^{11}	
G	[Pa]	5.315×10^{10}	
ν_{12}	[-]	0.27	
ρ	[kg/m^3]	1580	
A	[K^{-1}]	0	
T_{ref}	[K]	0	

4.2.2.4. Fuselages and tail

The composite layup of the fuselages and tail is done in a similar matter as the stringers. However, a different material is used. With the number of layers a certain thickness is determined by multiplying the number of layers with the ±45° fabric thickness given in table 4.11. Together with an arbitrary fuselage length and radius, a beam model is created for the fuselage using a tube cross-section representation. The composite thickness of the tail is combined with a span and chord into a box cross-section representation. The geometry and material of the fuselage and tail can be found in table 4.11. The orientation of the plies are lay in $[\pm 45°]_N$.

Table 4.11: Geometry and Material properties of the fuselage and tail.

Parameter		Fuselage	Tail
# Layers	[m]	9	13
Length/Span	[m]	20	6.7
Radius/Chord	[m]	0.6	2.5
Beam cross-section	[-]	TUBE	BOX
Material type	[-]	MAT1	
Layer thickness	[m]	0.0002	
E	[Pa]	1.4×10^{11}	
G	[Pa]	9.8×10^{9}	
ν_{12}	[-]	0.3	
ρ	[kg/m^3]	1600	
A	[K^{-1}]	8×10^{-8}	
T_{ref}	[K]	0	
S_t	[Pa]	3×10^{8}	
S_c	[Pa]	3×10^{8}	
S_s	[Pa]	1.5×10^{8}	

4.2.3. Airfoil selection

Airfoil design can have a significant effect on aircraft performance. An Airborne Wind Energy aircraft has an additional source of drag, namely the attached tether, which causes extreme additional drag forces. Previous research on what airfoils might be suited for AWE applications is hard to find. Up to the authors knowledge only three documentations are found. Two of them [88, 89] are not taking the tether drag into account when optimising the airfoil shape. However, [88] does discus the phenomenon of the added drag in his conference talk. The third publication uses a multi-Re optimisation of power production and building height on the airfoil shape taking into account an approximation of the tether drag [90]. The added drag is approximated by eq. (4.1) and added to the power production cost function [91].

$$C_{d,added} = \frac{1}{4}\frac{A_c}{A_k}C_{D,c}, \tag{4.1}$$

where A_c is the cable frontal area, A_k is the kite area and $C_{D,c}$ is the cable drag coefficient. Throughout Kroon his analysis, the $C_{D,c}$ is assumed to be 1.1, taken a cylindrical shape into account. Assuming a relatively long tether, the $\frac{A_c}{A_k}$ ratio analysed is 1.33 resulting in a Pareto front. From this front, two interesting airfoils are shown, a 35% and a 25% thickness airfoil visualised in figure 4.9. An airborne wind energy wing should be able to withstand a much higher wing loading than on regular aircraft wings [8]. In order to do this, just like the root of a wind turbine blade, thick airfoils are necessary to produce this resistance to structural deformation.

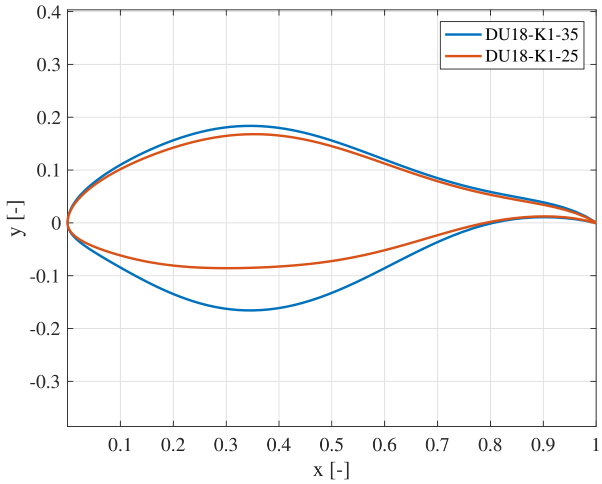

Figure 4.9: 35% and 25% t/c airfoils on Pareto front at A_c/A_k=1.33 [90].

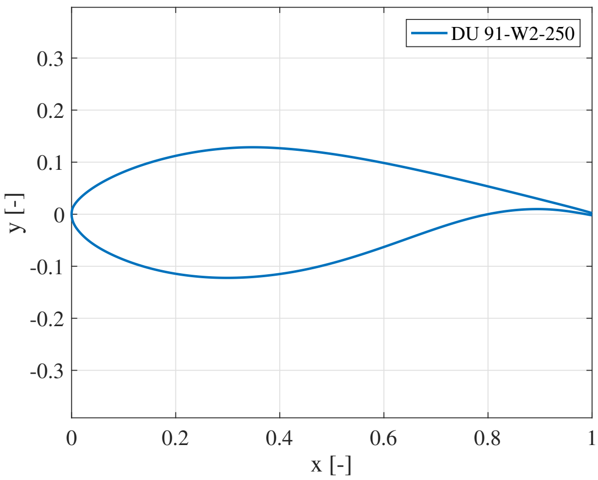

Figure 4.10: DU 91-W2-250 horizontal axis wind turbine airfoil shape [92].

Even though Kroon his method still has a lot of room for improvement and a shift towards more accurate and optimal airfoil designs, his findings show that the added drag of the tether and necessary high lift capabilities outweigh the airfoil drag penalty when optimising theoretical power production. This results in thick high maximum lift airfoils.

Another possible airfoil shape is reversed engineered in this thesis from the pictures published by Makani of the M600, namely "MRevE". From this, a second version is designed with a slightly smoother surface "MRevE-v2". A third profile "MRevE-v2$_{HC}$" is designed with the help of the software, JavaFoil [93], increasing the camber of the airfoil to increase the lift coefficient even more. Makani and Ampyx Power both use separate high lift devices in order to increase the lift. The current state of the aerodynamic model is not able to solve these multielement airfoils (slotted flaps and \or slats) and therefore it is chosen to use a single element airfoil without flaps and is the camber adjusted to produce more lift. All three reverse engineered profiles are shown in figure 4.11.

The maximum thickness and camber values can be found in table 4.12 together with the position along the chord.

Table 4.12: Maximum thickness and camber values for reverse engineered airfoils "MRevE","MRevE-v2" and "MRevE-v2$_{HC}$"

	$\frac{t}{c}$ @ $\frac{x}{c}$	$\frac{f}{c}$ @ $\frac{x}{c}$
MRevE	29.1% @ 30.9%	5.9% @ 36.2%
MRevE-v2	29.2% @ 31.4%	6.1% @ 36.7%
MRevE-v2$_{HC}$	28.6% @ 31.4%	9.0% @ 41.1%

Using an airfoil analysis tool called RFOIL [66], the two airfoils from figure 4.9 and three airfoils from figure 4.11 are analysed and its 2D characteristics are illustrated. RFOIL is designed at TU Delft to better simulate the airfoil characteristics close to and post stall. As mentioned in subsection 3.3.1, the simulation is stopped when the stall angle of attack is exceeded. Therefore, the exact post-stall behaviour

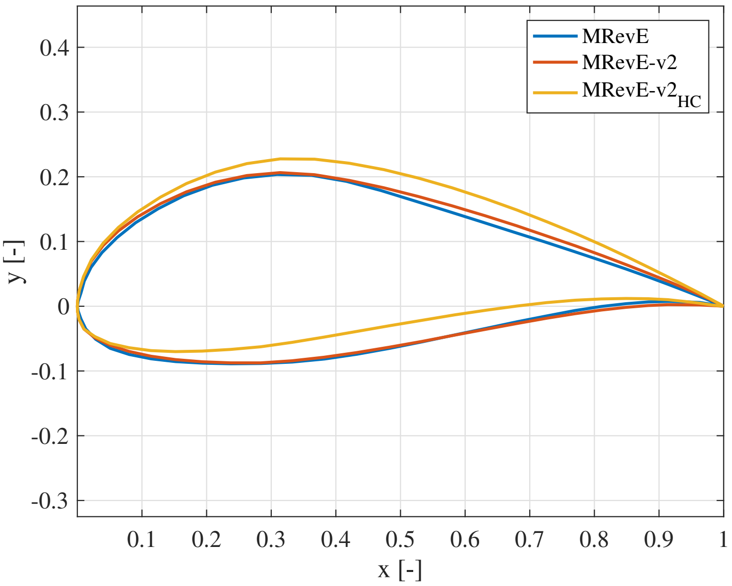

Figure 4.11: Reverse engineered airfoil designs "MRevE","MRevE-v2" and "MRevE-v2$_{HC}$"

of the airfoils is not studied in this thesis. Each airfoil is analysed for the angle of attack range -10°to 20°, at $\mathfrak{R} = 12.0 \times 10^6$ and $M = 0.2351$.

The performance of the two airfoils from figure 4.9 are demonstrated in figure 4.12 and accompanied by the 25% thickness DU 91-W2-250 horizontal axis wind turbine airfoil (see figure 4.10).

From the 25% and 35% DU K1 airfoils, especially the 35% airfoil shows a quite well performance. Clearly visible is that the optimiser takes the airfoil drag much less into account as the total drag of the airfoil and tether is used in the Re function. From figure 4.12 it is observed that the airfoils from around 10° angle of attack, have a significant higher drag than the DU 91-W2-250 airfoil designed for horizontal axis wind turbine blades.

The models used in [90] still have room for a lot of improvement and therefore it is chosen not to proceed with these designs. Assuming Makani did study its airfoils thoroughly, their design would be a better fit for this reference model. The chosen airfoil shapes are then interpolated to each rib position by linear interpolation of each node at the root to its corresponding node at the tip.

First thing that becomes clear here is that a lot of angle of attack inputs, in the around- and post-stall region, did not converge for the MRevE (v1) profile. This is mainly because the reverse engineering is done from scanning an image, resulting is a non smooth top surface and an overall irregular shape. As expected, from increasing the camber of the airfoil, a higher lift and lower drag performance emerges. Also the MrevE-v2$_{HC}$ shows a small improvement on stall behaviour: higher stall angle and a smaller decline rate in lift in the post-stall region. Even though an increased drag is present, the higher lift and better stall behaviour is preferred in tethered flight. Therefore, the MrevE-v2$_{textHC}$ is chosen in this thesis to proceed with (coordinates are found in appendix A). Figure 4.14 illustrates the performance at four different Reynolds numbers. The Reynolds numbers are chosen by taking the root and tip chord size, 4.45 m and 2.23 m, each at 30 m s^{-1} and 80 m s^{-1}, respectively (A low and high flight speed which could be present in a power cycle of the AWES).

Just looking at the 2D characteristics of this airfoil, it can be noted that the airfoil is expected to stall earlier at the tip than at the root. At the same speed and a smaller chord length (e.g. smaller Reynolds number), stall occurs at a smaller angle of attack.

In the design of the reference model, just like at Makani, the airfoil shapes at the root and tip are chosen to be the same. From the publications it is derived that the shapes at the root and tip are approximately similar. It is noted that the load case of the Makani aircraft is different than for the aircraft presented in this thesis, no change to the airfoil design philosophy is applied whatsoever. The shape is therefore only scaled to the specific chord and rotated by the structural twist angle determined in the structural optimisation.

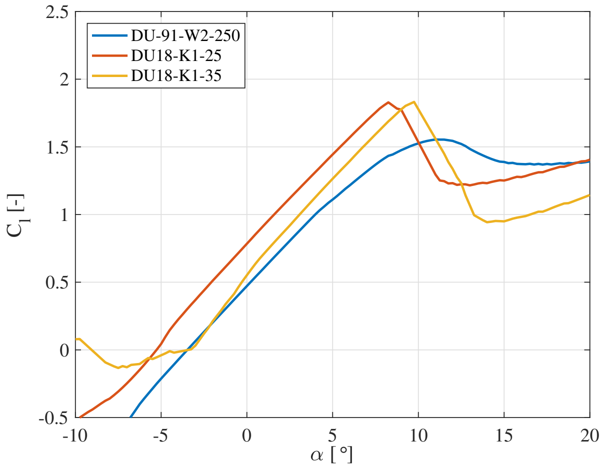

(a) Lift coefficient versus Angle of Attack.

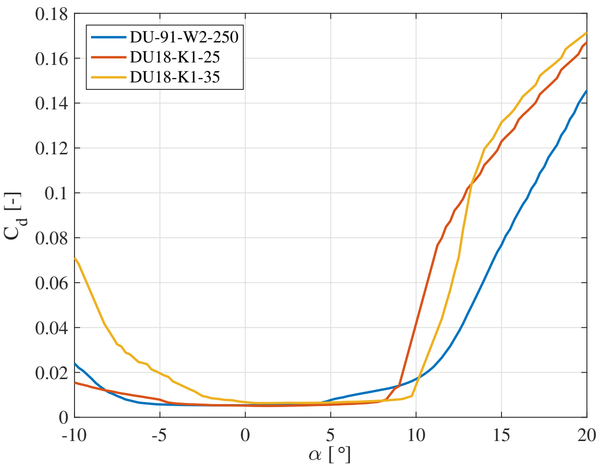

(b) Drag coefficient versus Angle of Attack.

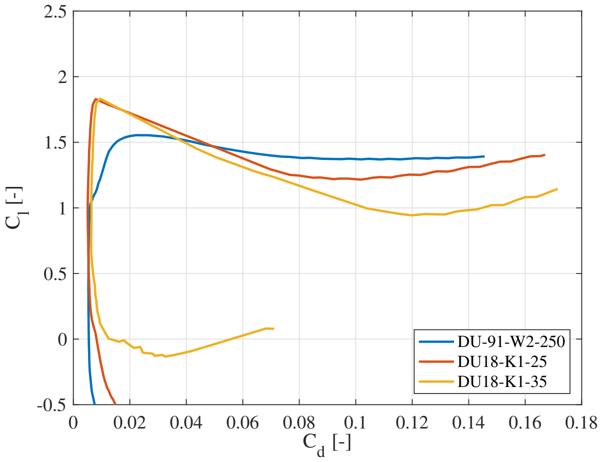

(c) Lift coefficient versus Drag coefficient.

Figure 4.12: Airfoil performance of DU-K1-* shapes from [90] compared to the DU 91-W2-250 HAWT profile @ $\mathfrak{R} = 12.0 \times 10^6$ and $M = 0.2351$.

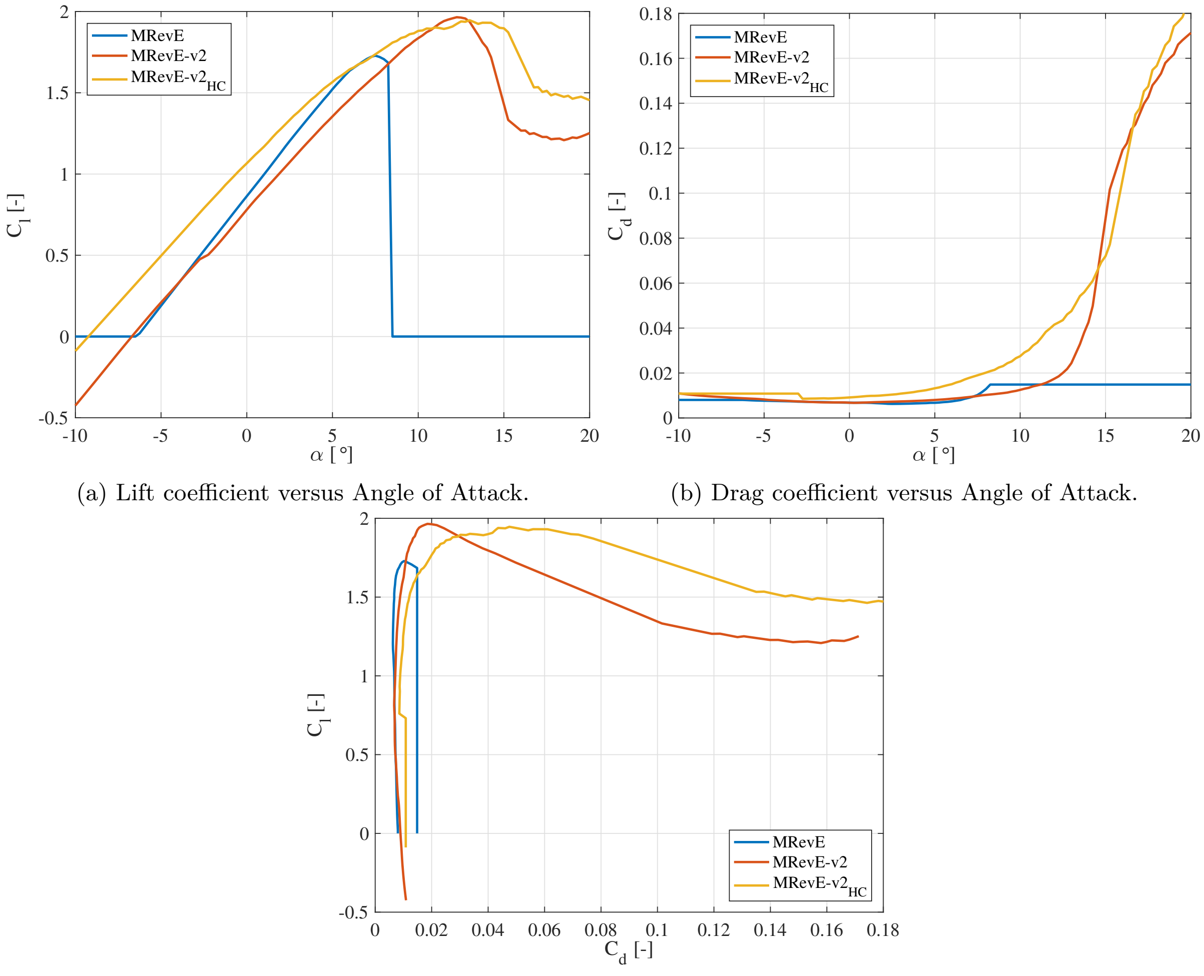

(a) Lift coefficient versus Angle of Attack.

(b) Drag coefficient versus Angle of Attack.

(c) Lift coefficient versus Drag coefficient.

Figure 4.13: Airfoil performance of the reversed engineered shapes in this thesis @ $\mathfrak{R} = 12.0 \times 10^6$ and $M = 0.2351$.

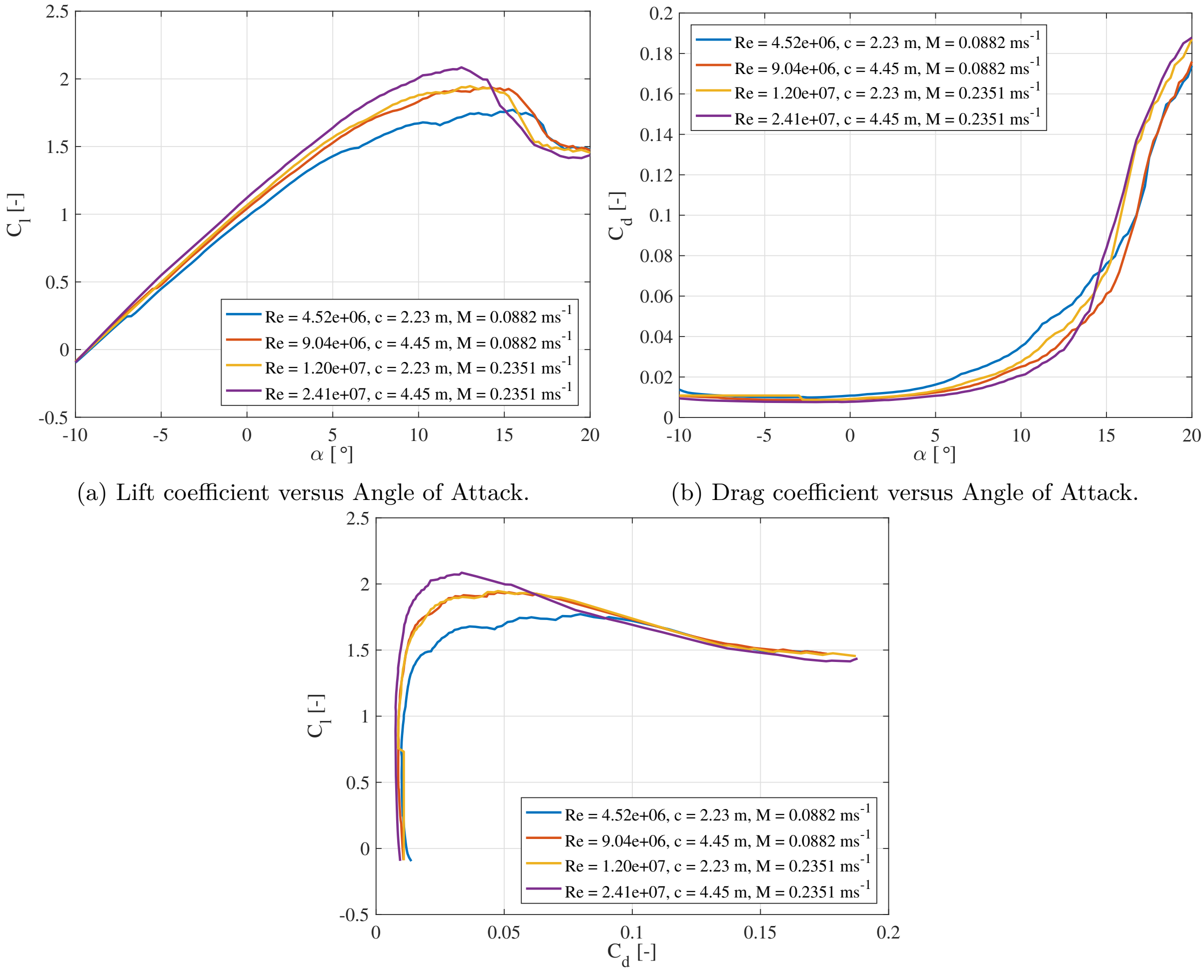

(a) Lift coefficient versus Angle of Attack.

(b) Drag coefficient versus Angle of Attack.

(c) Lift coefficient versus Drag coefficient.

Figure 4.14: Airfoil performance of the MrevE-v2$_{HC}$ @ $\mathfrak{R} = 4.52 \times 10^6$, 9.04×10^6, 12.0×10^6 & 24.1×10^6 and $M = 0.0882$ & 0.2351.

4.2.4. Flight dynamics parameters

For the flight dynamics model, all parameters presented as controller gains, Fourier coefficients and flight path are obtained from an optimisation process where the parameters are changed to obtain a higher average power output without exceeding the buckling load and wing flutter speed. More details on the Re function of the optimiser are given in subsection 4.1.2. The optimiser is limited to the parameters given here. Therefore, the system parameters are not considered as optimal but rather just an initial proposition. The main goal here is the visualisation of the power producing capabilities of a system at this scale, and with this controller and inputs the results presented in chapter 4 can be obtained.

First, the controller gains are presented and explained in sub-subsection 4.2.4.1. Second, the Fourier coefficients for the desired tether length and angle of attack are explained in sub-subsection 4.2.4.2. Last, the necessary dimensions of the tether and ground station to run a full power production cycle are given in sub-subsection 4.2.4.3.

4.2.4.1. Controller gains and flight path

As mentioned before, the controller gains and desired flight path parameters were obtained in an optimisation algorithm. However, the roll attitude gain (Attitude roll P) is determined by observing the flight behaviour. The initial optimisation depended on a simulation without the FSI model running and leaned on a simple model for aerodynamic behaviour. The controller gain found by the optimiser could not cope with the difference in aerodynamic performance when introducing the FSI. A higher rolling moment was the main cause for the controller to fail to counteract the error and made the aircraft diverge from its desired flight path until crashing into the ground. Significantly increasing the roll attitude gain to 500 solved the issue and made the aircraft fly its trajectory again as intended. Due to time constraint, a second optimisation was not performed and the results presented in section 4.3 are accepted to be less optimal than might have been possible in the current framework. Two other parameters are not changed by the optimiser. These are the tether length as well as the proportional and integrator reel-out gains. The behaviour of the controllers was found to be accurately enough and left unchanged to speed up the optimiser. Table 4.13 shows the final parameters which are used for each of the simulations throughout section 4.3.

Table 4.13: Controller gains gains and flight path description.

Parameter		Value
L1 distance	[m]	418.2790
Attitude roll P	[-]	500
Attitude roll I	[-]	0.9306
Attitude alpha P	[-]	293.9
Attitude alpha I	[-]	4.007
Rate Roll P	[-]	69.59
Rate Pitch P	[-]	19.60
Tether length Gain	[-]	10
Reel out speed P	[-]	200000
Reel out speed I	[-]	20.05
l_0	[m]	550.7
Elevation	[°]	47.05 degrees
Radius	[m]	265.5

4.2.4.2. Desired tether length and angle of attack

The power generated by the system is highly dependent on the reel-out speed and the force at which the tether pulls on the winch. As mentioned in section 3.4 the reel-out is controlled by the ground station. In order to set the right reel-out speed, an optimal tether length is determined. To model this, a Fourier series is used to periodically change the desired tether length over the flight path. Each period is taken from the highest point on the flight path where the shortest distance to the ground station is equal to the initial tether length (no sag). The Fourier series is set up by eq. (4.2) with the coefficients presented in table 4.14.

$$l_t(\theta_c) = l_{\text{init}} + l_{t,1}\cos\left(\theta_c + \theta_{t,1}\right) + l_{t,2}\cos\left(2\left(\theta_c + \theta_{t,2}\right)\right) \tag{4.2}$$

Table 4.14: Fourier coefficients for desired tether length.

Parameter	Value
l_{init}	616.3 m
$l_{t,1}$	12.31 m
$l_{t,2}$	0.3703 m
$\theta_{t,1}$	1.139 rad
$\theta_{t,2}$	1.139 rad

The other important factor in the power production is the tether force. This force is highly dependent on the lift produced by the aircraft. As lift is a function of angle of attack, a desired angle of attack fed into the pitch (elevator) controller. The angle of attack is also changed in a periodic way like the tether length. The Fourier series, which describes this behaviour, is shown in eq. (4.3) and coefficients in table 4.15.

$$\alpha(\theta_c) = \alpha_0 - \alpha_1 \cos\left(\theta_c + \theta_{0,\alpha 1}\right) - \alpha_2 \cos\left(2\left(\theta_c + \theta_{0,\alpha 2}\right)\right) \tag{4.3}$$

Table 4.15: Fourier coefficients for desired angle of attack.

Parameter	Value
α_0	-2.223
α_1	7.286
α_2	-0.5523
$\theta_{0,\alpha 1}$	-1.711
$\theta_{0,\alpha 2}$	-1.691

Even though the Fourier series representation shows a reasonable performance, it is not assumed that this is the most optimal implementation. More coefficients could be assumed or another approach all together. However, this is not researched in this thesis.

4.2.4.3. Generator and tether dimensions

To model the generator and tether, the list presented in table 4.16 is fed into the flight simulation. The generator efficiency, brake down torque and inertia are taken from the S95-2.1MW turbine generator [94]. The availability and technical detail of this report are the main reason this multi-megawatt generator is used. The tether diameter is determined with the buckling force to let the tether break after the wing would exceed the buckling load. Here a safety factor of 1.5 is applied to the buckling force to make sure the tether would not brake in real life applications. In case of a fully coupled structure - flight dynamics optimisation, the tether diameter would be different for each simulation. A material suitable for the tether is found to be High Performance PolyEthylene (HPPE). Such a material is used by KitePower for example [95, 96]. The unit damping and unit stiffness values are calculated by eqs. (3.24) and (3.25), respectively. The number of tether particles is set to five and the tether drag coefficient is taken from a cylindrical shape. The gearbox of the S95-2.1MW turbine presented in [94] has a gearbox ratio of 1:98.8, however, a winch is used in this system as opposed to a rotor. The gearbox ratio is therefore determined by comparing the reel-out speed of the tether with the operating range of the generator. Taking the maximum reel-out speed seen throughout the first initial simulations ($4.5\ \mathrm{m\,s^{-1}}$), the winch diameter and a generator operating speed of 1500 rpm the gearbox ratio can be determined by $n_g = \left(\frac{1500 \cdot 2\pi \cdot 2}{60 \cdot 4.5 \cdot 0.8}\right)$. Even though the reel-out speed is not constant throughout the optimisation, the final result in figure 4.18 shows a close resemblance to this speed. For the purpose of an accurate ground station, a generator - and thus a gearbox ratio - should be thought through to a higher extend. For wind turbines the industry is moving towards direct-drive permanent magnet synchronous generators [97]. These generators are more reliable, but currently massive systems. In the future this might be necessary to consider in modelling as well.

Table 4.16: Ground station and tether characteristics.

Parameter		Value
Ground station:		
Efficiency	[-]	96.8
Brake down torque	[N m]	1000000
Inertia	[kg m^2]	195
Winch diameter	[m]	0.8
Gearbox ratio	[-]	87.2665
Tether:		
Young's modulus	[Pa]	8.9×10^{10}
Tensile strength	[Pa]	1.15×10^{9}
Diameter	[m]	0.0558
k_0	[N]	2.1357×10^{6}
c_0	[N s]	1.0679×10^{4}
Length density	[kg/m$_{100}$]	276.7381
# tether particles	[-]	5
$C_{D,t}$	[-]	1.0

4.3. AWE Reference System performance

The performance of an Airborne Wind Energy System is mainly expressed in power production. This first section shows the behaviour of the system in general and concludes with the power production over a full cycle. A full power cycle is equivalent to 24.4 s flight period. Each of the performance graphs are at a reference wind velocity of 10 m s^{-1} unless stated otherwise.

The aircraft has a different velocity over the power cycle as expected from changing orientation compared to the gravity vector. Figures 4.15 and 4.16 show how the velocity changes over a cycle. The 0 and 2π circumferential angles are taken at the lowest altitude of the flight path. As the aircraft speeds up in downwards flight, the highest velocities are expected in this region. This is also visible in both figures.

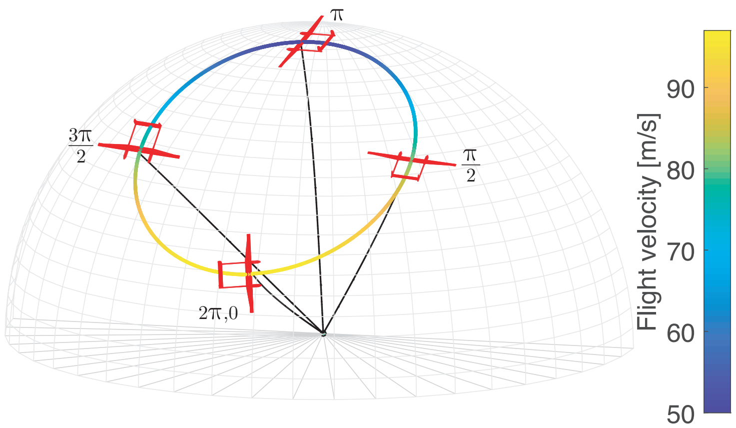

Figure 4.15: Flight velocities during a full power cycle (coloured line) and the aircraft with connected tether at four positions in the cycle.

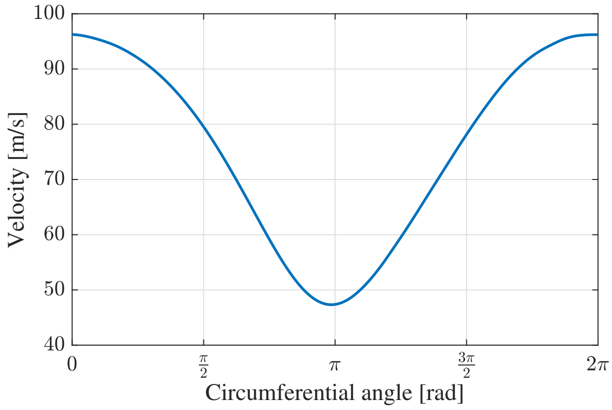

Figure 4.16: Detailed flight velocities during a full power cycle.

Figure 4.17 shows the actual and desired tether length. The controller manages to follow the desired tether length quite well. However, looking very closely it can be noted that the actual tether length has a slight delay in behaviour causing the tether length to be off in the order of a few tens of centimetres. Considering the difference with the order of magnitude in the tether length itself, the controller is considered to perform very well.

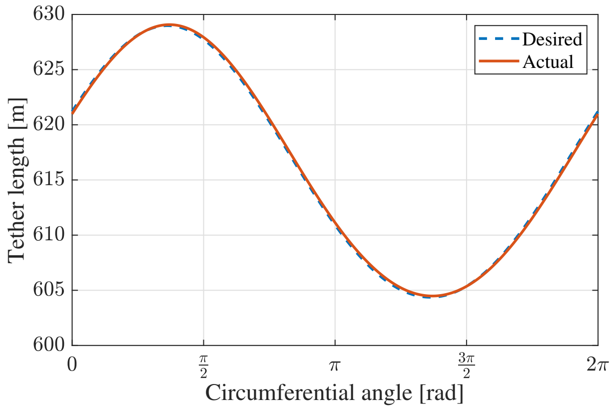

Figure 4.17: Desired and actual tether length over a power cycle.

Figure 4.18 shows the actual and desired reel-out (and reel-in) speed. The controller has difficulties reaching the desired reel-out speed. Continuing controller tuning or a change in controller approach could potentially increase the controller accuracy and may even increase the system performance overall. However, this is not performed in this research project.

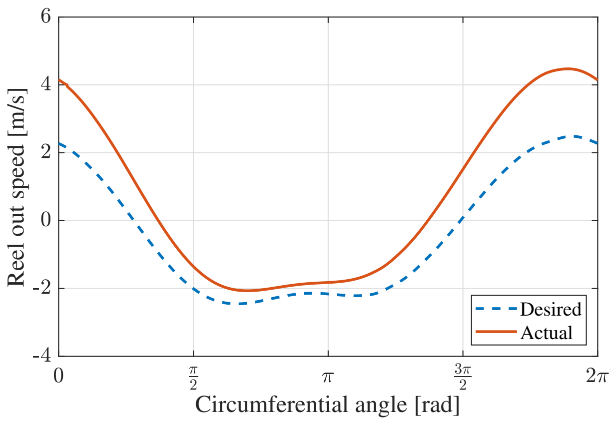

Figure 4.18: Desired and actual reel out speed of the tether over a power cycle (a negative reel out is equivalent to reel in).

One of the main contributor to the power output is the tether force. As this force is determined by the lift force of the aircraft, it is expected that the lift and the tether force follow the same behaviour over a cycle. However, the lift force is not exactly equal to the tether force as can be seen in figures 4.19 and 4.20. This is mainly caused by the attitude of the aircraft. The roll and pitch manoeuvrers of the aircraft cause the lift vector to be misaligned with the tether force. Another influence might be the inertias used to establish a dynamic equilibrium. It can be observed the tether force stays below the allowed buckling load of the wing with some room left (Buckling load is 1.875×10^6 N, safety factor of 1.5 is applied). This is mainly because the result from the optimisation is not power optimal. As mentioned before, four controller gains are kept constant still and the optimiser gets punished when flying too far of the flight path. For the sake of this reference model it is found more useful to have an aircraft follow a desired flight path rather than trying to optimise a flight path, which is out of the scope of this thesis. In order to do this, other strategies of flying a power cycle need to be considered then as well. In figure 4.19 it can also be noted that there is a small sag in the tether which reduces the tension. This can be explained by the fact that the tether length controller is slightly delayed and the reel-out speed is off as well.

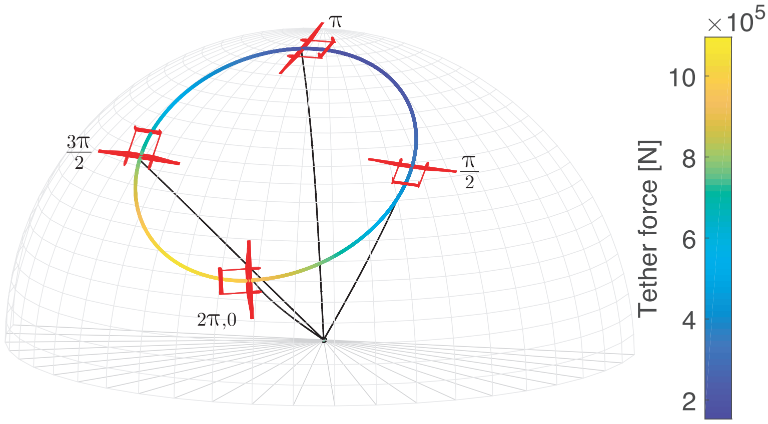

Figure 4.19: Tether forces during a full power cycle (coloured line) and the aircraft with connected tether at four positions in the cycle.

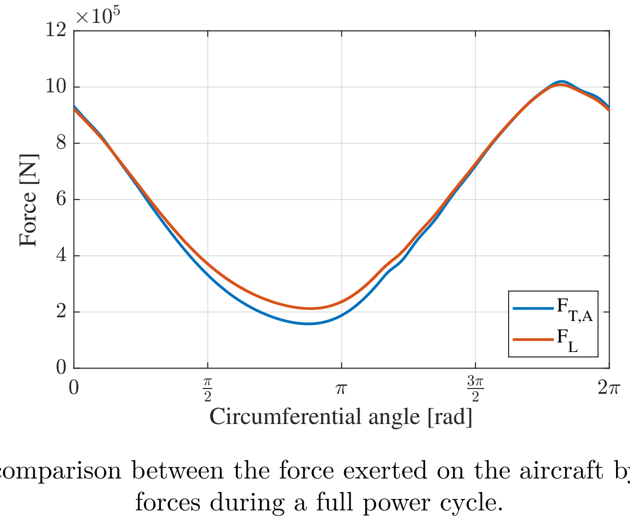

Figure 4.20: Detailed comparison between the force exerted on the aircraft by the tether and the lift forces during a full power cycle.

Figure 4.21 shows the deformation of the wing on two extremes in the power cycle, namely the highest and lowest velocity. The fidelity of the fluid-structure interaction model can be well observed. As expected, the wing deforms more at higher velocities than at low velocities. At $50.4 \mathrm{m\,s^{-1}}$ the wing only deforms approximately 10 cm compared to 50 cm at maximum deflection. Figure 4.22 shows the wing tip displacement of both left and right wing over a power cycle. The two wings do not deform similarly close to the lower end of the flight path. At this stage during the power cycle, the velocity and roll angle are the highest causing a significant non-symmetric wing loading.

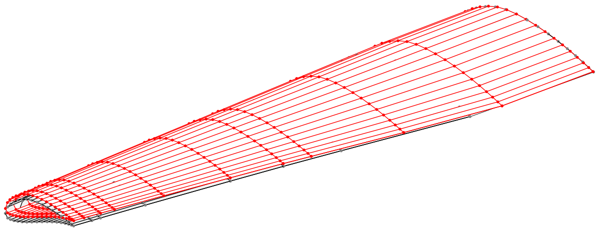

(a) V=50.4m s^{-1}.

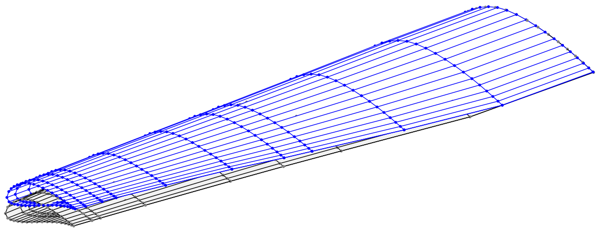

(b) V=96.3m s^{-1}.

Figure 4.21: Wing deformations at the cycle stage with lowest velocity and highest velocity compared to the undeformed wing (grey).

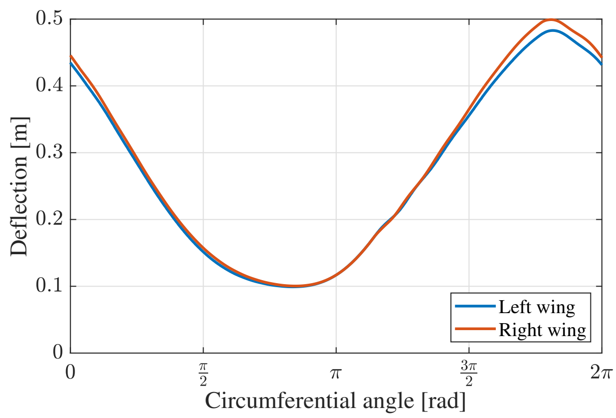

Figure 4.22: Detailed wing tip displacement during a full power cycle.

Figures 4.23 and 4.24 illustrate the error of the flown trajectory compared to the desired flight path. The maximum distance from the desired flight path is almost 21 m. The average is only 11.4 m which is less than 5% of the circle radius. This is considered close enough to the desired flight path. It can be noted in figure 4.23 that the aircraft does not reach a zero distance even though it might look like this in figure 4.24. This is due to the depth which cannot be seen properly in the three dimensional view. The small scale oscillations are occurring due to one big factor. This is the way the distance to the flight path is calculated. This is done by taking the closest point on the desired flight path and calculating the shortest distance to this point. Using more points on the desired flight path will decrease the oscillations. However, for the current research a more accurate flight path error is irrelevant.

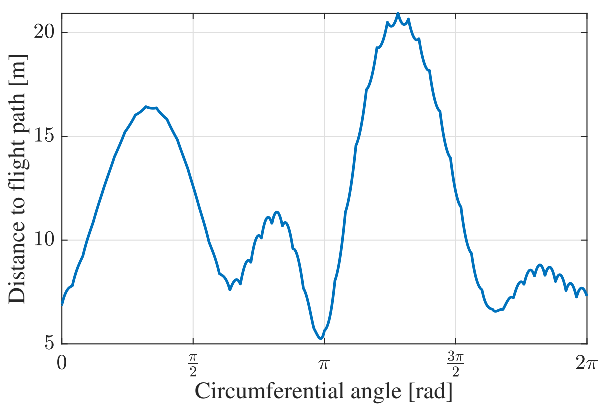

Figure 4.23: Closest distance to the desired flight path during a full power cycle.

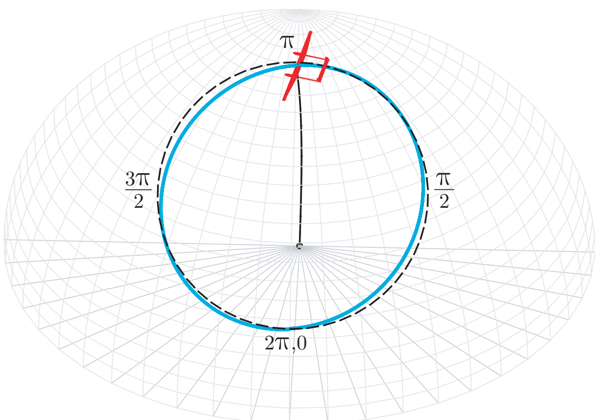

Figure 4.24: Desired (dashed) and actual(blue) flight path during a full power cycle.

Figure 4.25 shows the aileron deflection of one aileron in the power cycle. The other aileron would be equal but opposite sign as the ailerons are deflected differentially. It can be observed that in the current wind and flight conditions only small aileron angle deflections are necessary to achieve the desired roll angles. However, this does not have to mean the ailerons are sized too big. Other phases of the operation cycle, like take-off and landing and the real life trajectory initialisation are not taken into account. Also flying more optimal flight paths and different wind speeds might require bigger aileron deflections.

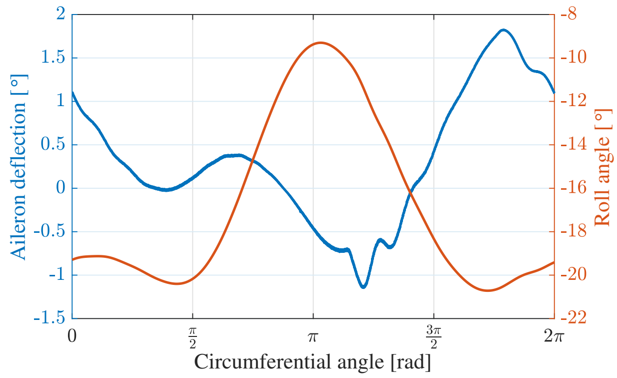

Figure 4.25: Aileron deflections and roll angle over a power cycle.

Combining the behaviour described with the figures above, the performance of this system can be expressed in power output. Figure 4.26 shows a visualisation of the power over its flight path. Figure 4.27 shows the values in more detail. The first thing that can be observed is the direct relation between power output and tether force. The point on the flight path where the tether force reaches its maximum is approximately the same point where the power reaches its maximum. Power is consumed when the tether is retracted. The average power over this cycle is 610.6 kW which is only 14.4% of the peak power (4.23 MW). This means that even though this system can be called a multi-megawatt airborne wind energy system, the actual production per cycle is less than 1MW. Further optimising controller inputs and allowing the aircraft to deviate further from its desired flight path can be solution to improve the power productions. Choosing a complete different flight path and using a better, more accurate controller will most certainly increase the average power production over the megawatt threshold.

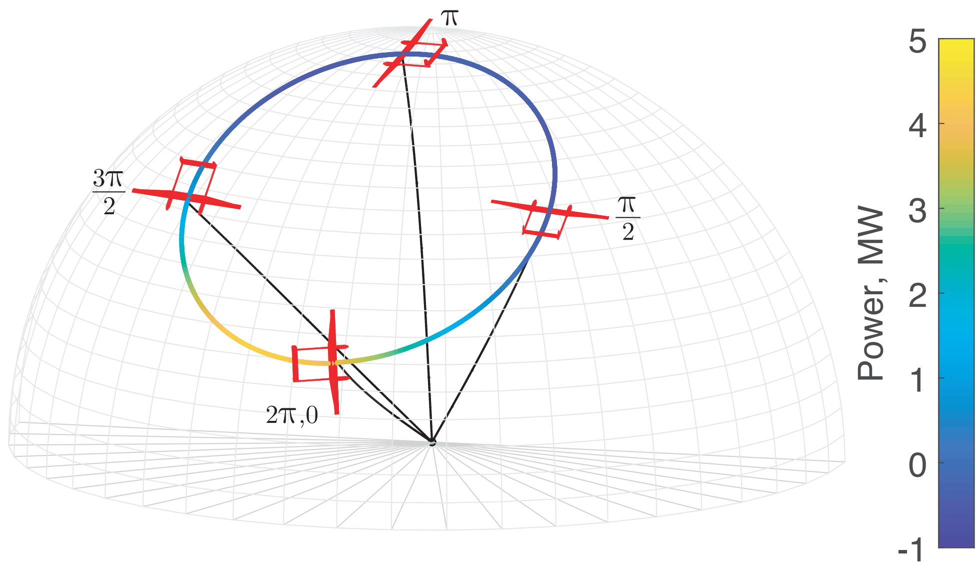

Figure 4.26: Power production during a full power cycle (coloured line) and the aircraft with connected tether at four positions in the cycle.

Figure 4.30 shows the possibility to achieve an average power in the megawatt scale. This is possible as the constraint for the flight path error is loosened, which is visible in figure 4.28 where a maximum error of 88.5 m can be observed. Figure 4.29 displays the tether- and lift force which stay below the

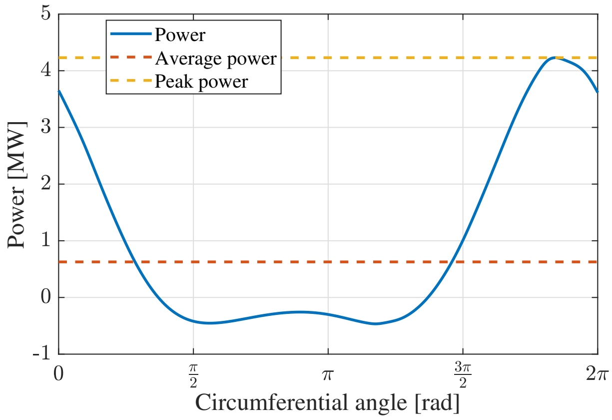

Figure 4.27: Detailed power production during a full cycle.

buckling constraint as requested.

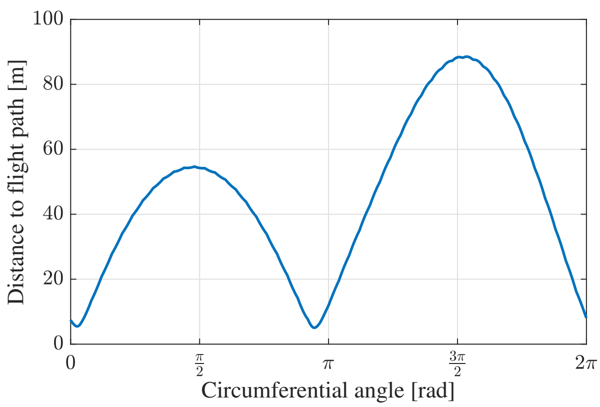

Figure 4.28: Improved power: closest distance to the desired flight path during a full power cycle.

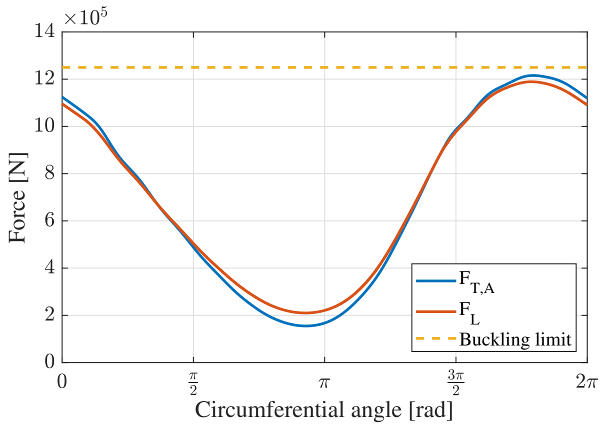

Figure 4.29: Improved power: detailed comparison between the force exerted on the aircraft by the tether and the lift forces during a full power cycle.

Finally, to show the capabilities of this system at different wind speeds than just 10 m s^{-1}, the objective function is adapted to the function shown in appendix B.3. The power is more optimal at lower wind speeds, forcing the optimiser to find parameter values at a lower wind speed. This result is shown in figure 4.31. Here part of a full power curve can be seen. Many of the results for a specific wind speed can be improved still by investing more time. Due to time constraint the presented result is decided to be a representation of what could potentially be the power performance. Also the theoretical cubic relation between power and wind speed fitted to the data is shown. Currently the results follow more a quadratic relation than cubic, but more time and/or more computational power can change the graph significantly. This is mainly demonstrated by the individual optimisation of a wind speed equal to 10. Here the produced power is significantly increased when only one wind speed is considered.

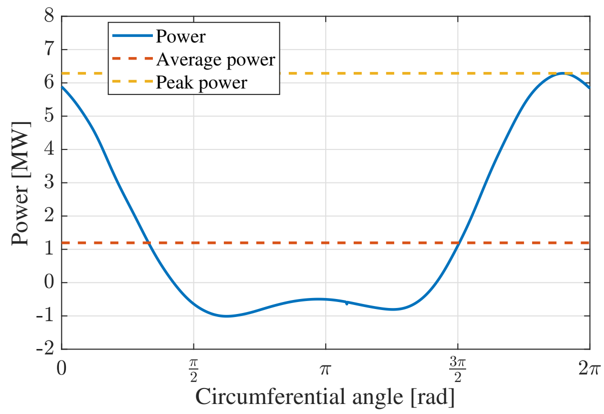

Figure 4.30: Detailed improved power production during a full cycle, average power = 1.1957 MW.

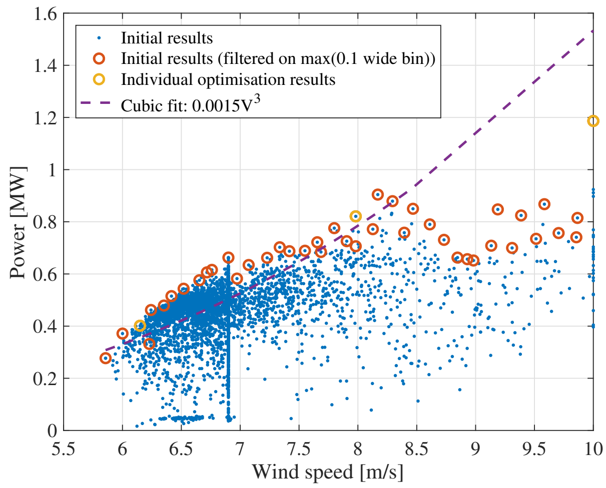

Figure 4.31: Power production for different wind speeds in the operational envelope.

5
Conclusion and recommendations

This chapter draws a conclusion given the results presented in chapter 4. Section 5.2 elaborates on recommendations for further research and necessary changes that need to be made to obtain a better performing Airborne Wind Energy System.

5.1. Conclusion

One issue with the renewable energy harvested by conventional wind turbines is that wind farms can cause saturation of windy areas. However, an Airborne Wind Energy can harvest larger and more persistent wind speeds at higher altitudes at a fraction of the cost of a conventional wind turbine.

Taking into account no commercial utility-scale product has been released to the market yet and looking at the trend in conventional wind energy industry, there is a big need for a public reference system which can be used by universities and companies to compare their research and enhance the development of airborne wind energy systems. Over the years the NREL 5 MW reference wind turbine has been accelerating further developments and widely used by universities and companies all over the world.

As mentioned before, a publicly available airborne wind energy reference model is not available yet. Even though a lot will change in the next decades, this research will be of key importance to stimulate more research and a collaboration within the Airborne Wind Energy research society. A rigid wing aircraft is chosen to be best suited for this reference as more and more companies are shifting their focus to this particular design. Mainly due to the durability issues coming with fabric wings.

This thesis presents the detailed design of the first publicly available Multi Megawatt Airborne Wind Energy Reference System and its parametrisation. An optimisation framework and full dynamic system simulation is presented as a method to evaluate high fidelity system performance at an early design stage and with relatively low computational effort. The optimisations performed in this work were performed practically locally on a single computer. This makes this method very accessible to anyone without the availability of a super computer or huge server access.

The structural design of the aircraft, the main wing in particular, show the ability to sustain high wing loading. Currently a wing loading of 29.5 can be sustained, but making the Finite Element Model of the wing more complex with a higher number of input parameters could potentially lower the weight of the wing of reducing the composite layup where needed the least. The parametrisation performed is therefore found a useful initial proposal.

The system is shown to perform well in the megawatt scale. However the current found controller strategy, gains and flight path combination does not allow for an average production in the megawatt scale yet. Allowing the aircraft to deviate more than 5% of the flight path radius from the desired trajectory, does produce an average power of more than 1 MW over one full cycle. Investing more time and further research would most likely produce a system with much better performance than described now. The current results do show the full potential of a 150 m² wing which is already able to generate multiple megawatts of power. Further decreasing the weight of the composite wing will increase the load factor and increase the force on the tether, allowing for bigger power production.

Even though a lot of improvements can be made - some of them discussed in section 5.2 - the system provided by this thesis does define a useful reference system. This system can be used to scale performance and carry out several different optimisations, ensuring further development of the airborne wind energy sector. It is expected to have initiated a foundation of reference systems in airborne wind energy; that other researchers will contribute to this benchmark network as well; and more detailed designs and results will be published.

5.2. Recommendations and outlook

Even though a big step is made towards a well performing multi megawatt airborne wind energy reference system, the system still requires a lot of further research and evaluation whether design choices made here should have been made differently to obtain better performance. Many considerations have not been taken into account as there is still little known about what choices are better than others. For example, the main design constraint where this thesis is based on, is the assumption of using a ground-generated rigid wing AWE system as reference. This choice is solely based on the fact that many organisations are switching towards this system for its benefit over a flexible kite in terms of durability and the benefit of not having to lose expensive generators from crashing a test aircraft. However, it is not proven that one system is better over the other and this trend might shift in the future. Therefore, it is stated explicitly that this thesis tries to initiate a publicly available benchmarking industry rather than proposing the best design for a reference system. Flying a circular trajectory was able to produce power but has a lot of potential for improvement. Several different studies are already performed on flight path optimisation, which was out of the scope of this thesis. The research done on flight path optimisation shows that flying helical or figure of eight flight path trajectories might significantly improve power production.

The current wings are depended on a reverse engineered airfoil shape. This is far from an optimal way of designing an airfoil. The power output of an AWES is highly dependent on the aircraft lift but needs to be able to withstand high wing loadings. Thorough research in an optimal airfoil shape for tethered flight might influence the performance significantly. This includes adding flaps and/or slats to increase lift capabilities which are now limited to a single airfoil analysis. Including high lift devices require an adaptation of the current aerodynamic model.

The Finite Element Analysis is performed by a linear analysis. Further research should show if this assumption still holds and produces accurate results at large scale AWE wings. Also the used 3D panel method relies on linear assumptions, which is based on the comparison of a small aircraft linear and non-linear analyses. The results here showed accuracy of the linear approximation within required bounds. However, time constraints did not allow for a similar analysis of the large-scale aircraft and this should be considered in future studies.

For the computational efficiency of the FSI, a steady wake is shed behind the wing. Including unsteady aerodynamic effects into the simulations lowers the computational efficiency by several orders. However, detailed analyses of the system power capabilities require a higher fidelity aerodynamic analysis and in wind farm configurations an accurate wake might be necessary to evaluate the power production of a wind farm. The current aerodynamic model is mostly chosen because of the availability. In chapter 2 other possibilities are given, and for each case it should be evaluated what is best. The original model was designed for camber morphing wings. However, the aircraft designed in this thesis has a constant cambered airfoil. It could be considered using a non-linear extended lifting line method instead, which increases the computational efficiency. It should be researched if this is accurate enough. Pre-CFD calculations could be performed as well on singular or multi-body airfoil profiles. The current 3D panel method is incapable of taking into account a slotted flap. Having section-wise pre-computed CFD data combined with a non-linear lifting line method could provide more accurate power optimisations for a single planform (as the CFD data is only valid for one shape).

The current implementation of the aileron mechanism is not very suitable for physical evaluations. A better more realistic implementation can allow for the evaluation of aileron effectiveness and aileron flutter which are phenomena that can greatly influence performance. Control reversal can have fatal consequences for the aircraft.

The performance of this system is expressed here in terms of flying a desired trajectory and the accompanied power production. However, this is not the only way of measuring performance and feasibility. Another point of view, which might be more important when working towards a commercial system, is the cost and, consequently, the levelised cost of energy. Commercial companies will probably have this as their main optimisation goal. For a reference system it might be interesting to compare a cost optimisation with the power optimisation performed here. Many different methods of estimating costs are available, some more detailed than others. An initial cost estimation can be based on a bottom-up approach for the composite parts where the number of layers and orientation is known in detail. Other system aspects where less details are known yet could be modelled with a parametric approach. Coupling a cost model with the framework illustrated throughout this thesis could estimate and eventually optimise the system for cost of energy. However, a cost model was found too time consuming to proceed with during this initial design, but it definitely has potential for obtaining designs which can better represent commercial products.

Bibliography

[1] Wrigley, E. A., "Energy and the english industrial revolution," *Phil. Trans. R. Soc. A*, vol. 371, no. 1986, p. 20110568, 2013.

[2] Jonkman, J., Butterfield, S., Musial, W., and Scott, G., "Definition of a 5-mw reference wind turbine for offshore system development," *National Renewable Energy Laboratory, Golden, CO, Technical Report No. NREL/TP-500-38060*, 2009.

[3] Bak, C., Zahle, F., Bitsche, R., Kim, T., Yde, A., Henriksen, L. C., Hansen, M. H., Blasques, J. P. A. A., Gaunaa, M., and Natarajan, A., "The dtu 10-mw reference wind turbine," in *Danish Wind Power Research 2013*, 2013.

[4] Peeringa, J., Brood, R., Ceyhan, O., Engels, W., and De Winkel, G., "Upwind 20mw wind turbine pre-design," *ECN, Paper No. ECN-E–11-017*, 2011.

[5] Loyd, M. L., "Crosswind kite power (for large-scale wind power production)," *Journal of energy*, vol. 4, no. 3, pp. 106–111, 1980.

[6] Ampyx Power, "How does it work?" [Online]. Available: https://www.ampyxpower.com/technology

[7] ——, "The sea-air-farm project: Demonstrating the potential of far offshore floating airborne wind farms," Public Summary, 2018.

[8] Fasel, U., Keidel, D., Molinari, G., and Ermanni, P., "Aeroservoelastic optimization of morphing airborne wind energy wings," in *AIAA Scitech 2019 Forum*, 2019, p. 1217.

[9] Ahrens, U., Diehl, M., and Schmehl, R., *Airborne wind energy.* Springer Science & Business Media, 2013.

[10] Cherubini, A., Papini, A., Vertechy, R., and Fontana, M., "Airborne wind energy systems: A review of the technologies," *Renewable and Sustainable Energy Reviews*, vol. 51, pp. 1461–1476, 2015.

[11] Kruijff, M. and Ruiterkamp, R., "A roadmap towards airborne wind energy in the utility sector," in *Airborne Wind Energy.* Springer, 2018, pp. 643–662.

[12] Vander Lind, D., "Analysis and flight test validation of high performance airbornewind turbines," in *Airborne Wind Energy.* Springer, 2013, pp. 473–490.

[13] Williams, P., Lansdorp, B., and Ockesl, W., "Optimal crosswind towing and power generation with tethered kites," *Journal of guidance, control, and dynamics*, vol. 31, no. 1, pp. 81–93, 2008.

[14] Canale, M., Fagiano, L., and Milanese, M., "Kitegen: A revolution in wind energy generation," *Energy*, vol. 34, no. 3, pp. 355–361, 2009.

[15] Erhard, M. and Strauch, H., "Flight control of tethered kites in autonomous pumping cycles for airborne wind energy," *Control Engineering Practice*, vol. 40, pp. 13–26, 2015.

[16] Cherubini, A., "Kite dynamics and wind energy harvesting," Laurea Magistrale, Politecnico di Milano, 2012.

[17] Lütsch, G., "Airborne wind energy network hwn500–shouldering r&d in cooperations," in *Abstract submitted to the airborne wind energy conference. TU Delft*, 2015.

[18] Dunker, S., "Ram-air wing design considerations for airborne wind energy," in *Airborne Wind Energy.* Springer, 2013, pp. 517–546.

[19] Ippolito, M., "Infrastructure for driving and assisting take-off of airfoils for tropospheric aeolian generator," May 2009, pCT Patent WO2009147692.

[20] ——, "Tether for tropospheric aeolian generator," Jan. 2010, pCT Patent WO2010084520.

[21] Bormann, A., Gebhardt, C., Hauke, C., and Skutnik, S., "Global economy of airborne wind energy and our path towards a market-ready technology," in *Abstract submitted to the airborne wind energy conference. TU Delft*, 2015.

[22] Ruiterkamp, R. and Sieberling, S., "Description and preliminary test results of a six degrees of freedom rigid wing pumping system," in *Airborne wind energy.* Springer, 2013, pp. 443–458.

[23] Waszak, M. R. and Schmidt, D. K., "Flight dynamics of aeroelastic vehicles," *Journal of Aircraft*, vol. 25, no. 6, pp. 563–571, 1988.

[24] Buttrill, C., Arbuckle, D., and Zeiler, T., "Nonlinear simulation of a flexible aircraft in maneuvering flight," in *Flight Simulation Technologies Conference*, 1987, p. 2501.

[25] Neill, D., Johnson, E., and Canfield, R., "Astros-a multidisciplinary automated structural design tool," *Journal of Aircraft*, vol. 27, no. 12, pp. 1021–1027, 1990.

[26] Drela, M., "Method for simultaneous wing aerodynamic and structural load prediction," *Journal of aircraft*, vol. 27, no. 8, pp. 692–699, 1990.

[27] ——, "Integrated simulation model for preliminary aerodynamic, structural, and control-law design of aircraft," in *40th Structures, Structural Dynamics, and Materials Conference and Exhibit*, 1999, p. 1394.

[28] Meirovitch, L. and Stemple, T., "Hybrid equations of motion for flexible multibody systems using quasicoordinates," *Journal of Guidance, Control, and Dynamics*, vol. 18, no. 4, pp. 678–688, 1995.

[29] Meirovitch, L. and Tuzcu, I., "Multidisciplinary approach to the modeling of flexible aircraft," in *International Forum on Aeroelasticity and Structural Dynamics, Madrid, Spain, June*, 2001, pp. 5–7.

[30] ——, "Integrated approach to flight dynamics and aeroservoelasticity of whole flexible aircraft-part i: System modeling," in *AIAA Guidance, Navigation, and Control Conference and Exhibit*, 2002, p. 4747.

[31] Waszak, M. R., Meirovitch, L., and Tuzcu, I., "Integrated approach to the dynamics and control of maneuvering flexible aircraft," 2003.

[32] Meirovitch, L. and Tuzcu, I., "Unified theory for the dynamics and control of maneuvering flexible aircraft," *AIAA journal*, vol. 42, no. 4, pp. 714–727, 2004.

[33] Meirovitch, L., "Hybrid state equations of motion for flexible bodies in terms of quasi-coordinates," *Journal of Guidance, Control, and Dynamics*, vol. 14, no. 5, pp. 1008–1013, 1991.

[34] ——, "Derivation of equations for flexible multibody systems in terms of quasi-coordinates from the extended hamilton's principle," *Shock and Vibration*, vol. 1, no. 2, pp. 107–119, 1993.

[35] ——, "A unified theory for the flight dynamics and aeroelasticity of whole aircraft," in *Proceedings of the Eleventh Symposium on Structural Dynamics and Control*, 1997, pp. 461–468.

[36] Patil, M. J., Hodges, D. H., and S. Cesnik, C. E., "Nonlinear aeroelastic analysis of complete aircraft in subsonic flow," *Journal of Aircraft*, vol. 37, no. 5, pp. 753–760, 2000.

[37] Williams, P., Lansdorp, B., Ruiterkamp, R., and Ockels, W., "Modeling, simulation, and testing of surf kites for power generation," in *AIAA Modeling and Simulation Technologies Conference and Exhibit*, vol. 6693, 2008.

[38] Terink, E., Breukels, J., Schmehl, R., and Ockels, W., "Flight dynamics and stability of a tethered inflatable kiteplane," *Journal of Aircraft*, vol. 48, no. 2, pp. 503–513, 2011.

[39] Dadd, G. M., Hudson, D. A., and Shenoi, R., "Determination of kite forces using three-dimensional flight trajectories for ship propulsion," *Renewable Energy*, vol. 36, no. 10, pp. 2667–2678, 2011.

[40] Brown, E. L., "Integrated strain actuation in aircraft with highly flexible composite wings," Ph.D. dissertation, Massachusetts Institute of Technology, 2003.

[41] Shearer, C. M., "Coupled nonlinear flight dynamics, aeroelasticity, and control of very flexible aircraft," Ph.D. dissertation, Massachusetts Institute of Technology, 2006.

[42] Su, W. and Cesnik, C. E., "Strain-based geometrically nonlinear beam formulation for modeling very flexible aircraft," *International Journal of Solids and Structures*, vol. 48, no. 16-17, pp. 2349–2360, 2011.

[43] Su, W., "Coupled nonlinear aeroelasticity and flight dynamics of fully flexible aircraft." Ph.D. dissertation, Massachusetts Institute of Technology, 2008.

[44] Breukels, J., "An engineering methodology for kite design," Ph.D. dissertation, Delft University of Technology, 2011.

[45] Bosch, A., Schmehl, R., Tiso, P., and Rixen, D., "Dynamic nonlinear aeroelastic model of a kite for power generation," *Journal of Guidance, Control, and Dynamics*, vol. 37, no. 5, pp. 1426–1436, 2014.

[46] Fasel, U., Keidel, D., Molinari, G., and Ermanni, P., "Aerostructural optimization of a morphing wing for airborne wind energy applications," *Smart Materials and Structures*, vol. 26, no. 9, p. 095043, 2017.

[47] Wijnja, J., Schmehl, R., De Breuker, R., Jensen, K., and Vander Lind, D., "Aeroelastic analysis of a large airborne wind turbine," *Journal of Guidance, Control, and Dynamics*, vol. 41, no. 11, pp. 2374–2385, 2018.

[48] Dussart, G., Portapas, V., Pontillo, A., and Lone, M., "Flight dynamic modelling and simulation of large flexible aircraft," *Flight Physics-Models, Techniques and Technologies*, 2018.

[49] Fasel, U., Tiso, P., Keidel, D., Molinari, G., and Ermanni, P., "Reduced-order dynamic model of a morphing airborne wind energy aircraft," *AIAA Journal*, pp. 1–13, 2019.

[50] Filkovic, D., "Graduate work: 3d panel method," *Faculty of Mechanical Engineering and Naval Architecture, University of Zagreb, Croatia*, 2008.

[51] Horn, G., Gros, S., and Diehl, M., "Numerical trajectory optimization for airborne wind energy systems described by high fidelity aircraft models," in *Airborne wind energy.* Springer, 2013, pp. 205–218.

[52] Bak, C., Zahle, F., Bitsche, R., Kim, T., Yde, A., L.C. Henriksen, P.B. Andersen, Natarajan, A., and M.H. Hansen, "Design and performance of a 10 mw wind turbine," *J. Wind Energy*, 2013.

[53] Goldstein, L., "Scalability of airborne wind energy systems," 2014, preprint on webpage at http://www.energykitesystems.net/LeoGoldstein/.

[54] Diehl, M., "Airborne wind energy: Basic concepts and physical foundations," in *Airborne wind energy.* Springer, 2013, pp. 3–22.

[55] Argatov, I., Rautakorpi, P., and Silvennoinen, R., "Estimation of the mechanical energy output of the kite wind generator," *Renewable Energy*, vol. 34, no. 6, pp. 1525–1532, 2009.

[56] Molinari, G., Quack, M., Dmitriev, V., Morari, M., Jenny, P., and Ermanni, P., "Aero-structural optimization of morphing airfoils for adaptive wings," *Journal of Intelligent Material Systems and Structures*, vol. 22, no. 10, pp. 1075–1089, 2011.

[57] Nastran, M., "Linear static analysis user's guide," *MSC Software Corporation*, 2012.

[58] Arena, M., Palumbo, R., Pecora, R., Amoroso, F., Amendola, G., and Dimino, I., "Flutter clearance investigation of camber-morphing aileron tailored for a regional aircraft," *Journal of Aerospace Engineering*, vol. 32, no. 2, 2018.

[59] Previtali, F., Arrieta, A. F., and Ermanni, P., "Performance of a three-dimensional morphing wing and comparison with a conventional wing," *AIAA journal*, vol. 52, no. 10, pp. 2101–2113, 2014.

[60] Rea, F., Pecora, R., Amoroso, F., Arena, M., Noviello, M. C., and Amendola, G., "Aeroelastic stability analysis of a wind tunnel wing model equipped with a true scale morphing aileron," *International Journal of Mechanical Engineering and Robotics Research*, vol. 6, no. 6, pp. 440–450, 2017.

[61] Besselink, B., Tabak, U., Lutowska, A., Van de Wouw, N., Nijmeijer, H., Rixen, D. J., Hochstenbach, M., and Schilders, W., "A comparison of model reduction techniques from structural dynamics, numerical mathematics and systems and control," *Journal of Sound and Vibration*, vol. 332, no. 19, pp. 4403–4422, 2013.

[62] Newmark, N. M. *et al.*, "A method of computation for structural dynamics." American Society of Civil Engineers, 1959.

[63] Katz, J. and Plotkin, A., *Low-speed aerodynamics.* Cambridge university press, 2001, vol. 13.

[64] John, V., "The navier–stokes equations as model for incompressible flows," in *Finite Element Methods for Incompressible Flow Problems.* Springer, 2016, pp. 7–24.

[65] Abbott, I. H. and Von Doenhoff, A. E., *Theory of wing sections, including a summary of airfoil data.* Courier Corporation, 1959.

[66] Van Rooij, R., "Modification of the boundary layer calculation in rfoil for improved airfoil stall prediction," *Report IW-96087R TU-Delft, the Netherlands*, 1996.

[67] Drela, M. and Giles, M. B., "Viscous-inviscid analysis of transonic and low reynolds number airfoils," *AIAA journal*, vol. 25, no. 10, pp. 1347–1355, 1987.

[68] Miller, K. S., "On the inverse of the sum of matrices," *Mathematics magazine*, vol. 54, no. 2, pp. 67–72, 1981.

[69] Schwochow, J., "Robust flutter analysis using interval modal analysis and continuation method," in *International Forum on Aeroelasticity and Structural Dynamics, June*, 2009, pp. 21–25.

[70] Baayen, J., "Modeling a kite on a variable length flexible tether," Master's thesis, Delft University of Technology, 2011.

[71] Fechner, U., van der Vlugt, R., Schreuder, E., and Schmehl, R., "Dynamic model of a pumping kite power system," *Renewable Energy*, vol. 83, pp. 705–716, 2015.

[72] Jenkins, N., Burton, A., Sharpe, D., and Bossanyi, E., *Wind Energy Handbook*. United Kingdom: John Wiley & Sons Ltd, 2001.

[73] Galliard, C., Verling, S., Stastny, T., and Siegwart, R., "Spherical guidance and control for an airborne wind energy system," Bachelor's Thesis, ETH Zürich, 2017.

[74] Fagiano, L., Nguyen-Van, E., Rager, F., Schnez, S., and Ohler, C., "Autonomous takeoff and flight of a tethered aircraft for airborne wind energy," *IEEE Transactions on Control Systems Technology*, vol. 26, no. 1, pp. 151–166, 2017.

[75] Rapp, S., Schmehl, R., Oland, E., Smidt, S., Haas, T., and Meyers, J., "A modular control architecture for airborne wind energy systems," in *AIAA Scitech 2019 Forum*, 2019, p. 1419.

[76] Park, S., Deyst, J., and How, J., "A new nonlinear guidance logic for trajectory tracking," in *AIAA guidance, navigation, and control conference and exhibit*, 2004, p. 4900.

[77] Meier, L., Honegger, D., and Pollefeys, M., "Px4: A node-based multithreaded open source robotics framework for deeply embedded platforms," in *2015 IEEE international conference on robotics and automation (ICRA)*. IEEE, 2015, pp. 6235–6240.

[78] Harder, R. L. and Desmarais, R. N., "Interpolation using surface splines." *Journal of aircraft*, vol. 9, no. 2, pp. 189–191, 1972.

[79] Duchon, J., "Splines minimizing rotation-invariant semi-norms in sobolev spaces," in *Constructive theory of functions of several variables*. Springer, 1977, pp. 85–100.

[80] de Boer, A., Van Zuijlen, A., and Bijl, H., "Review of coupling methods for non-matching meshes," *Computer methods in applied mechanics and engineering*, vol. 196, no. 8, pp. 1515–1525, 2007.

[81] Shepard, D., "A two-dimensional interpolation function for irregularly-spaced data," in *Proceedings of the 1968 23rd ACM national conference*. ACM, 1968, pp. 517–524.

[82] Lonsain, J., "Aeroelastic analysis of a 3d wing structure with a flexible trailing edge," Master's thesis, Delft University of Technology, 2017.

[83] Ashino, R., Nagase, M., and Vaillancourt, R., "Behind and beyond the matlab ode suite," *Computers & Mathematics with Applications*, vol. 40, no. 4-5, pp. 491–512, 2000.

[84] Hansen, N., "The cma evolution strategy: a comparing review," in *Towards a new evolutionary computation*. Springer, 2006, pp. 75–102.

[85] Chaitanya, R., Tarkian, M., and Jouannet, C., "Model based aircraft control system design and simulation," in *International Congress of the Aeronautical Sciences*, 2010.

[86] Wright, J. and Cooper, J., *Introduction to Aircraft Aeroelasticity and Loads*, ser. Aerospace Series (PEP). John Wiley & Sons, 2008. [Online]. Available: https://books.google.ch/books?id=305nZEgRN6IC

[87] Kumar, G. S., Mohan, S., and Rao, R. S., "Design development and cfd simulation of a variable twist wing," *Imperial Journal of Interdisciplinary Research*, vol. 3, no. 5, 2017.

[88] de Oliveira, G., Fechner, U., and Pereira, R., "Multiobjective airfoil design for airborne wind energy." Airborne Wind Energy Conference 2017, 2017.

[89] Venturato, A., "Analisi fluidodinamica del profilo alare clark-y ed ottimizzazione multi-obbiettivo tramite algoritmo genetico," Master's thesis, Università degli studi di Padova, 2013.

[90] Kroon, E., "Airborne wind energy airfoils: Design of pareto-optimal airfoils for rigid wing systems in the field of airborne wind energy," Master's thesis, TU Delft, 2018.

[91] Houska, B. and Diehl, M., "Optimal control of towing kites," in *Proceedings of the 45th IEEE Conference on Decision and Control*. IEEE, 2006, pp. 2693–2697.

[92] Timmer, W. and Rooij, R., "Summary of the delft university wind turbine dedicated airfoils," in *41st aerospace sciences meeting and exhibit*, 2003, p. 352.

[93] Hepperle, M., "Javafoil user's guide," *available at: www.mh-aerotools.de*, 2011.

[94] Malcher, B. and Mueller, J., "Wind turbine generator: S95–2.1mw turbine," SUZLON Energy GmbH, Tech. Rep., 2011.

[95] Kite Power, "System components - tether," 2012. [Online]. Available: http://www.kitepower.eu/technology/3-sytem-components/49-tether

[96] Dyneema, D., "Dyneema high-strength, high-modulus polyethylene fiber, dyneema fact sheet," 2014.

[97] Semken, R. S., Polikarpova, M., Röyttä, P., Alexandrova, J., Pyrhönen, J., Nerg, J., Mikkola, A., and Backman, J., "Direct-drive permanent magnet generators for high-power wind turbines: Benefits and limiting factors," *IET Renewable Power Generation*, vol. 6, no. 1, pp. 1–8, 2012.

A
Airfoil coordinates

In this chapter the coordinates of the reverse engineered airfoil shape used by this AWE reference system are presented. Table A.1 shows the x and y coordinates of the top and bottom surfaces separately.

Table A.1: Mrev-v2$_{\text{HC}}$ airfoil coordinates.

Top

x [-]	y [-]
1.00000000	0.00000000
0.99318636	0.00384055
0.98078831	0.01056468
0.96393595	0.01968723
0.94228080	0.03071542
0.91623289	0.04408441
0.88583437	0.05917438
0.85148163	0.07589195
0.81341903	0.09367029
0.77194139	0.11194797
0.72735574	0.13014479
0.68033749	0.14858512
0.63103128	0.16623903
0.57997670	0.18292629
0.52758333	0.19798687
0.47437022	0.21099673
0.42069030	0.22091853
0.36702840	0.22717270
0.31385022	0.22763426
0.26233213	0.22034307
0.21373018	0.20724739
0.16897255	0.18961307
0.12877692	0.16861102
0.09344809	0.14585443
0.06362092	0.12188317
0.03994981	0.09739776
0.02180493	0.07185635
0.00962997	0.04597539
0.00306368	0.02439695
0.00050507	0.00915441
0.00000000	0.00000000

Bottom

x [-]	y [-]
0.00032367	-0.00824477
0.00270799	-0.02034526
0.01024134	-0.03528545
0.02714704	-0.04686066
0.05091256	-0.05759559
0.08014692	-0.06407570
0.11399344	-0.06854404
0.15184058	-0.07007498
0.19310978	-0.06926661
0.23727857	-0.06668714
0.28386388	-0.06259660
0.33226880	-0.05577961
0.38193737	-0.04762213
0.43238078	-0.03888881
0.48313028	-0.03005569
0.53377634	-0.02163674
0.58378966	-0.01330148
0.63288186	-0.00606993
0.68054025	0.00037743
0.72636492	0.00565135
0.76997269	0.00928447
0.81093157	0.01128163
0.84886244	0.01199818
0.88333526	0.01160495
0.91398201	0.01010101
0.94048472	0.00729950
0.96253802	0.00480714
0.97986286	0.00226079
0.99236601	0.00068512
1.00000000	0.00000000

B
Objective Functions

In this appendix the Matlab objective functions used throughout this thesis are presented. With first, the structural optimisation objective function in appendix B.1. Second, the power optimisation objective function in appendix B.2. Last, the adapted power optimisation objective function with the ability to progress towards a lower wind speed in appendix B.3.

B.1. Structural optimisation

```
function objFOUT = struct_obj_out(simOut)
% Objective function to optimise the load factor taking buvkling and
% flutter into account.

% simOut.fow = Lift / Aircraft weight;
% simOut.mass = Aircraft mass
% simOut.flutter = FlutterSpeed / Flight speed;
% simOut.buckling = Buckling load / Lift

%% calculate objective function

mP = 50;

% flutter penalty
pFlutter = 0;
sfF = 1.5;
if simOut.flutter < sfF
    pFlutter = mP*(1 + sfF-simOut.flutter);
end

% buckling penalty
if isinf(simOut.buckling)
    simOut.buckling = 0.1;
end
pBuckling = 0;
sfB = 1.5;
if simOut.buckling < sfB
    pBuckling = mP*(1 + sfB-simOut.buckling);
end

objF = -simOut.fow + pFlutter + pBuckling;

objFOUT = [-simOut.fow;simOut.mass;pFlutter;pBuckling;objF];
end
```

B.2. Power optimisation

```
function powerOut = runsimParallel3D(simIn, constraintOut, numSims, simIDrun)
% Objective function to obtain a better power output when following a
% prescribed trajectory as close as possible.

% simIn = Simulation input
% constraintOut = Structure containing the buckling load
% numSims = Number of simulations, equal to 1 or population size
% simIDrun = Simulation ID

%% run parallel simulation and extract power

%%%%%%%%%%%%%%%%%%%%%%%%%%%%%%%%%%%%%%%%%%%%%%%%%%%%%%%%%%%%%%%%%%%%%%%%

deltaPower = 0.02;          % 2% -> steady state
deltaPowerT = 2;            % 2s min circle time

nVw = 1;                    %One wind speed per simulation, old implementation;

powerOut = 1e3.*ones(nVw+4,numSims);

timeSimFinish = zeros(nVw,numSims);

lsimIDrun = length(simIDrun);
if lsimIDrun == 1
    clear(func2str(@checkSteadyState2))
    clear(func2str(@switchSolver3))
    clear(func2str(@deltaAERO))
    clear(func2str(@checkSteadyState_FPerror))
    clear(func2str(@plot_trajectory_dylan))

    % Run the simulation
```

```
    simOut = sim(simIn(1),'UseFastRestart',true,'SetupFcn',...
        @() clearPersistentParSim(),'CleanupFcn',@() clearPersistentParSim());

    for idx = 1:nVw            % idx=1
        try                    % Extract the time where the simulation finished
            timeSimFinish(idx,1) = max(simOut(1,idx).simoutPowerConstraint.time);
        catch
            timeSimFinish(idx,1) = 0;
        end

        try
            powerOutN = simOut(1,idx).simoutPower.signals.values(1:100);
            powerOutN(powerOutN == 0) = [];
            powerOutT = simOut(1,idx).simoutPower.signals.values(101:200);
            powerOutT(powerOutT == 0) = [];
        catch
            powerOutN = [];
            powerOutT = [];
        end
        if length(powerOutN) > 1
            if powerOutT(1) - powerOutT(2) < deltaPowerT
                powerOut(idx,simIDrun) = 0;
            elseif abs((powerOutN(1)-powerOutN(2))/powerOutN(1)) > deltaPower
                powerOut(idx,simIDrun) = -powerOutN(1)*0.1;
            else
                powerOut(idx,simIDrun) = -powerOutN(1);
            end
            if any(simOut(1,idx).simoutposvec.signals.values(:,3)>=0)
                powerOut(idx,simIDrun) = 1e6+sum(simOut(1,idx)...
                    .simoutposvec.signals.values(:,3)>=0) * 1e-2;
            end
        end
    end
elseif lsimIDrun > 1          % Full population

    % Run the simulation in parallel
    simOut = parsim(simIn(1:lsimIDrun),'UseFastRestart',true,'SetupFcn',...
        @() clearPersistentParSim(),'CleanupFcn',@() clearPersistentParSim());

    for idx = 1:lsimIDrun
        for ii = 1:nVw         % ii=1
            try                % Extract the time where the simulation finished
                timeSimFinish(ii,idx) = max(simOut(1,(idx-1)*nVw + ii).simoutPowerConstraint.time);
            catch
                timeSimFinish(ii,idx) = 0;
            end
            try
                powerOutN = simOut(1,(idx-1)*nVw + ii).simoutPower.signals.values(1:100);
                powerOutN(powerOutN == 0) = [];
                powerOutT = simOut(1,(idx-1)*nVw + ii).simoutPower.signals.values(101:200);
                powerOutT(powerOutT == 0) = [];
            catch
                powerOutN = [];
                powerOutT = [];
            end
            if length(powerOutN) > 1
                if powerOutT(1) - powerOutT(2) < deltaPowerT
                    powerOut(ii,simIDrun(idx)) = 0;
                elseif abs((powerOutN(1)-powerOutN(2))/powerOutN(1)) > deltaPower
                    powerOut(ii,simIDrun(idx)) = -powerOutN(1)*0.1;
                else
                    powerOut(ii,simIDrun(idx)) = -powerOutN(1);
                end
                if any(simOut(1,(idx-1)*nVw + ii).simoutposvec.signals.values(:,3)>=0)
                    powerOut(ii,simIDrun(idx)) =  1e6+sum(simOut(1,(idx-1)*nVw + ii)...
                        .simoutposvec.signals.values(:,3)>=0) * 1e-2;
                end
            end
        end
    end
end

clear(func2str(@checkSteadyState2))
clear(func2str(@switchSolver3))
clear(func2str(@deltaAERO))
clear(func2str(@checkSteadyState_FPerror))
clear(func2str(@plot_trajectory_dylan))

%% Buckling
maxLoadOut = zeros(numSims,nVw);
bucklingSF = 1.5;
bucklingPenaltyF1 = 100000;
bucklingPenaltyF2 = 100000;

timeCheckDelta = 60;     %Time from the end to check

for idx = 1:lsimIDrun
```

```
    for ii = 1:nVw      % ii=1
        if powerOut(ii,simIDrun(idx)) < 0
            timeCheckForce = timeSimFinish(ii,idx)-timeCheckDelta;
            try         % Extract the three force components
                F1 = simOut(1,(idx-1)*nVw+ii).simoutForce.signals.values...
                    (simOut(1,(idx-1)*nVw+ii).simoutForce.time > timeCheckForce,1);
                F2 = simOut(1,(idx-1)*nVw+ii).simoutForce.signals.values...
                    (simOut(1,(idx-1)*nVw+ii).simoutForce.time > timeCheckForce,2);
                F3 = simOut(1,(idx-1)*nVw+ii).simoutForce.signals.values...
                    (simOut(1,(idx-1)*nVw+ii).simoutForce.time > timeCheckForce,3);
                maxLoadOut(idx,ii) = max(sqrt(F1.^2+F2.^2+F3.^2));
            catch
                maxLoadOut(idx,ii) = 0;
            end
        else
            maxLoadOut(idx,ii) = 0;
        end
    end

    if max(maxLoadOut(idx,:)) > constraintOut(simIDrun(idx)).buckling/bucklingSF
        bucklingPenalty0 = bucklingPenaltyF1*(max(maxLoadOut(idx,:))/...
            (constraintOut(simIDrun(idx)).buckling/bucklingSF))^2;
        bucklingPenalty = bucklingPenaltyF2 + bucklingPenalty0;
    else
        bucklingPenalty = 0;
    end
    powerOut(nVw+2,simIDrun(idx)) = bucklingPenalty;
end

%% Flutter speed
maxflutterOut = zeros(numSims,3);
flutterSF = 1.0;
flutterPenaltyF1 = 100000;
flutterPenaltyF2 = 100000;

for idx = 1:lsimIDrun
    for ii = 1:nVw      % ii=1
        if powerOut(ii,simIDrun(idx)) < 0
            timeCheckForce = timeSimFinish(ii,idx)-timeCheckDelta;
            try
                flutter = simOut(1,(idx-1)*nVw+ii).simoutVel.signals.values...
                    (simOut(1,(idx-1)*nVw+ii).simoutVel.time > timeCheckForce,1);
                maxflutterOut(idx,ii) = max(flutter);
            catch
                maxflutterOut(idx,ii) = 0;
            end
        else
            maxflutterOut(idx,ii) = 0;
        end
    end

    if max(maxflutterOut(idx,:)) > constraintOut(simIDrun(idx)).flutter/flutterSF
        flutterPenalty0 = flutterPenaltyF1*(max(maxflutterOut(idx,:))/...
            (constraintOut(simIDrun(idx)).flutter/flutterSF))^2;
        flutterPenalty = flutterPenaltyF2 + flutterPenalty0;
    else
        flutterPenalty = 0;
    end
    powerOut(nVw+3,simIDrun(idx)) = flutterPenalty;
end

%% Apply penalties to output including flight path error
errorOut = zeros(nVw,1);
for idx = 1:lsimIDrun   % Find the error to the flight path
        for ii = 1:nVw      % ii=1
        try
            errorOutN = simOut(1,(idx-1)*nVw + ii).simoutFPError.signals.values(1,1:end);
            errorOutN(errorOutN == 0) = [];
        catch
            errorOutN = [];
        end
        if length(errorOutN) > 1
            errorOut(ii) = max(errorOutN)/1e5;
        else
            errorOut(ii) = 1e9/1e4;
        end
        end
    errorOut = max(errorOut);
    if errorOut>3e2
        flightpathPenalty = 10000;
    else
        flightpathPenalty = 0;
    end
    powerOut(nVw+1,simIDrun(idx)) = flightpathPenalty;
    % Apply penalties and the wind speed correction
        if powerOut(nVw,simIDrun(idx))<0
        powerOut(nVw+4,simIDrun(idx)) = powerOut(nVw,simIDrun(idx))/errorOut...
```

```
                + powerOut(nVw+1,simIDrun(idx)) + powerOut(nVw+2,simIDrun(idx)) +...
                powerOut(nVw+3,simIDrun(idx));
    else
            powerOut(nVw+4,simIDrun(idx)) = powerOut(nVw,simIDrun(idx))*errorOut...
                + powerOut(nVw+1,simIDrun(idx)) + powerOut(nVw+2,simIDrun(idx)) +...
                powerOut(nVw+3,simIDrun(idx));
            end
end
```

B.3. Wind speed adapted power optimisation

```
function powerOut = runsimParallel3D_V(simIn, constraintOut, numSims, simIDrun)
% Objective function to obtain a working input parameter set for lower wind
% speeds.

% simIn = Simulation input
% constraintOut = Structure containing the buckling load
% numSims = Number of simulations, equal to 1 or population size
% simIDrun = Simulation ID

%% run parallel simulation and extract power

%%%%%%%%%%%%%%%%%%%%%%%%%%%%%%%%%%%%%%%%%%%%%%%%%%%%%%%%%%%%%%%%%%%%%%%%%%%%%

deltaPower = 0.02;            % 2% -> steady state
deltaPowerT = 2;              % 2s min circle time

nVw = 1;                      %One wind speed per simulation, old implementation;

powerOut = 1e7.*ones(nVw+4,numSims);

timeSimFinish = zeros(nVw,numSims);

lsimIDrun = length(simIDrun);
if lsimIDrun == 1

    clear(func2str(@checkSteadyState2))
    clear(func2str(@switchSolver3))
    clear(func2str(@deltaAERO))
    clear(func2str(@checkSteadyState_FPerror))
    clear(func2str(@plot_trajectory_dylan))

    % Run the simulation
    simOut = sim(simIn(1),'UseFastRestart',true,'SetupFcn',...
        @() clearPersistentParSim(),'CleanupFcn',@() clearPersistentParSim());

    for idx = 1:nVw

        try                  % Extract the time where the simulation finished
            timeSimFinish(idx,1) = max(simOut(1,idx).simoutPowerConstraint.time);
        catch
            timeSimFinish(idx,1) = 0;
        end

        try
            powerOutN = simOut(1,idx).simoutPower.signals.values(1:100);
            powerOutN(powerOutN == 0) = [];
            powerOutT = simOut(1,idx).simoutPower.signals.values(101:200);
            powerOutT(powerOutT == 0) = [];
        catch
            powerOutN = [];
            powerOutT = [];
        end
        if length(powerOutN) > 1

            if powerOutT(1) - powerOutT(2) < deltaPowerT
                powerOut(idx,simIDrun) = 0;
            elseif abs((powerOutN(1)-powerOutN(2))/powerOutN(1)) > deltaPower
                powerOut(idx,simIDrun) = -powerOutN(1)*0.1;
            else
                powerOut(idx,simIDrun) = -powerOutN(1);
            end
            if any(simOut(1,idx).simoutposvec.signals.values(:,3)>=0)
                powerOut(idx,simIDrun) = sum(simOut(1,idx).simoutposvec.signals.values(:,3)>=0);
            end
        end
    end
elseif lsimIDrun > 1          % Full population

    % Run the simulation in parallel
    simOut = parsim(simIn(1:lsimIDrun),'UseFastRestart',true,'SetupFcn',...
        @() clearPersistentParSim(),'CleanupFcn',@() clearPersistentParSim());

    for idx = 1:lsimIDrun
        for ii = 1:nVw        % ii=1
```

```
            try             % Extract the time where the simulation finished
                timeSimFinish(ii,idx) = max(simOut(1,(idx-1)*nVw + ii).simoutPowerConstraint.time);
            catch
                timeSimFinish(ii,idx) = 0;
            end

            try
                powerOutN = simOut(1,(idx-1)*nVw + ii).simoutPower.signals.values(1:100);
                powerOutN(powerOutN == 0) = [];
                powerOutT = simOut(1,(idx-1)*nVw + ii).simoutPower.signals.values(101:200);
                powerOutT(powerOutT == 0) = [];
            catch
                powerOutN = [];
                powerOutT = [];
            end
            if length(powerOutN) > 1
                if powerOutT(1) - powerOutT(2) < deltaPowerT
                    powerOut(ii,simIDrun(idx)) = 0;
                elseif abs((powerOutN(1)-powerOutN(2))/powerOutN(1)) > deltaPower
                    powerOut(ii,simIDrun(idx)) = -powerOutN(1)*0.1;
                else
                    powerOut(ii,simIDrun(idx)) = -powerOutN(1);
                end
                % Check whether the plane crashed into the ground
                if any(simOut(1,(idx-1)*nVw + ii).simoutposvec.signals.values(:,3)>=0)
                    powerOut(ii,simIDrun(idx)) =  sum(simOut(1,(idx-1)*nVw + ii).simoutposvec.signals.values(:,3)>=0);
                end
            end
        end
    end
end

clear(func2str(@checkSteadyState2))
clear(func2str(@switchSolver3))
clear(func2str(@deltaAERO))
clear(func2str(@checkSteadyState_FPerror))
clear(func2str(@plot_trajectory_dylan))

%% Buckling
maxLoadOut = zeros(numSims,nVw);
bucklingSF = 1.5;
bucklingPenaltyF1 = 1000;
bucklingPenaltyF2 = 1000;

timeCheckDelta = 60;    %Time from the end to check

for idx = 1:lsimIDrun
    for ii = 1:nVw      % ii=1
        if powerOut(ii,simIDrun(idx)) < 0
            timeCheckForce = timeSimFinish(ii,idx)-timeCheckDelta;
            try         % Extract the three force components
                F1 = simOut(1,(idx-1)*nVw+ii).simoutForce.signals.values...
                    (simOut(1,(idx-1)*nVw+ii).simoutForce.time > timeCheckForce,1);
                F2 = simOut(1,(idx-1)*nVw+ii).simoutForce.signals.values...
                    (simOut(1,(idx-1)*nVw+ii).simoutForce.time > timeCheckForce,2);
                F3 = simOut(1,(idx-1)*nVw+ii).simoutForce.signals.values...
                    (simOut(1,(idx-1)*nVw+ii).simoutForce.time > timeCheckForce,3);
                maxLoadOut(idx,ii) = max(sqrt(F1.^2+F2.^2+F3.^2));
            catch
                maxLoadOut(idx,ii) = 0;
            end
        else
            maxLoadOut(idx,ii) = 0;
        end
    end

    if max(maxLoadOut(idx,:)) > constraintOut(simIDrun(idx)).buckling/bucklingSF
        bucklingPenalty0 = bucklingPenaltyF1*(max(maxLoadOut(idx,:))/...
            (constraintOut(simIDrun(idx)).buckling/bucklingSF))^2;
        bucklingPenalty = bucklingPenaltyF2 + bucklingPenalty0;
    else
        bucklingPenalty = 0;
    end
    powerOut(nVw+2,simIDrun(idx)) = bucklingPenalty;
end

%% Flutter speed
maxflutterOut = zeros(numSims,3);
flutterSF = 1.0;
flutterPenaltyF1 = 1000;
flutterPenaltyF2 = 1000;

for idx = 1:lsimIDrun
    for ii = 1:nVw      % ii=1
        if powerOut(ii,simIDrun(idx)) < 0
            timeCheckForce = timeSimFinish(ii,idx)-timeCheckDelta;
```

```matlab
            try
                flutter = simOut(1,(idx-1)*nVw+ii).simoutVel.signals.values...
                    (simOut(1,(idx-1)*nVw+ii).simoutVel.time > timeCheckForce,1);
                maxflutterOut(idx,ii) = max(flutter);
            catch
                maxflutterOut(idx,ii) = 0;
            end
        else
            maxflutterOut(idx,ii) = 0;
        end
    end

    if max(maxflutterOut(idx,:)) > constraintOut(simIDrun(idx)).flutter/flutterSF
        flutterPenalty0 = flutterPenaltyF1*(max(maxflutterOut(idx,:))/...
            (constraintOut(simIDrun(idx)).flutter/flutterSF))^2;
        flutterPenalty = flutterPenaltyF2 + flutterPenalty0;
    else
        flutterPenalty = 0;
    end
    powerOut(nVw+3,simIDrun(idx)) = flutterPenalty;
end

%% Apply penalties to output including flight path error and wind speed correction
errorOut = zeros(nVw,1);
for idx = 1:lsimIDrun   % Find the error to the flight path
        for ii = 1:nVw      % ii=1
        try
            errorOutN = simOut(1,(idx-1)*nVw + ii).simoutFPError.signals.values(1:end,1);
            distanceN = simOut(1,(idx-1)*nVw + ii).simoutFPError.signals.values(1:end,2);
            ind = find(errorOutN ~= 0);
            errorOutN(errorOutN == 0) = [];
            try
                if lsimIDrun>1
                    powerOutN = simOut(1,(idx-1)*nVw + ii).simoutPower.signals.values(1:100);
                    powerOutN(powerOutN == 0) = [];
                end
            catch
                powerOutN = [0 0];
            end
            for k=1:numel(ind)
                if k == 1
                    if mean(distanceN(find(distanceN>0,1):ind(k)))<0.05*simIn(idx)...
                            .Variables(1).Value.inputLimit.spiralRadius
                        errorOutN(k) = 0;
                    else
                        errorOutN(k) = mean(distanceN(find(distanceN>0,1):ind(k)));
                    end
                else
                    if mean(distanceN(ind(k-1)+1:ind(k)))<0.05*simIn(idx).Variables(1)...
                            .Value.inputLimit.spiralRadius
                        errorOutN(k) = 0;
                    else
                        errorOutN(k) = mean(distanceN(ind(k-1)+1:ind(k)));
                    end
                end
            end
        catch
            errorOutN = [];
            powerOutN = [0 0];
        end
        if length(powerOutN)>1
            if length(errorOutN) > 1 && abs((powerOutN(1)-powerOutN(2))/powerOutN(1)) < deltaPower
                errorOut(ii) = errorOutN(1)/simIn(idx).Variables(1).Value.inputLimit...
                    .spiralRadius*3e2;
            elseif length(errorOutN) > 1
                errorOut(ii) = max(errorOutN)/simIn(idx).Variables(1).Value.inputLimit...
                    .spiralRadius*3e2;
            else
                errorOut(ii) = 1e3;
            end
        else
            if length(errorOutN) > 1
                errorOut(ii) = max(errorOutN)/simIn(idx).Variables(1).Value.inputLimit...
                    .spiralRadius*3e2;
            else
                errorOut(ii) = 1e3;
            end
        end
        end

    if errorOut(ii)>0
        flightpathPenalty = 10+errorOut(ii);
    else
        flightpathPenalty = 0;
    end
    powerOut(nVw+1,simIDrun(idx)) = flightpathPenalty;

```

```
    % Force the power to be more optimal when the wind speed is lower
    windi = exp(simIn(idx).Variables(1).Value.windProp.Velocity)^0.9; % Power prod.
    windi2 = exp(simIn(idx).Variables(1).Value.windProp.Velocity^0.0001)/2e3; % Power loss

    % Apply penalties and the wind speed correction
        if powerOut(nVw,simIDrun(idx))<0
        powerOut(nVw+4,simIDrun(idx)) = powerOut(nVw,simIDrun(idx))/windi + ...
            powerOut(nVw+1,simIDrun(idx)) + powerOut(nVw+2,simIDrun(idx)) + ...
            powerOut(nVw+3,simIDrun(idx));
    else
        powerOut(nVw+4,simIDrun(idx)) = powerOut(nVw,simIDrun(idx))*windi2 + ...
            powerOut(nVw+1,simIDrun(idx)) + powerOut(nVw+2,simIDrun(idx)) + ...
            powerOut(nVw+3,simIDrun(idx));
        end
end
```